Manukau Harbour Numerical Modelling

Sediment Transport Report

Report prepared for Tonkin & Taylor

June 2024

MetOcean
SOLUTIONS

Document History

Versions

Version	Revision Date	Summary	Reviewed by
0.1	05/02/2024	Draft document for Client review	Cussioli/Watson/Berthot
0.2	09/02/2024	Draft document for Client review	Cussioli/Watson/Berthot
0.3	19/02/2024	Draft document for Client review	Cussioli/Watson/Berthot
1.1	14/05/2024	Draft addressing external review comments	Cussioli
2.0	05/06/2024	Final Version	Cussioli

Distribution

Version	Date	Distribution
1.0	19/02/2024	Tonkin & Taylor
2.0	05/06/2024	Tonkin & Taylor

Document ID: P597-02

Authors

Cussioli M., Watson H. Berthot A.

Contributors

Thiebaut S., Gardiner S.

MetOcean Solutions is a Division of Meteorological Services of New Zealand Ltd, MetraWeather (Australia) Pty Ltd [ACN 126 850 904], MetraWeather (UK) Ltd [No. 04833498] and MetraWeather (Thailand) Ltd [No. 0105558115059] are wholly owned subsidiaries of Meteorological Service of New Zealand Ltd (MetService).

The information contained in this report, including all intellectual property rights in it, is confidential and belongs to Meteorological Service of New Zealand Ltd. It may be used by the persons to which it is provided for the stated purpose for which it is provided and must not be disclosed to any third person without the prior written approval of Meteorological Service of New Zealand Ltd. Meteorological Service of New Zealand Ltd reserves all legal rights and remedies in relation to any infringement of its rights in respect of this report.

Executive Summary

Earlier studies identified that the current Ports of Auckland Ltd (POAL) freight operation in the Waitematā Harbour is likely to run out of capacity to cater for Auckland's long-term freight needs. The Manukau Harbour has previously been identified as a potential port location, however there are unanswered questions around the technical feasibility of this given the complex and dynamic nature of the harbour entrance along with other factors associated with greenfield port development.

Te Manatū Waka / the New Zealand Ministry of Transport has appointed Tonkin & Taylor Ltd and their subconsultants (Royal HaskoningDHV, MetOcean Solutions (MOS), Pacific Marine Management, the University of Auckland, Discovery Marine Limited, and RMA Science) to undertake a feasibility study to understand whether it would be technically possible to locate a port in the Manukau Harbour from a navigation and operational reliability perspective. Environmental, social, and economic factors are not part of the current scope of work.

MetOcean Solutions has undertaken a numerical modelling study to support this feasibility study. The modelling work is presented in two reports:

- TWP03b (MOS) - Numerical modelling - Metocean study report - MOS Report P0597-01
- TWP03c (MOS) - Numerical modelling - Sediment Transport report – MOS Report P0597-02

This report is presenting the Sediment Transport study (i.e. second report).

To better understand sediment transport processes near the entrance bar of Manukau Harbou, we simulated a total of 17 control scenarios with metocean conditions representative of the site. Each modelled scenario involved a 24-hour wave-hydrodynamic warm-up period without sediment movement, followed by sediment transport simulations over a complete 12-hour tidal cycle. Some of these scenarios were also used for sensitivity testing and rerun with different tidal, sediment or wind conditions.

The hydrodynamic and sediment transport modelling was run coupled with waves in depth-averaged (2D) mode. Modelling was undertaken using the same grids, datum and bathymetries used in the hydrodynamic modelling (Figure 1), described in the metocean study report (TWP03b (MOS) - Numerical modelling - Metocean study report).

The simulations were run for two bathymetry configurations: the 'existing' bathymetry (developed from the 2023 survey), and the channel 'design' bathymetry (the existing 2023 bathymetry with the addition of the South West dredged channel) (Figure 1). The bathymetries considered the bedforms and morphology of Manukau's ebb-tidal delta (see Figure 2).

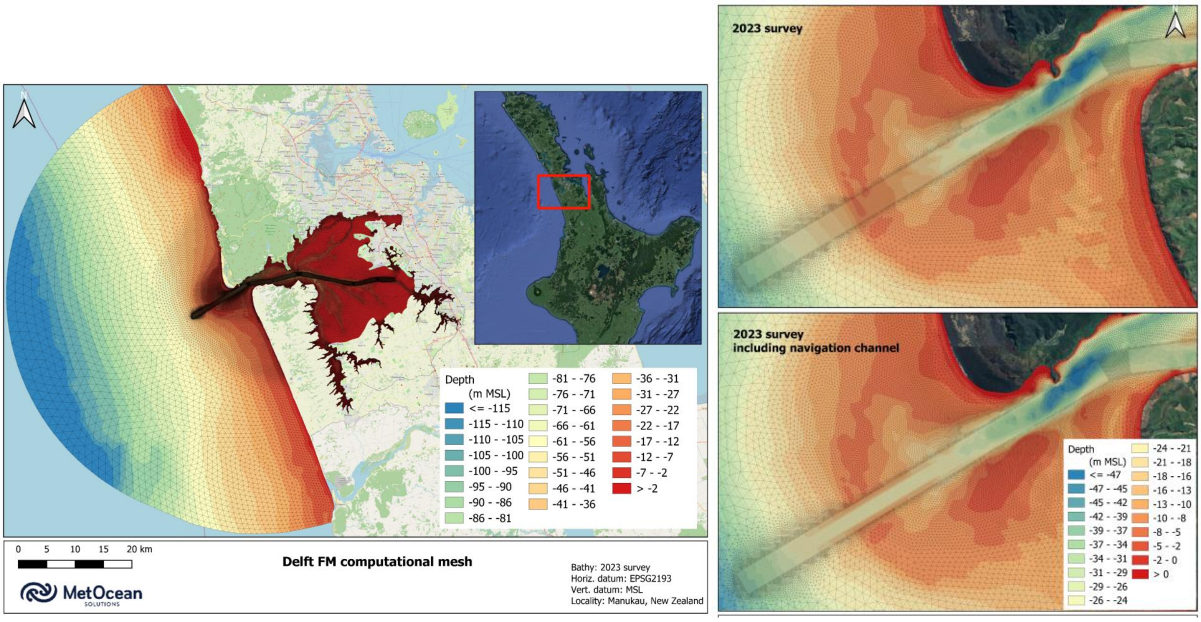

Figure 1: Delft FM computational mesh of Manukau Harbour (left). The model bathymetry near the Manukau entrance bar for the 'existing' simulation is shown on top right panel and for the channel 'design' simulations on the bottom right panel.

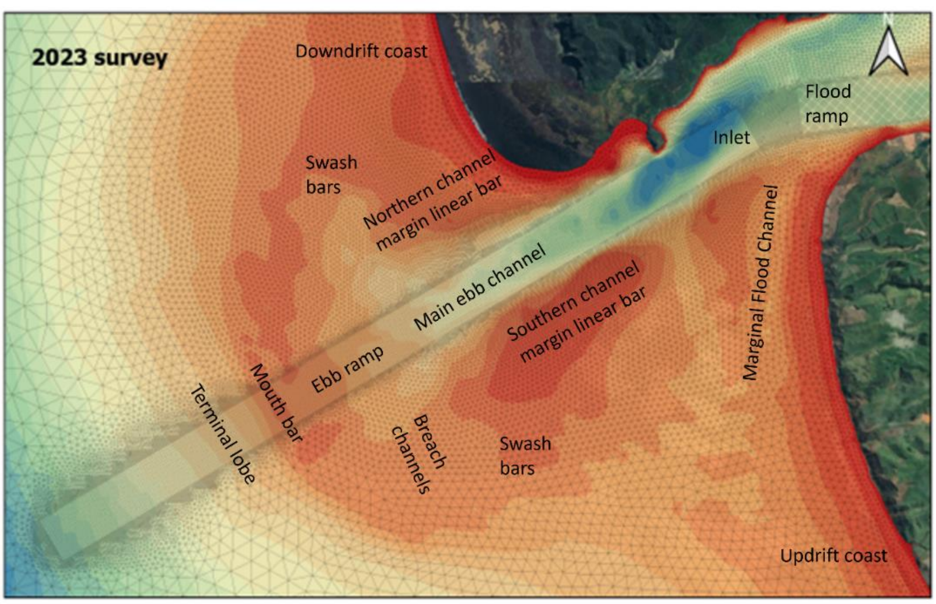

Figure 2: Main bedforms and general morphology of Manukau ebb-tidal delta.

Particle size and sediment density analysis were available from in situ surface samples collected as part of this project and presented in the TWP02 (TT) – Fieldwork. The present study considered an initial uniform sediment layer of 5 m adopting a single sand fraction of 250 µm. We ran a few scenarios using 3 sediment fractions (150 µm, 250 µm, and 500 µm) combined in a spatially varying distribution. Additionally, we ran separate single-fraction simulations using fine (150 µm) and coarse (500 µm) fractions in sensitivity test runs.

The model was validated by comparing model results with (a) sediment concentration estimated from suspended sediment collected in a catcher deployed near the main channel, (b) empirical calculations of sediment transport rates across an open coast transect, and (c) published data of suspended sediment concentration for a site in the inner harbour. The comparisons show the model is reproducing reasonably well the magnitude of sediment transport and concentrations.

Examples of results of sediment erosion/deposition and transport direction at different stages fo the tide, for the 'existing' and channel 'design' with wave boundary conditions characterized by H_s = 5 m, T_p = 15 s and Dir = 230 deg are presented on Figure 3 and Figure 4.

During flood tide, transport is towards the shore, and high erosion and deposition rates occur around the mouth bar and banks. During the ebb tide, stronger currents in the main ebb channel encounters the incoming waves at the mouth bar, leading to high erosion and deposition rates. In the 'channel' case, transport within the channel is oriented offshore, driving sediment deposition offshore of this region.

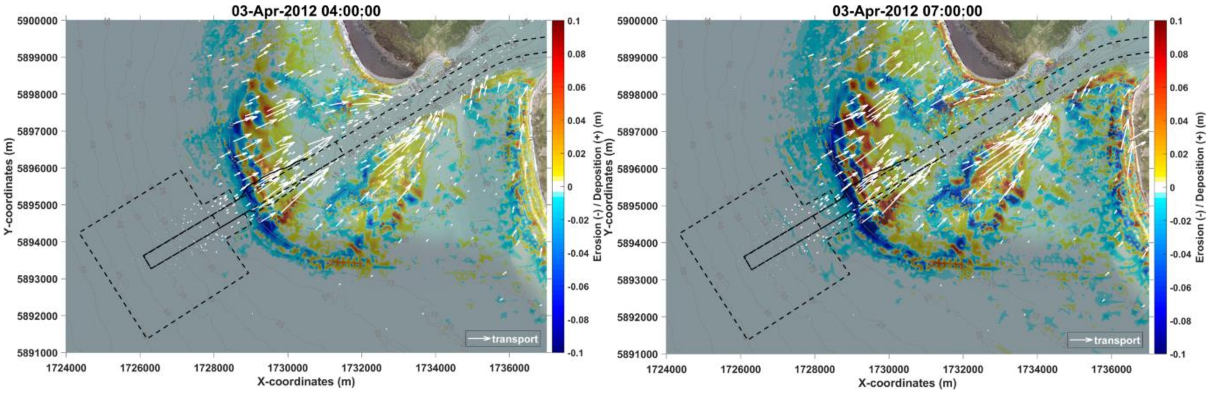

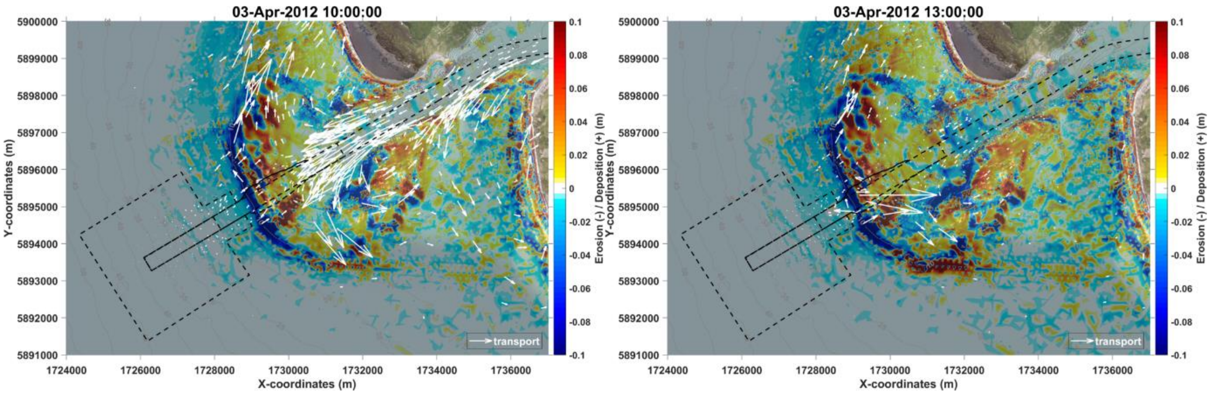

*Figure 3: Map results of erosion/deposition for run using the **existing bathymetry**, Control 3 (H_s = 5 m, T_p = 15 s and Dir = 230 deg). Results for flood tide (top left), high tide (top right), ebb tide (bottom left) and low tide (bottom right). Negative values (blue) represent erosion and positive values (red) represent deposition of sediment. White arrows show sediment transport direction.*

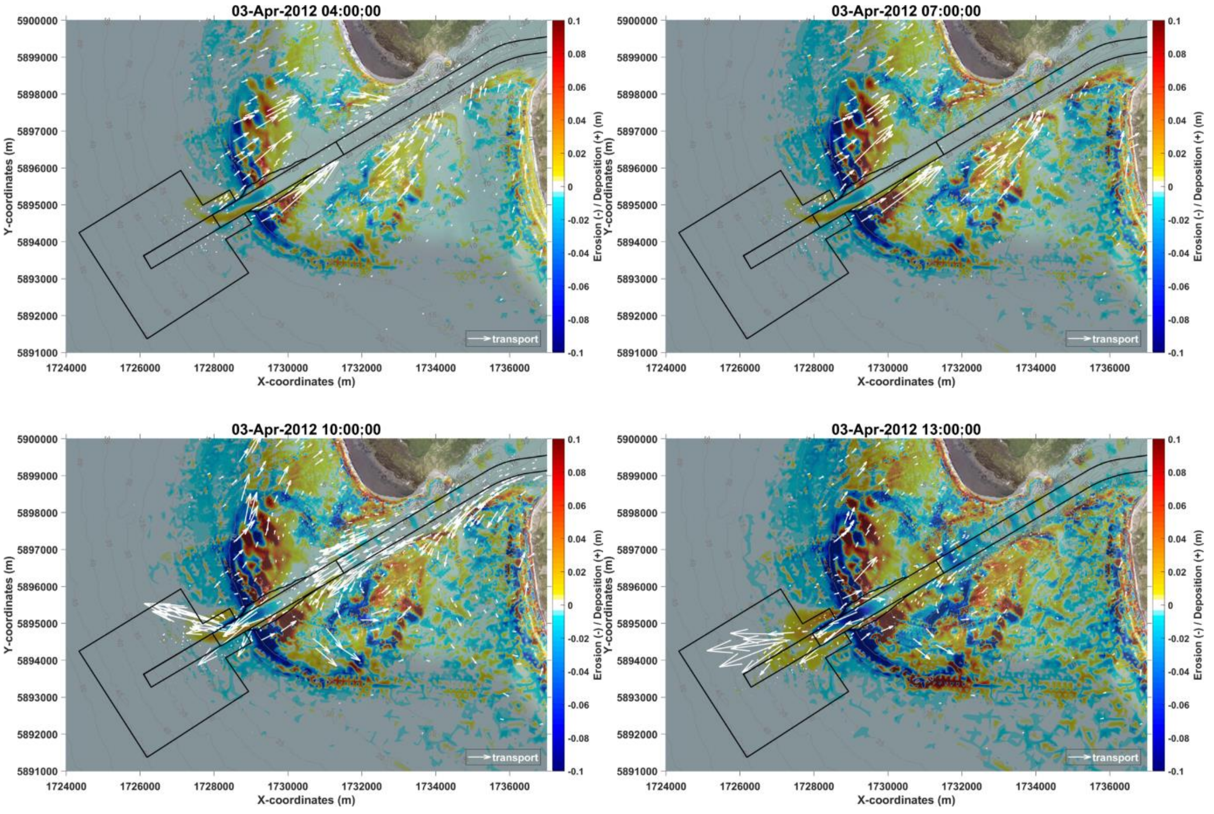

*Figure 4: Map results of erosion/deposition for run **including the conceptual navigation channel**, Control 7 (H_s = 5 m, T_p = 15 s and Dir = 230 deg). Results for flood tide (top left), high tide (top right), ebb tide (bottom left) and low tide (bottom right). Negative values (blue) represent erosion and positive values (red) represent deposition of sediment. White arrows show sediment transport direction.*

Based on the results of control scenarios, we proposed a conceptual model for sediment pathways representative of the sediment dynamics on the entrance bar. Below is an example of the conceptual models comparing 'existing' and 'channel' scenarios. With Southwestern waves and the 'existing' bathymetry, there is a higher potential for onshore transport at the terminal lobe, influenced by wave processes on the bar. Within the channel, tidal currents lead to offshore sediment transport . For the 'channel scenario', transport of sediments is offshore to deeper areas (Figure 5).

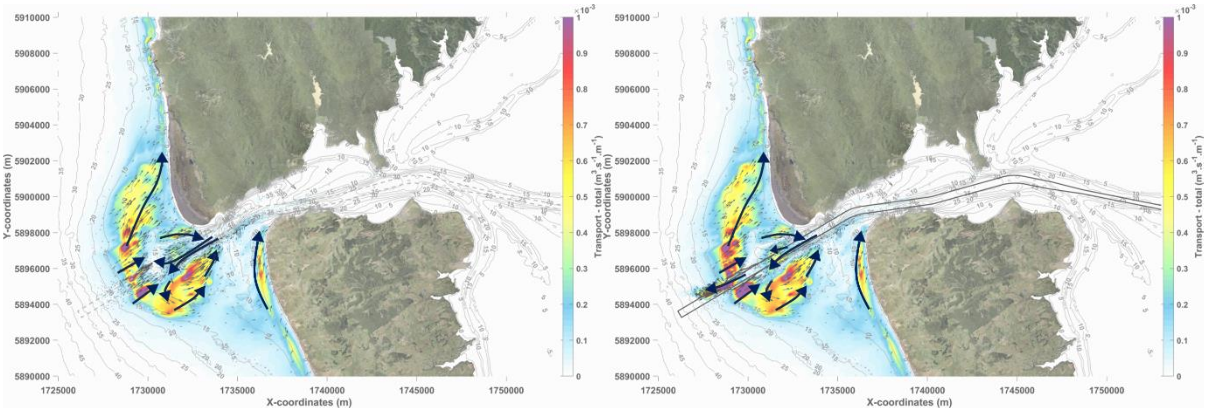

Figure 5: Sediment transport magnitude (colormap) and direction (thin black arrows) for runs including waves (H_s = 5 m, T_p = 15 s and Dir = 230 deg). Control 3, existing bathymetry (top) and Control 7, bathymetry including the concept navigation channel (bottom). Bold blue arrows represent the main transport pattern.

Infill volumes after the 12-hour runs were calculated within selected areas of interest (polygons in Figure 6). Within the 'bar' polygons (3+4+5+6), infill volumes over 12 hours varied from approximately 1,200 m^3 to around 60,400 m^3. Deposition volumes in the inner harbour polygon were comparatively very low (maximum deposition of approximately 400 m^3 over 12 hours.

Other scenarios were compared in the report:

- Wind vs no wind scenarios
- SW vs NW wave scenarios
- 1989 bathymetry scenarios
- Runs with 3 sediment fractions combined
- Individual runs using 150 µm and 500 µm sediment fractions
- Bar and open coast transects

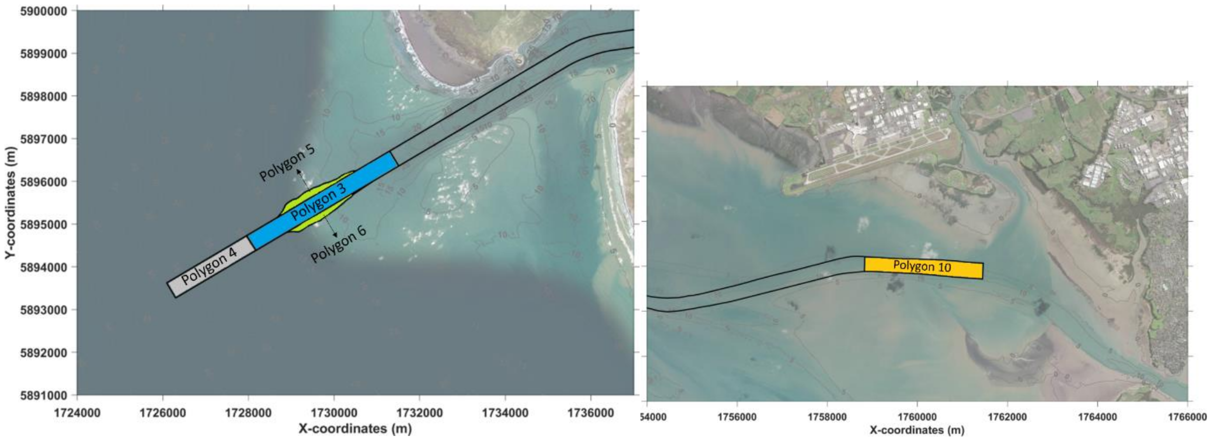

Figure 6: Polygons used to calculate infill rates in the main channel and inner harbour.

Annual Infill

To quantify sediment infill for a range of wave conditions present at the site, selection of wave conditions representative the wave climate in the area were used to define Input Reduction (IR) scenarios. These scenarios were run for 12-hours, similarly to the control runs, and infill rates were calculated.

A transformation process, based on the offshore wave climate and the Input Reduction scenarios matrix of results, was used to determine the annual sediment infill estimate. The transformation was undertaken through a 4D scattered interpolation. Wave parameter timeseries from the offshore 41-year SWAN wave hindcast is resampled to give the 12-hour average wave conditions. The 12-hour wave parameter timeseries is interpolated against the run matrix and assigned a 12-hour infill volume. For the final annual infill estimate we have repeated this methodology by shifting the start of the 12-hour averaging window by one-hour increments to account for the occurrence of potential joint occurrence of tide and wave events.

The transformed values provide annual infill rates between 5.03M to 7.68M m^3/year (average of 6.54M m^3/year) at the bar. Net change (deposition – erosion) suggests that while there is a high volume of sediment moving at the bar there is also a large amount of net loss/erosion.

Applying a 5% increase in wave height to account for climate change, there is a potential increase in mean annual infill of about 500,000 m^3/year on average (about 8% increase in infill). The maximum annual infill calculated is 8.37M m3 for the year 2016.

Synthetic storm

We ran a 10-day continuous simulation of a synthetic storm to determine if the IR method (several events of 12 hours each) provided an adequate representation of the infill that could occur during a continuous event. Comparing results of the 12-h IR with the storm event, cumulative volumes derived from the IR results indicated approximately 20% more infill compared to the continuous synthetic storm run at the end of the simulation. This indicates that the transformation methodology is conservative.

Navigation Channel Infill Sensitivity

This sensitivity analysis indicates that whilst our transformation process methodology to define the annual infill may be conservative by approximately 20%, the consideration for a single medium sand fraction (250 μm) may be underpredicting the infill estimate by about 20%. Indeed, simulations with 150 μm show a larger total infill while simulation with 500 μm show a lower total infill. These assumptions and model limitations are each affecting the results in opposing manner, so results are likely accurate within +/- 20%, which is a reasonable outcome for the overall annual estimate of approximately 6.5 M m^3/year (or 5.03M to 7.68M m^3/year variability).

Inner Harbour Port Area Annual Infill

Sediment infill in the inner harbour was estimated based on simulations with (a) tide only no wind, (b) tide with medium strength wind (10m/s), and (c) tide with strong wind (20m/s). The simulations considered a fine sands fraction of 150 μm. Based on analysis of the wind speed probability of occurrence, infill estimates were combined with wind probabilities to determine the overall annual infill estimate, expected to be approximately 100,000 to 150,000 m^3/year (within polygon 10) and about 60,000 m^3/year per km along the 5 km of channel batter extending out from the proposed port area.

South Channel Assessment

In addition to the assessment for the prefered navigation channel within the natural South West Channel, a high level assessment of a concept navigation channel in the South Channel was also undertaken. We ran a typical scenario similar to the control runs (H_s = 5 m, T_p = 15 s and Dir = 230 deg) using the ‘design’ bathymetry with the deepened South Channel (same depth and width as the South West channel).

Results from this run show the main erosion and deposition occur along the batter slopes. Infill volume is approximately 1.6 times greater than the sediment calculated within the bar polygons for the South West channel under the same forcing conditions. Assuming a 1.6 factor between the South West channel and the South Channel option, the annual infill would then be about 10.4M m^3/year on average and up to 12.3M m^3/year for the South Channel. This assessment presents a preliminary overview to draw comparisons to the South West channel infill rates.

Modelling results were provided as maps and tabulated values to the other project work stream teams. The data has been used for the analysis presented in the coastal processes assessment (TW03 (TT) – Coastal Processes), the navigation and channel design assessment (TW04 (RH) – Navigation and Channel Design, and TW05 (PMM) – Navigational Operability).

Contents

List of Figures

List of Tables

1 Introduction

Earlier studies identified that the current Ports of Auckland Ltd (POAL) freight operation in the Waitematā Harbour is likely to run out of capacity to cater for Auckland's long-term freight needs.

The Manukau Harbour has previously been identified as a potential port location, however, there are unanswered questions around the technical feasibility of this given the complex and dynamic nature of the harbour entrance along with other factors associated with greenfield port development.

Te Manatū Waka / the New Zealand Ministry of Transport has appointed Tonkin & Taylor Ltd and their subconsultants (Royal HaskoningDHV, MetOcean Solutions, Pacific Marine Management, the University of Auckland, Discovery Marine Limited, and RMA Science) to undertake a feasibility study to understand whether it would be technically possible to locate a port in the Manukau Harbour from a navigation and operational reliability perspective. Environmental, social, and economic factors are not part of the current scope of work.

This study will support on-going work by the Ministry on the National Freight and Supply Chain Strategy, which is examining New Zealand's freight system for the next 30 years. MetOcean Solutions scope includes developing calibrated wave (spectral), hydrodynamic and sediment transport models of the harbour and entrance to inform navigation and maintenance dredging requirements.

The modelling work is presented in two reports:

- Manukau Harbour Numerical Modelling - Metocean Study Report P0597-01
- Manukau Harbour Numerical Modelling – Sediment Transport Report P0597-02

This report is the second of the two reports and presents the input data, numerical model setup, model verification and simulations, the sediment transport processes and predicted infill to the concept navigation channel. The main body of the report focuses on the bar area. Additional analysis of the inner harbour area is presented in Appendix B.

This report covers a description of the available data and datums used in Section 2. Section 3 presents a description of the Delft FM hydrodynamic wave and sediment transport model numerical setup and verification. Model simulations results and a description of the entrance bar sediment transport patterns is presented in Section 4.

The sedimentation and infill assessment in shown in Section 5 and references are given in Section 6.

2 Input Data Overview

The metocean datasets used for setup and validation of the wave and hydrodynamic models are presented in Metocean Study report (first report for this project - P597-01). This section presents the Datum and a summary of the sediment data used for this part of the study, i.e. the sediment transport modelling.

2.1 Datum

The project datum and coordinate system adopted for this study are as follows:

- Vertical Datum: Chart Datum (CD) Onehunga
- Coordinate: NZTM2000 (EPSG: 2193)

Mean Sea Level (MSL) at Onehunga is 2.43 m above CD (based on the LINZ tide tables) but some data is referenced to the Paratutae datum which is 2.33 m above CD. The NZVD2016 is 2.5 m above Onehunga.

For the vertical datums used in the numerical models in this study, all model bathymetry and water levels are relative to MSL (CD + 2.43 m).

Both cartesian and spherical projections were used for the site. Delft FM modelling used cartesian coordinates using the NZGD2000 / New Zealand Transverse Mercator 2000 with EPSG 2193.

2.2 Sediments

Particle size analysis was provided by Tonkin & Taylor in TWP02 – Fieldwork Report for surface samples at50 sites (Table 2-1 and Figure 2-1). The results showed that the main ebb channel sites are primarily characterized by medium sand, with some samples (e.g., 1.08 – see Figure 2-2 (top), 1.10, and 1.14) exhibiting coarser particles. In contrast, samples collected along the south channel predominantly consist of fine sand (Figure 2-3).

Towards the inner harbour, samples showed finer particles (Figure 2-2 – bottom, and Figure 2-4), although some locations showed increased grain sizes attributed to shell fragments.

Analysis of particle density for selected samples (Table 2-2) shows an average density of 3.04 g/cm^3 (3,040 kg/m^3) for samples collected from the southwest and south channels, as well as around the bars. Samples from the inlet and inner harbour presented slightly lower densities. The overall average particle density is 2.88 g/cm^3 (2,880 kg/m^3). Note that density analysis were performed without removing calcium carbonate.

Table 2-1: Particle sizes for samples collected in the Manukau Harbour and Bar.

Sample Name	D10	D50	D90	Classification
1.01 SC1	101	169	295	fine sand
1.02 SC2	105	172	280	fine sand
1.03 SC3	138	216	333	fine sand
1.04 SC4	130	204	319	fine sand
1.05 SC5	166	267	423	medium sand
1.06 SC6	167	289	537	medium sand
1.07 SC7	215	334	523	medium sand
1.08 SC8	314	521	840	coarse sand
1.09 SC9	209	329	516	medium sand
1.10 SC10	385	641	1060	coarse sand
1.11 SC11	218	404	749	medium sand
1.12 SC11	275	429	675	medium sand
1.13 SC12	162	263	421	medium sand
1.14 SC13	319	517	823	coarse sand
1.15 M.Heads outer Bar #1	125	209	363	fine sand
1.16 Manukau outer Bar #1	202	355	618	medium sand
1.17 M.Heads Inner Bar #3	167	283	484	medium sand
1.18 M.Heads Inner Bar #4	285	453	717	medium sand
AVERAGE	**205**	**336**	**554**	**medium sand**
2.01 S2	163	272	450	medium sand
2.02 2-300E	209	360	614	medium sand
2.03 2-300W	199	325	528	medium sand
2.04 2-600S	193	451	1090	medium sand
2.05 2-600W	168	271	439	medium sand
2.06 S2-300S	244	446	795	medium sand
2.07 SS14	249	405	646	medium sand
2.08 SS15	161	306	747	medium sand
2.09 SS16	315	565	1030	coarse sand
AVERAGE	**211**	**378**	**704**	**medium sand**
3.01 SS17	138	207	309	fine sand
3.02 SS18	142	218	334	fine sand
3.03 SS19	132	201	302	fine sand
3.04 SS20	128	193	291	fine sand
3.05 SS21	134	208	322	fine sand
3.06 SS22	137	214	327	fine sand
3.07 SS23	138	216	333	fine sand
3.08 SS24	89.9	370	2020	medium sand
3.09 SS25	145	288	1480	medium sand
AVERAGE	**132**	**235**	**635**	**fine sand**
4.01 1A	6.45	143	423	fine sand

4.02 1B	2.3	15.9	154	silt
4.03 1C	6.4	162	610	fine sand
4.04 1D	4.65	103	312	very fine sand
4.06 1F	102	182	350	fine sand
4.07 1G	95.9	260	1190	medium sand
4.08 1H	6.7	147	286	fine sand
AVERAGE	**32**	**145**	**475**	**fine sand**
5.01 2A	3.46	46.7	210	silt
5.02 2B	3.02	32.9	210	silt
5.03 2C	107	656	1890	coarse sand
5.04 2D	3.59	58	287	silt
5.05 2E	7.3	186	763	fine sand
5.06 2F	8.17	146	262	fine sand
5.07 2G	4.27	62.3	268	silt
AVERAGE	**20**	**170**	**556**	**fine sand**
OVERALL AVERAGE	**143**	**275**	**585**	**medium sand**

Table 2-2: Particle density for selected samples collected at Manukau.

Sample Name	Particle Density g/cm^3
1.01 SC1	3.55
1.09 SC9	3.02
1.14 SC13	2.77
1.18 M. Heads Inner Bar #4	2.82
2.03 S-300W	2.94
3.03 SS19	2.94
4.01 1A	2.71
4.04 1D	2.72
5.02 2B	2.64
5.03 2C	2.69

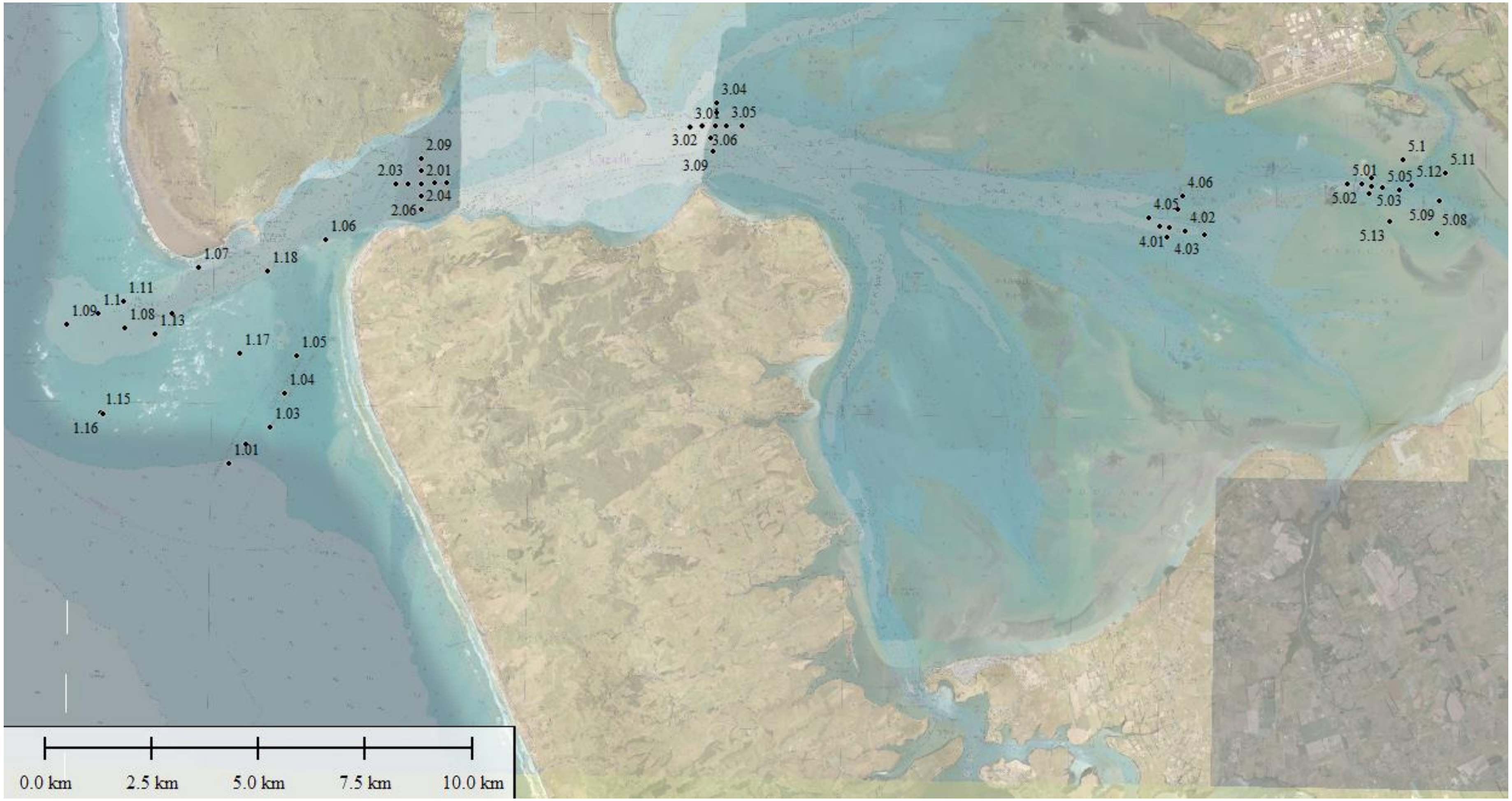

Figure 2-1: Sediment sampling locations.

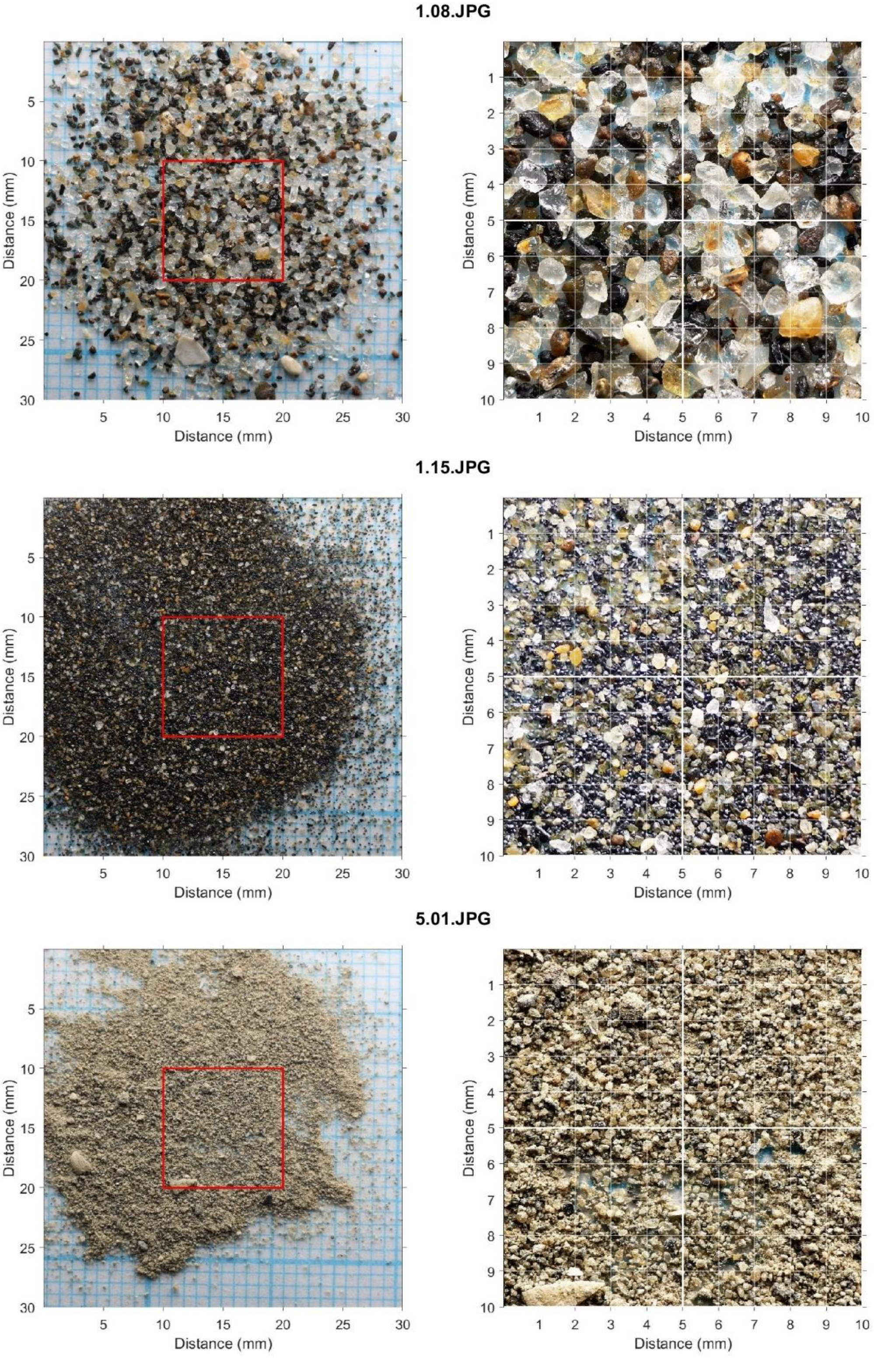

Figure 2-2: Sediment samples showing grain characteristics.

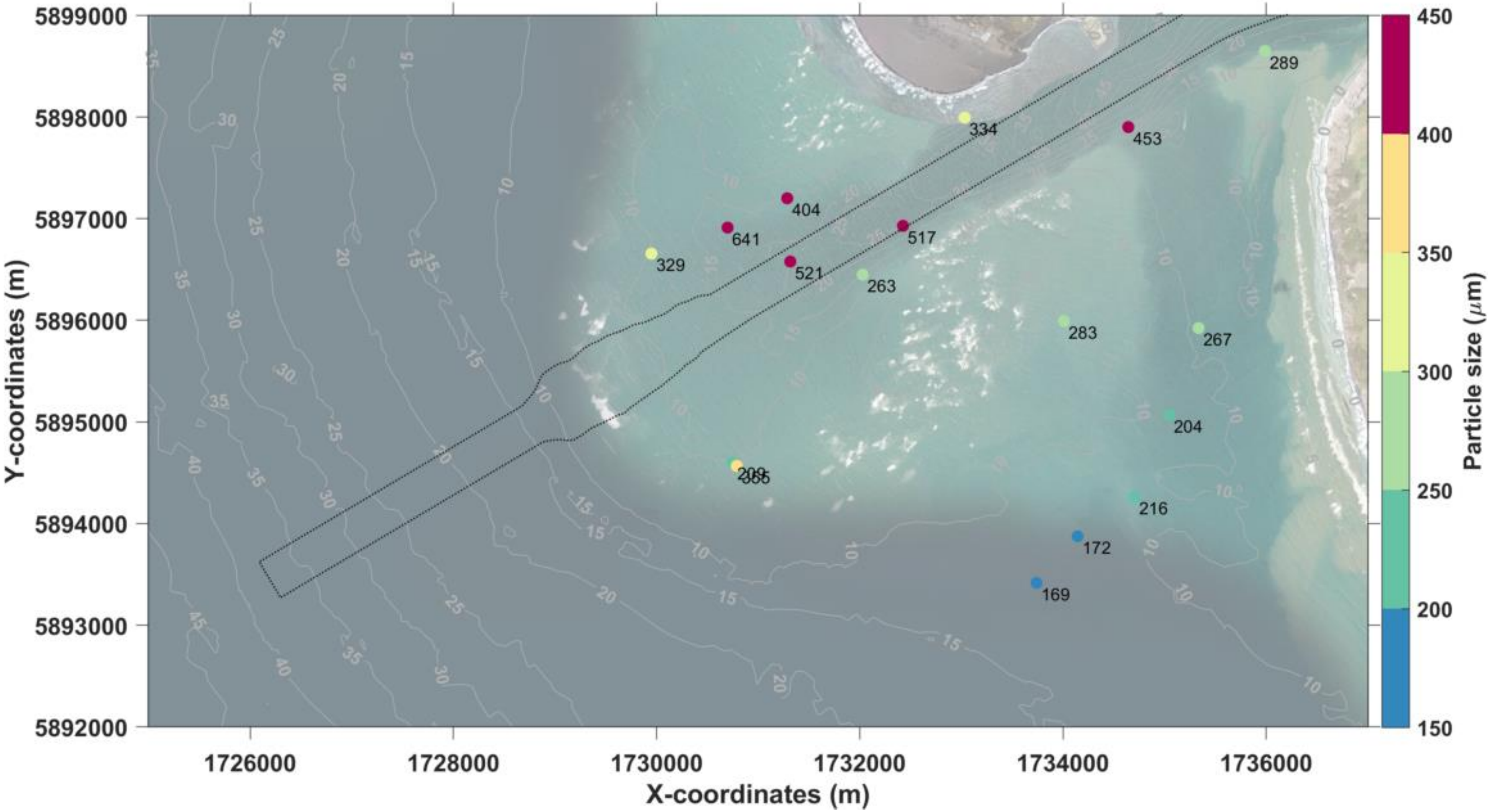

Figure 2-3: Particle size (D50) for samples within the southwest and south channels and around the bars.

Figure 2-4: Particle size (D50) for samples in the inner harbour.

3 Numerical Model Description and Setup

3.1 Delft FM Hydrodynamic Wave and Sediment Transport Model

The hydrodynamic and sediment transport modelling followed an approach that aimed at capturing the complete range of possible hydrodynamic forcing expected near the site to provide a robust picture of the likely transport and deposition patterns. For this reason, the model was run coupled with waves.

The hydrodynamic model was configured in depth-averaged (2D) mode. Modelling was undertaken in cartesian coordinates using the NZGD2000 / New Zealand Transverse Mercator 2000 with EPSG 2193. The model was run in UTC. The bathymetry of the model (Figure 3-1 and Figure 3-2) is set to MSL relative to Onehunga datum (which is CD + 2.43 m).

Each modelled scenario, discussed in detail in the next section, involved a 24-hour wave-hydrodynamic warm-up period without sediment movement, followed by sediment transport simulations over a complete 12-hour tidal cycle. There was no update in the bathymetry throughout the simulations, with variations limited to sediment thickness.

Wave boundary conditions were applied at the offshore boundaries, denoted by the dark blue grid (200-m grid) in Figure 3-3, which was nested to different grids with varying resolutions. The coupled SWAN wave model is comprised of four nested grids covering the entire Delft-FM domain (Figure 3-3). The 200 m extent is the same as that used in the SWAN hindcast and the outer 80m, 25m grids and inner 80 m were rotated to be aligned with the coastline.

Multiple scenarios were simulated, each characterized by specific initial bathymetry and wave conditions. The wave conditions were maintained constant at the boundaries throughout each simulation run.

This comprehensive methodology allowed us to explore various scenarios and analyse the impact of different initial conditions on wave, hydrodynamic, and sediment transport interactions.

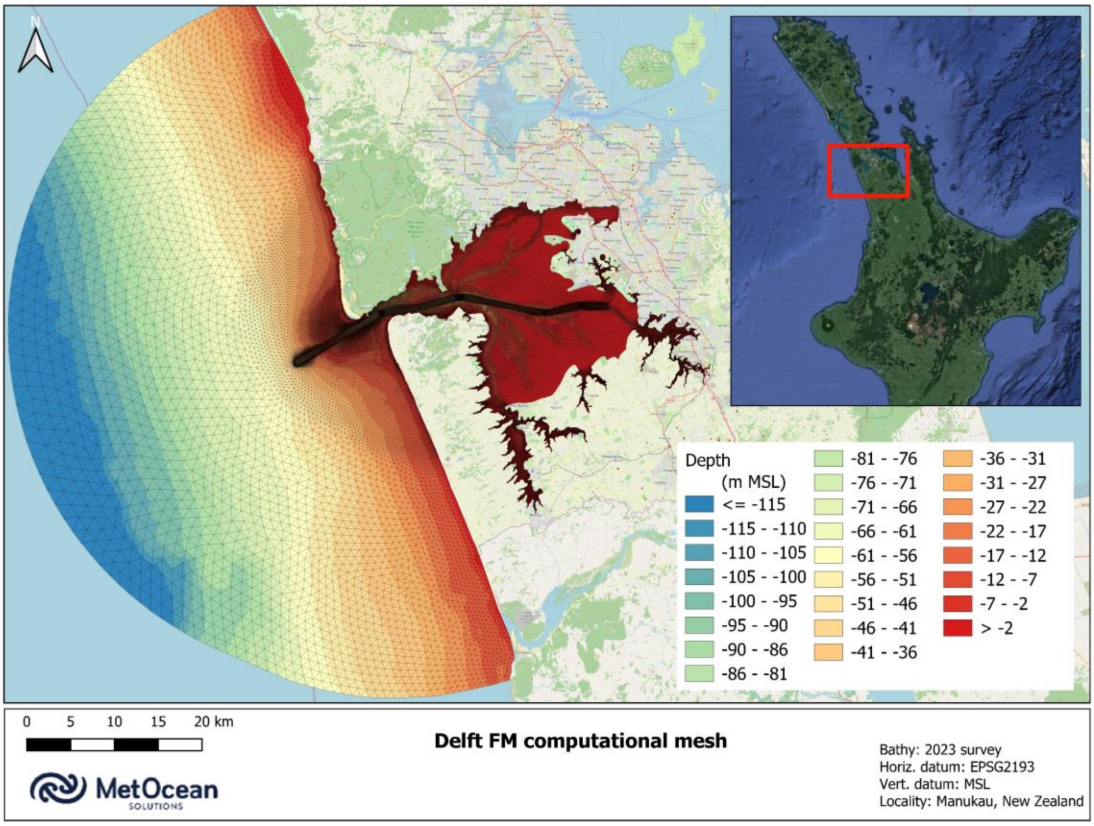

Figure 3-1 Delft FM computational mesh of Manukau Harbour with the 2023 existing bathymetry.

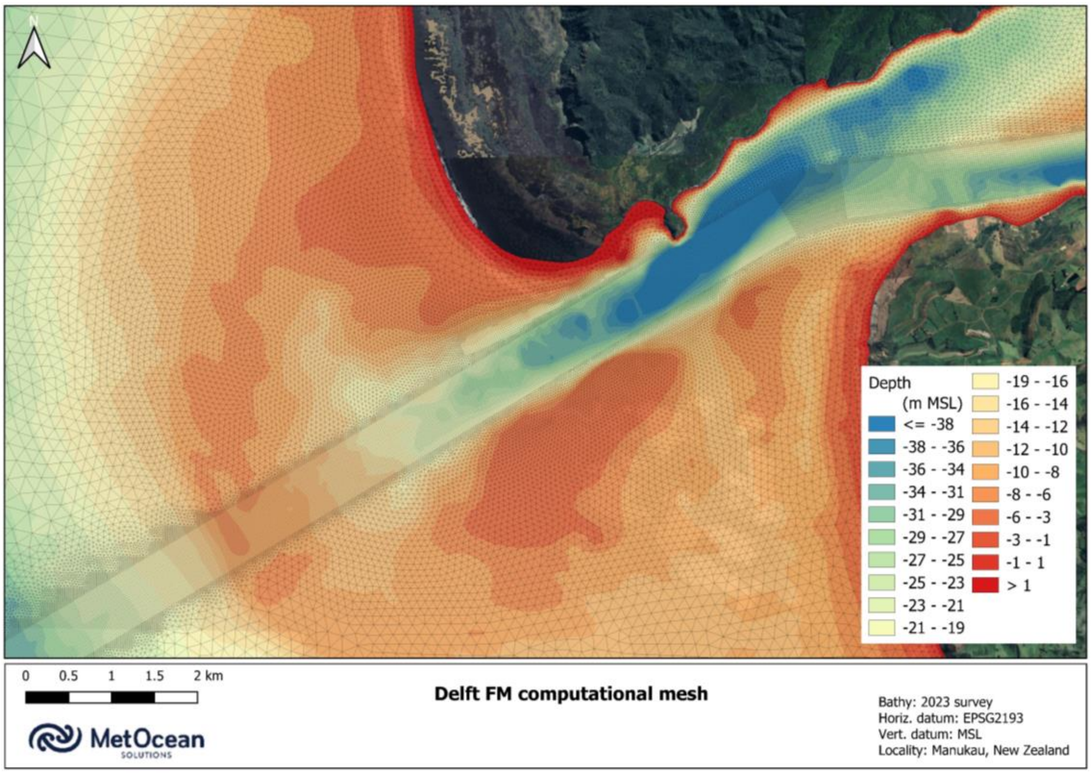

Figure 3-2 Delft FM computational mesh of Manukau Harbour entrance with the existing 2023 bathymetry of the entrance bar and channel.

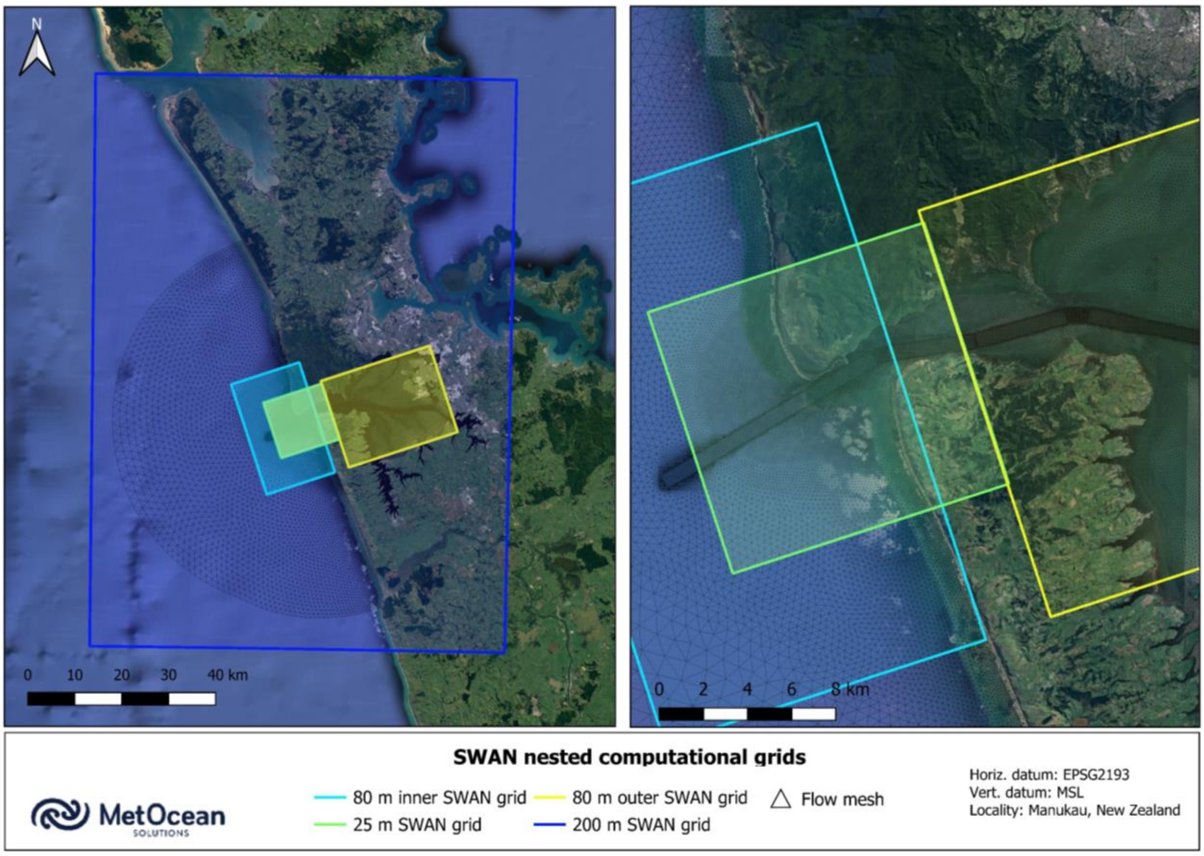

Figure 3-3 Model domains used in the coupled Delft FM/SWAN model runs.

3.2 Model Setup

3.2.1 Bathymetry

The simulations were run for two bathymetry configurations:

- The ‘existing’ bathymetry which was developed from the 2023 survey and used during calibration.
- The channel ‘design’ bathymetry which was the existing 2023 bathymetry with the addition of the South West channel dredged design for the concept navigation channel.

Figure 3-4, Figure 3-5 and Figure 3-6 show the bathymetry used along the concept navigation channel (South West channel). The bathymetries included all the existing bedforms and general morphology of Manukau’s ebb-tidal delta.

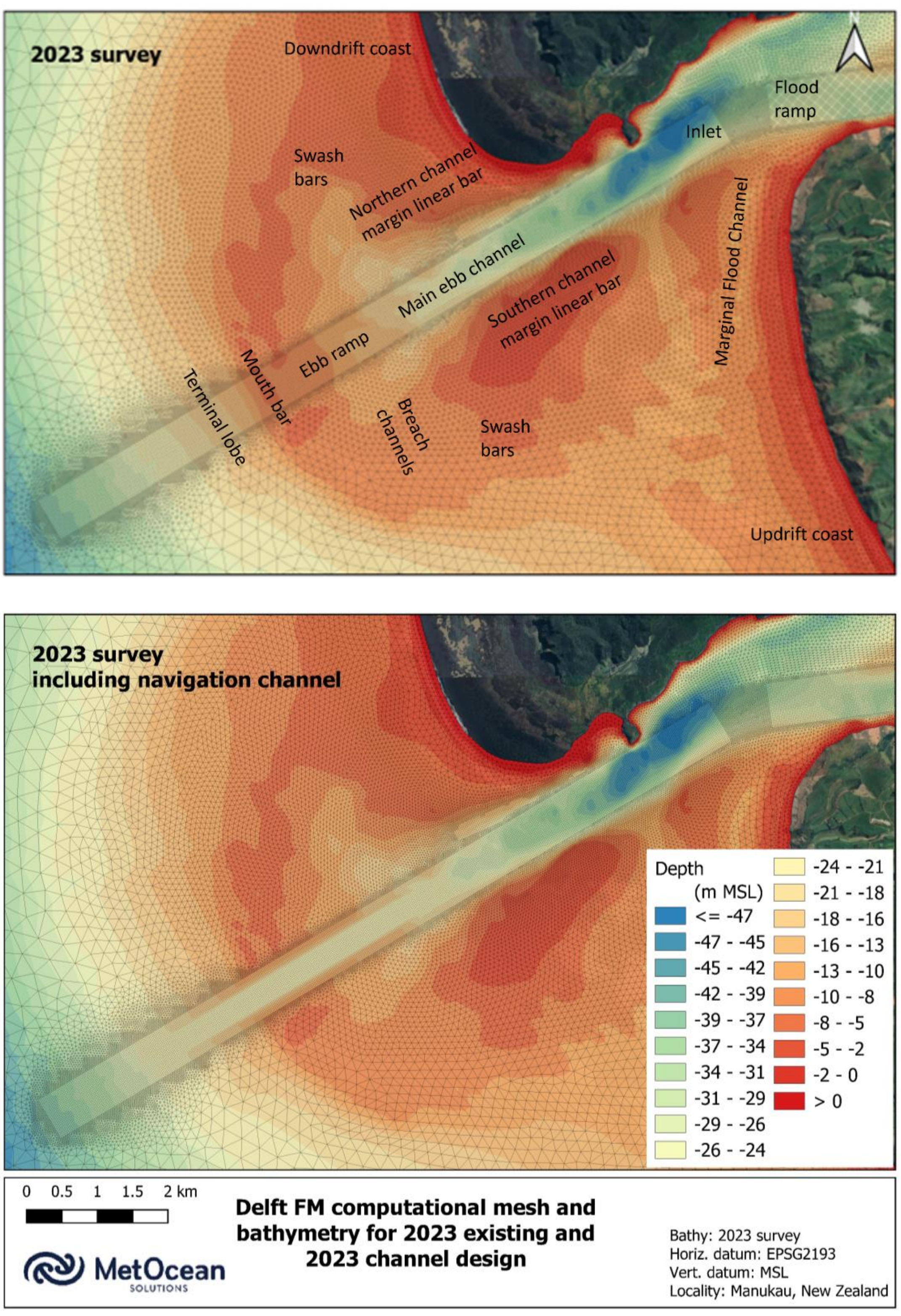

Figure 3-4 Bathymetry used in the 'existing' and channel 'design' model simulations within the entrance channel and bar at Manukau Harbour. Top panel shows main bedforms and general morphology of Manukau ebb-tidal delta.

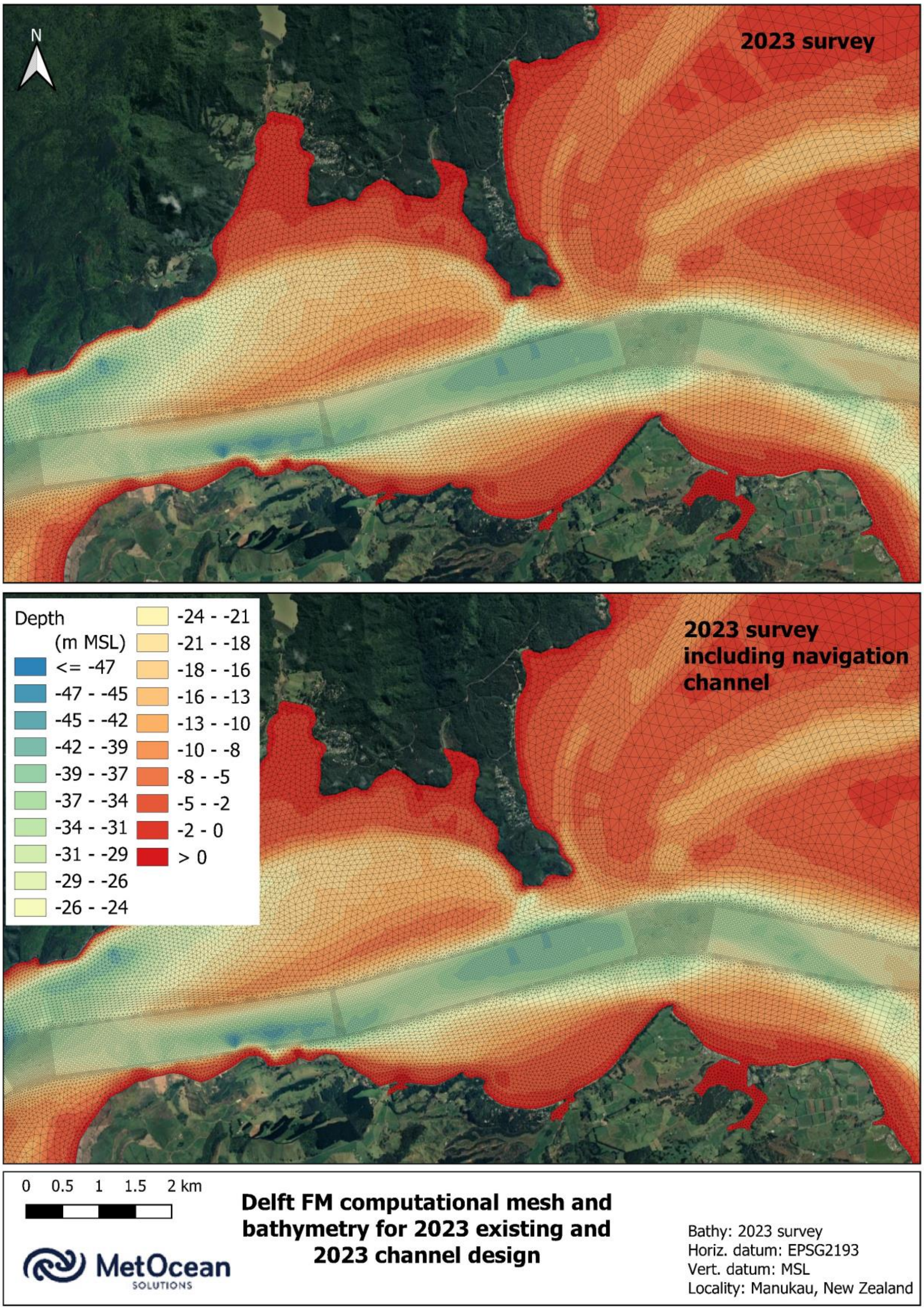

Figure 3-5 Bathymetry used in the 'existing' and channel 'design' model simulations within the entrance channel at Manukau Harbour.

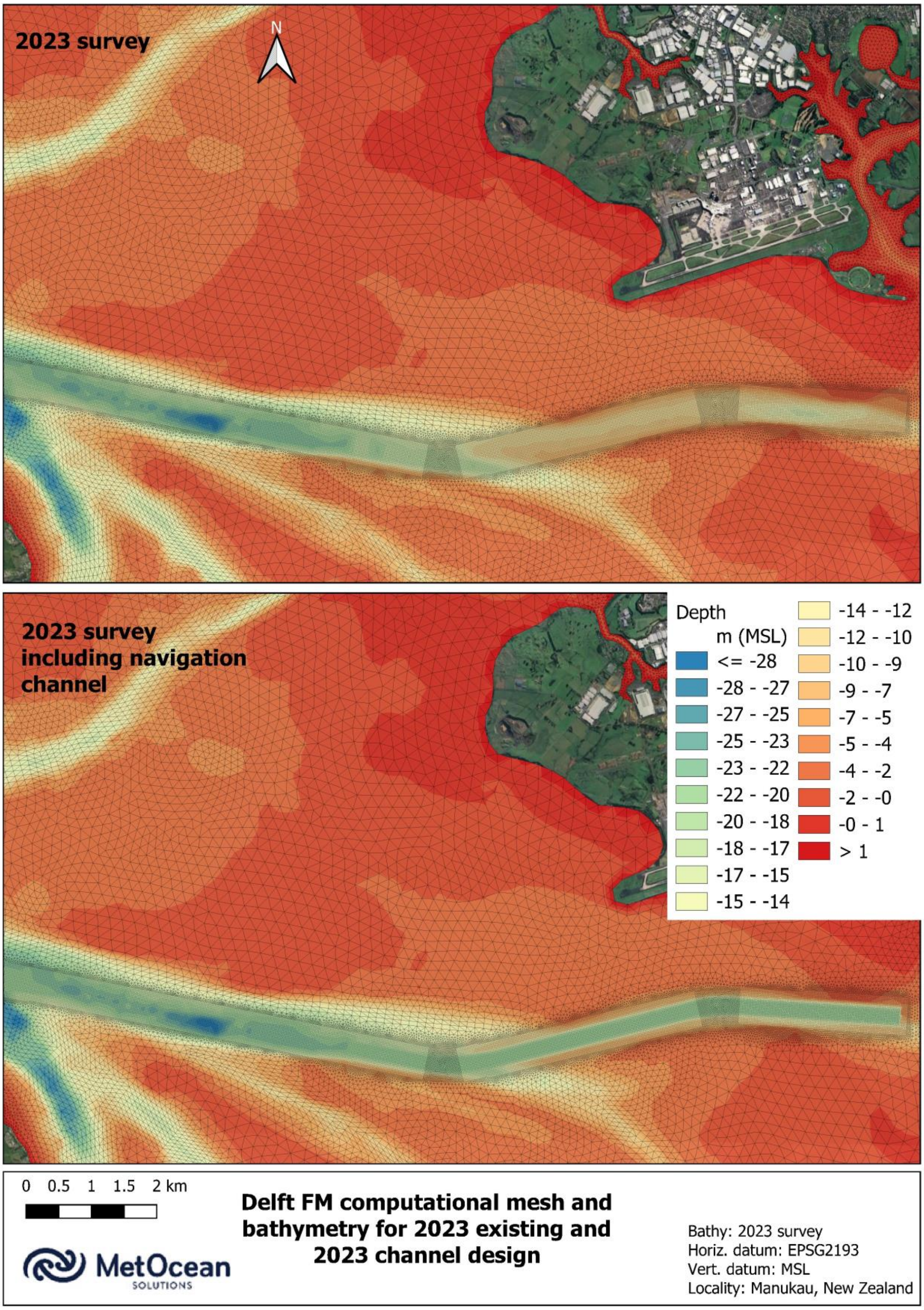

Figure 3-6 Bathymetry used in the 'existing' and channel 'design' model simulations within Manukau Harbour.

3.2.2 Tidal Cases

The different tidal cycles have significant implications for sediment transport. During spring tides, the increased tidal range increases the potential for sediment mobilization and transport, as faster currents exert higher bed shear stress, entraining more sediment and transport it further. During neap tides, reduced tidal range may result in lower sediment transport rates due to slower currents resulting in reduced entrainment and reduced advection of entrained sediment. Understanding the variations in sediment movement during these different tidal conditions is essential for accurately predicting sediment transport dynamics in coastal environments.

In our simulations, we considered three different tidal conditions: spring tide, neap tide, and average 'typical' tide (Figure 3-7). All simulations started at low tide and covered a 12-hour period. The ebbing phase of the spring tide showed a prolonged ebb, and the model simulation did not extend to cover the final hour of this ebb phase in order to standardize it as a 12-hour run and ensure consistency with the other runs. Section 4.3 provides some discussion on the implications of extending the spring tide runs to a 13-hour run to cover the final hour of ebbing.

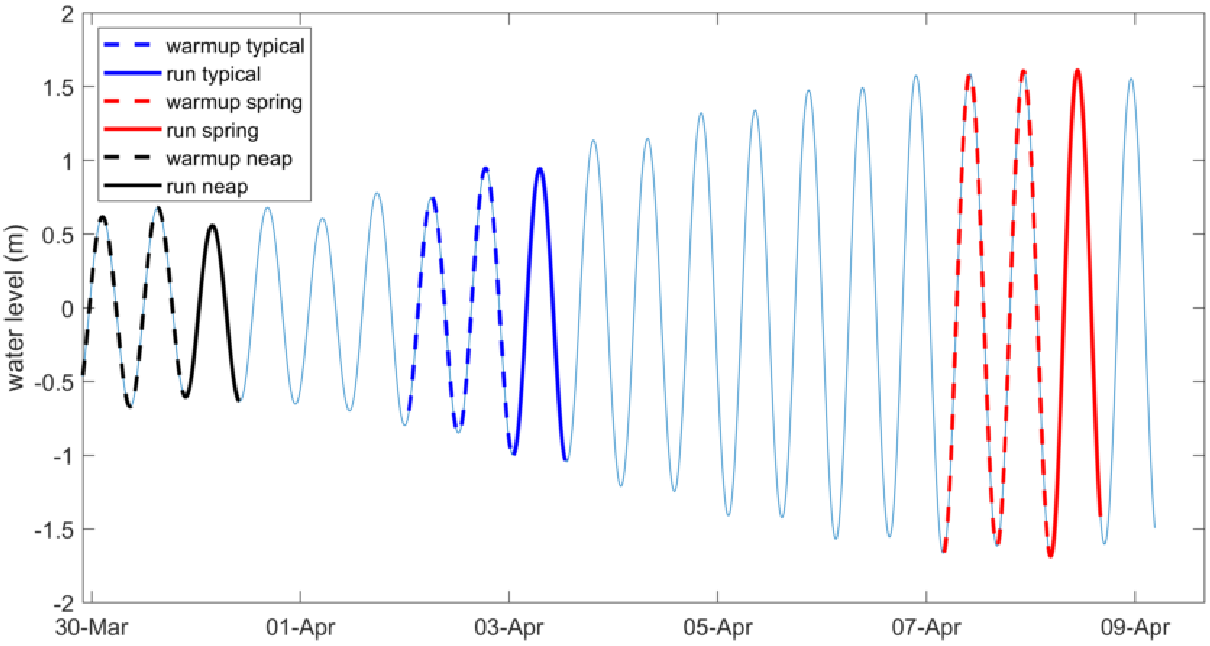

Figure 3-7 Different tidal stages applied in the sediment transport simulations.

3.2.3 Sediment

The present study considered a single sand fraction of 250 μm for our initial runs (control scenarios listed in Table 4-1) and an initial uniform sediment layer of 5 m. Average D50 for all samples collected in the Manukau Harbour and bar is 275 μm (Table 2-1). The particle density used was 3,000 kg/m^3, with a dry bed density set at 1,800 kg/m^3 and a porosity of 0.4.

The Delft3D sediment transport module integrates the effects of waves, currents and sediment transport on the morphological development. At each computational time step the model computes both bedload and suspended load sediment transport components within the model domain. The bed level (if morphological update is activated) and sediment thickness layers are then updated as a result of the sediment sink and sources terms and computed transport gradients. The model is designed to simulate wave propagation, currents, sediment transport and morphological developments in coastal, river and estuarine areas (Deltares, 2014). Note that our simulations included only non-cohesive ('sands') sediments.

The transfer of sediment between the bed and the flow is modelled using sink and source terms acting on the near-bed layer. Bedload and equilibrium suspended load transport resulting from the combined effect of waves and currents can be modelled by a range of formulations, among which are Engelund-Hansen, Meyer-Peter-Muller, Bijker, Bailard and Van Rijn. The streamwise and transverse bed slope effects on the magnitude and direction of transport are also included in the model. General formulations are presented in Appendix A.

For the sediment transport calculations, we adopted the TRANSPOR2004 formula. The TRANSPORT2004 model distinguishes between bedload and suspended-load transport and includes the effects of waves. In the Delft model, radiation stresses and sediment transport are not directly related. Radiation stresses are just the extra momentum flux because waves are present. The model uses radiation stress gradients to calculate wave driven currents, and these drive surf zone sediment transport. The model also takes into account stokes drift for bedload, and lastly, wave orbital velocities are used in the stirring of sediment if the transport formula under consideration allows for it.

A detailed description of the TRANSPOR2004 model is provided in van Rijn et al. (2004). The input parameters used in the model to predict the sediment dynamics over Manukau are summarised in Table A-1 in Appendix A.

We ran additional scenarios using a combination of three different sediment particle sizes (150, 250, and 500 μm) to assess their effect on transport patterns. Based on the sediment samples presented in Section 2.2, we tested different proportions of these fractions, to achieve an overall combination similar to the D50 of the measured particle size distribution (Figure 3-8). First, we distributed the three particles by multiplying a factor related to the spatially varying depth (or current speed), which will influence the spatial distribution of particle sizes - e.g., coarser particles were predominantly found in samples collected from deeper areas of the main channel where the fastest current speeds were simulated. Subsequently, we combined the distribution due to depth and current speed by applying weights to the distributions. The best distribution (in terms of resemblance with the D50 of sediment samples) was achieved by giving 20% weight to the depth and 80% to the current speed.

In addition, sensitivity tests were conducted employing single-fraction uniform layers of 150 and 500 µm, similarly to the original runs using 250 µm, increasing our understanding of the sediment transport dynamics within the studied system.

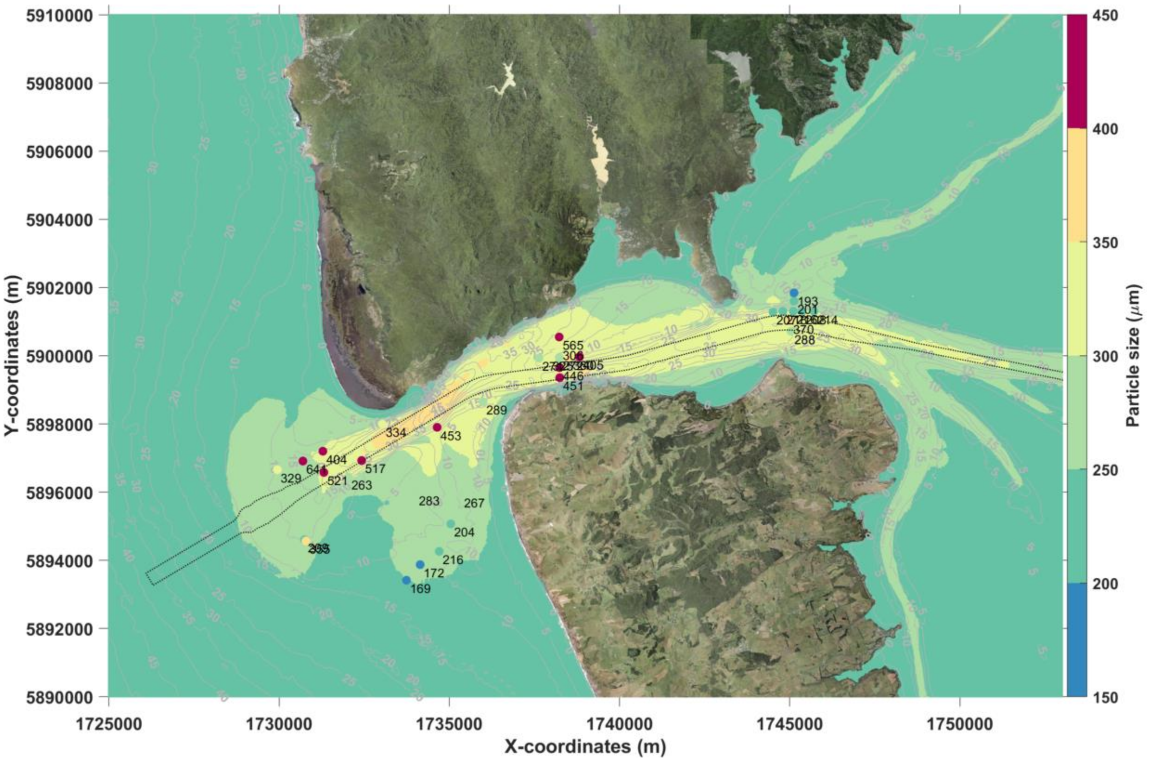

Figure 3-8 Map of average D50 based on layers of variable thickness of particle sizes 150, 250, and 500 µm. Dots represent the locations of sediment samples and their corresponding D50 values.

3.2.4 Model Verification

3.2.4.1 Field Measurement

Very limited data is available to calibrate and validate the sediment transport model mainly from the difficulties associated with collecting a sufficient number of samples to accurately represent the sediment distribution in this highly dynamic system.

Tonkin & Taylor deployed a sediment catcher device at 1 m above the seabed which collected suspended material for a period of time. Together with the catcher, a drag tilt sensor was used to infer current flow passing through the sampler. The trapped material was subsequently weighed. The approximate location of the deployment is shown in Figure 3-9 and the details related to the catcher are presented in Table 3-1. Full description of deployment is presented in TWP02 – Fieldwork Report.

Our model was setup in two-dimensional (2D) and therefore, to be able to compare the concentration of suspended material from the field, we estimated the distribution of suspended sediment concentration through the water column using a standard Rouse profile (Figure 3-10), as indicated in the equation below (van Rijn et al., 2004).

$$c^{(l)} = c_a^{(l)} \left[\frac{a(h-z)}{z(h-a)}\right]^{A^{(l)}}$$

Equation 3-1

where: $c^{(l)}$ is the concentration of sediment fraction (l), $c_a^{(l)}$ is the reference concentration of sediment fraction, a is the van Rijn's reference height, h is the water depth, z is the elevation above the bed, and $A^{(l)}$ is the Rouse number, a non-dimensional number used to define a concentration profile of suspended sediment, defined in Equation 3-2.

Model output provided the reference height a and the reference concentration $c_a^{(l)}$. Assuming the concentration in the centre of the kmx layer c_{kmx} is the depth-averaged concentration given by the model output and considering the centre of the water column z_{kmx} half the total depth 0.5 h, the exponent $A^{(l)}$ can be determined. We also tested z_{kmx} to be 0.4 h as a sensitivity test, without significant changes in the results.

$$A^{(l)} = \frac{ln\left(\frac{c_{kmx}}{c_a}\right)}{ln\left(\frac{a(h-z_{kmx})}{z_{kmx}(h-a)}\right)}$$

Equation 3-2

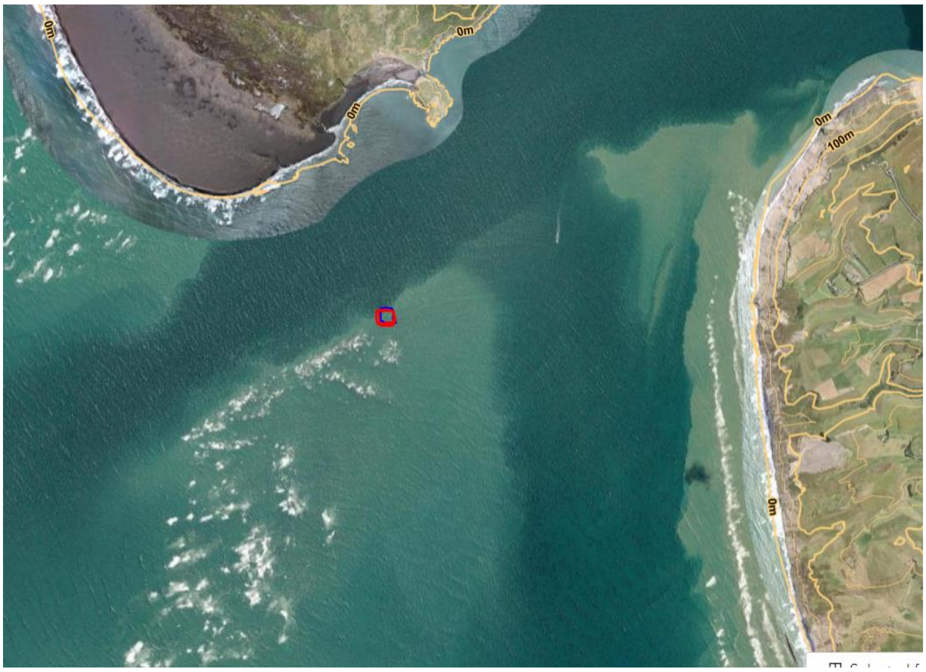

Figure 3-9 Approximate location of the deployment of the suspended material sampler.

Table 3-1: Details of fieldwork deployment, sampler, and collected material.

Time (NZDT)	10:30 am
Tidal stage	30 min after mid-incoming
Tidal amplitude	Spring
Local depth	15 m
Deployment time	6 min
Weight of material collected	180 g
Sampler opening width	0.07 m
Sampler opening height	0.147 m
Current velocity (average)	1.4 m/s
Height opening centre above bed	1.0735 m
Area across sampler opening	0.01029 m^2
Flow rate through sampler	0.014406 m^3/s
Flow volume through sampler	5.18616 m^3
Average concentration	**34.7 g/m^3 (0.0347 kg/m^3)**

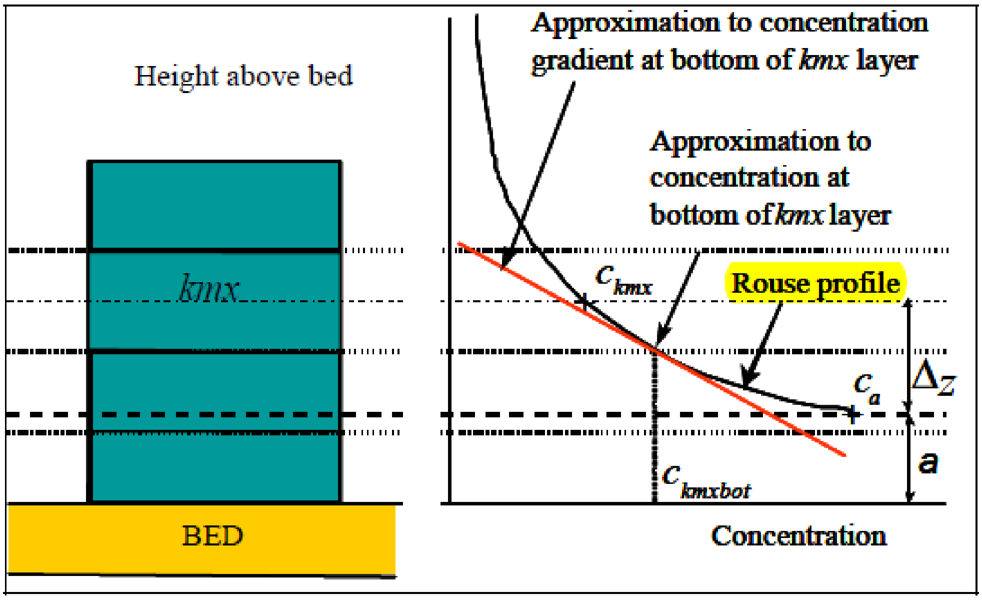

Figure 3-10 Schematic representing the kmx layer and the concentration gradient approximated by a Rouse profile (source: van Rijn et al., 2004).

Based on the deployment time, tidal stage and amplitude during the field sampling, we selected a control run (Control 04), which best replicated the hydrodynamic conditions observed in the field, representing a spring tide with waves (refer to Table 4-1 for run details).

We chose a model node near the deployment location that best matched the water depth during the sampling and selected a model timestep corresponding to the field sampling period (Figure 3-11).

Significant variations in the modelled sediment concentration were observed during the simulation time. The green line shows the approximate time of field sampling. It is important to acknowledge that due to bathymetric gradients and model interpolation, the selected model node may not perfectly represent the actual field conditions. As a comparison, we plotted sediment concentrations (kg/m^3) for two sites (red and blue lines in Figure 3-12) around the field deployment location.

Using the modelled sediment concentration at the chosen timestep, we derived a water-column distribution of sediment concentration using the Rouse profile (Figure 3-13). The estimated concentration at 1 m from the seabed (same height as the sampler) is approximately 0.0321 kg/m^3, compared to 0.0347 kg/m^3, the concentration derived from the sampler (Table 3-2). This comparison shows a close match between field and model results. However, as shown in Figure 3-12, the time of sampling does not occur at peak concentrations. Consequently, it is not guaranteed that the comparison would yield good results under peak transport conditions.

As shown in Figure 3-12, the time of deployment (relative to the tidal stage) did not coincide with the time of highest concentrations (in the model).

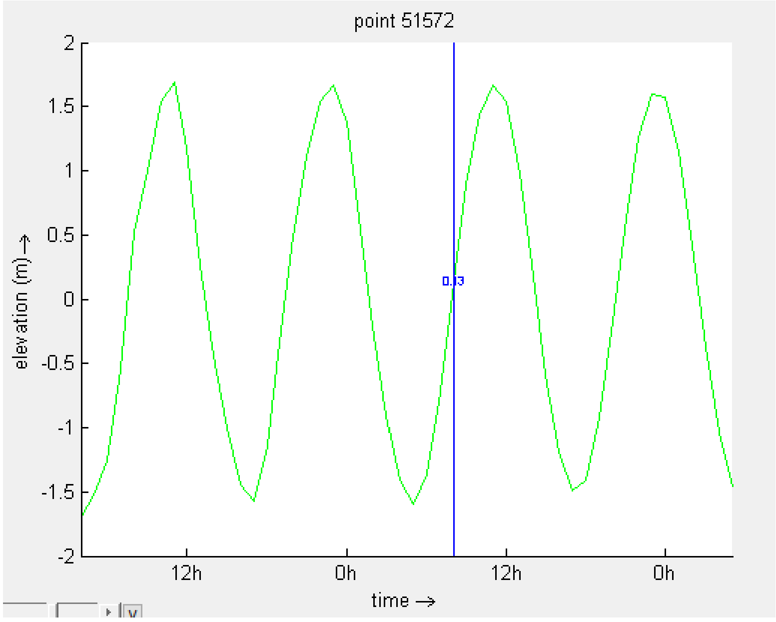

Figure 3-11 Water level during model simulation (green line) and time step chosen to represent the time of the field sampling (blue line).

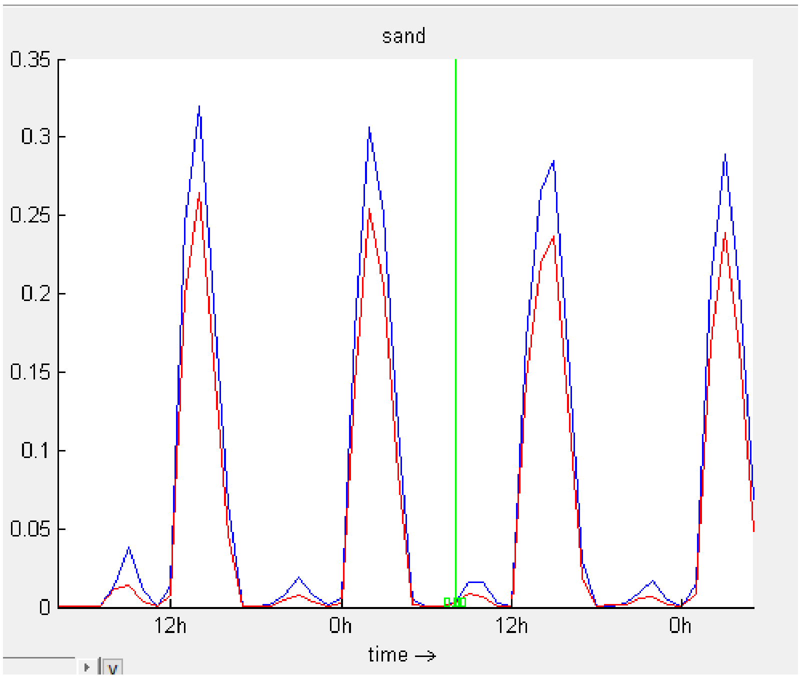

Figure 3-12 Sediment concentration (kg/m^3) for two sites next to each other (red and blue lines) near the approximate location of field deployment. Green line represents the time of field sampling.

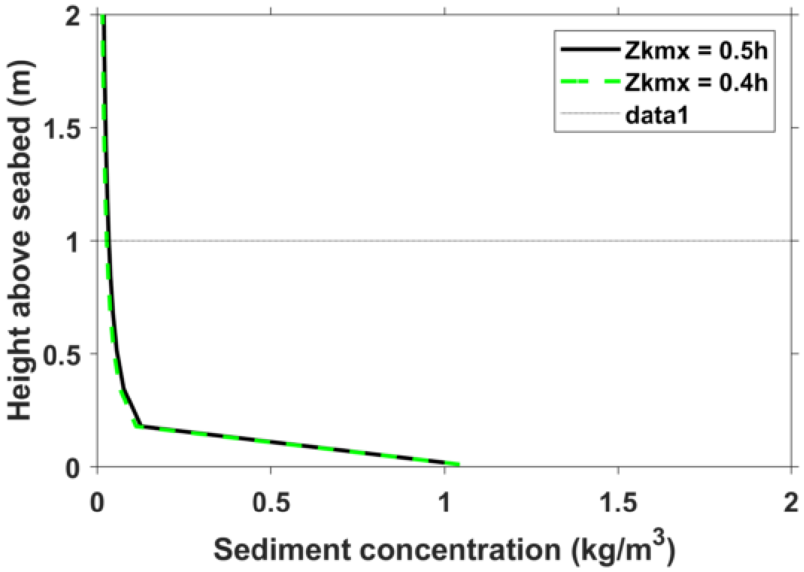

Figure 3-13 Sediment concentration (kg/m^3) profile for the approximate time of field deployment. Black line was calculated using zkmx = 0.5h and green using zkmx = 0.4h.

Table 3-2: Sediment concentration model vs. field.

	Height above bed	**Concentration**
Model	1.017m	0.0321 kg/m3
Field	1.074m	0.0347 kg/m3

3.2.4.2 Empirical Longshore Sediment Transport Rate

An alternative approach for verifying the sediment transport model, involves the use of empirical formulas typically derived from laboratory and field data.

Tonkin & Taylor applied a widely recognized formula, described in Kamphuis (2000), to compute longshore sediment transport rates. The parameters used in the calculation are listed in Table 3-3. The process includes wave refraction/shoaling from offshore to breaking point according to Goda (2007).

Sediment transport rates were estimated using a 40-year high-resolution wave hindcast. The results indicated a predominant northward transport, driven by local wave conditions. Transport rate was also calculated at an open coast location, situated far from the influence of the mouth and tidal flow, using wave conditions from specific control runs (Table 4-1), to allow comparison with model results.

Transport rates derived from the model results were extracted at approximately the same location as the open coast used in empirical calculations. Additionally, transport rates were extracted at two locations situated immediately to the north and south of the ebb channel.

For scenarios with waves coming from the southwest (e.g., Control 3 and 14 in Table 3-4), the model results showed net northward transport for transects north of the channel and at the open coast transect, agreeing with the expected pattern from the empirical model. The direction of transport is reversed for the scenario forced by northwest waves (Control 6). Our results showed that south of the channel, the transport is southward for the three runs, attributed to the ebb tide flow, as evident in the transport maps and the conceptual model (Section 4.4).

The magnitude of transport for the location south of the channel is greater than that observed at the open coast and north of the channel (Table 3-4). Although the modelled rates at the open coast location were lower than the empirical findings, considering the simplification of the empirical formula relative to the numerical model, the comparison produced reasonable results.

Table 3-3: Sediment transport parameters used in the empirical formula calculations.

Shoreline orientation	245 degrees
Grain size	250 microns
Porosity	0.4
Gamma	0.6
Density of particle	3000 kg/m^3
Surf-zone slope	0.007 (1V:140H)

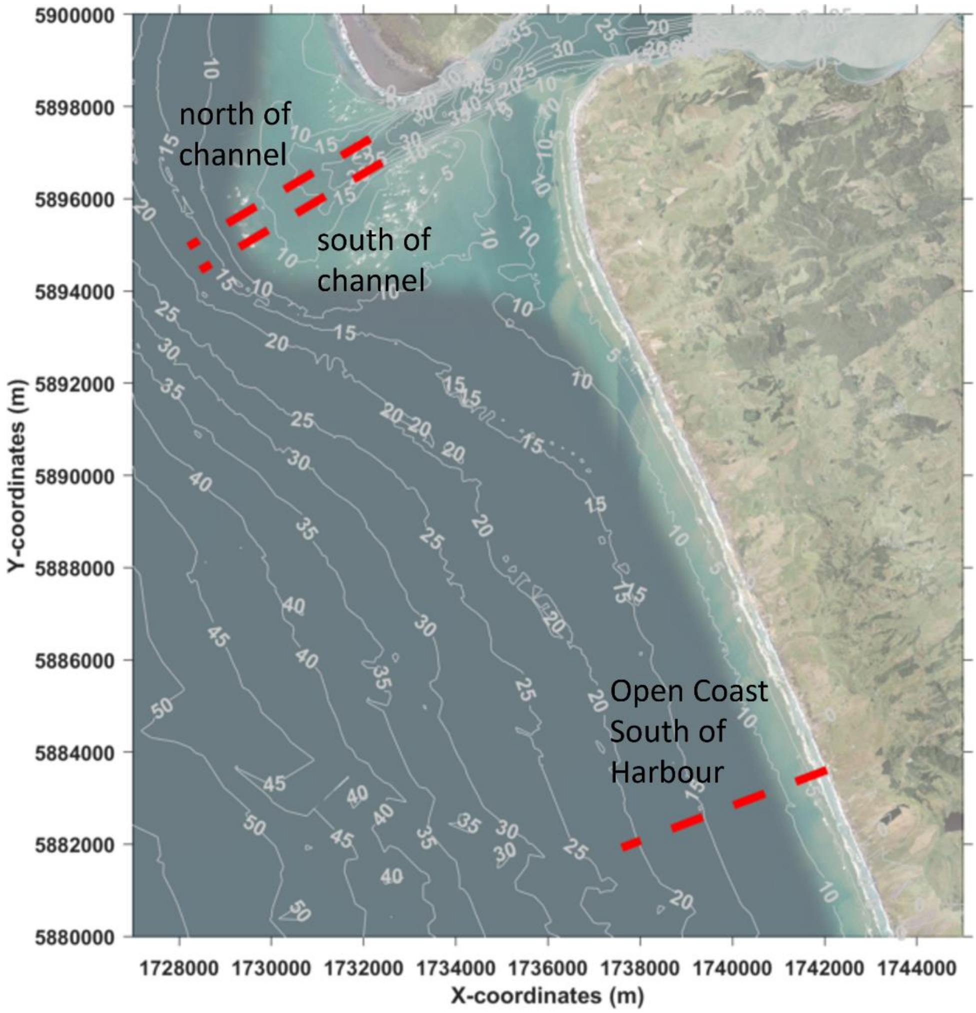

Figure 3-14 Location of transects used to extract model results of sediment transport rates. The open coast location is approximately at the same location as that used for the empirical calculations.

Table 3-4: Sediment transport rates at 3 locations for different scenarios and rates calculated using empirical formula (Kamphuis, 2000).

Scenario	**Flux north of channel (m^3/s)**	**Flux south of channel (m^3/s)**	**Flux Open Coast South of Harbour (m^3/s)**	**Kamphuis LS transport south of entrance (m^3/s)**
Control 3 (H_s 5 m, T_p 15 s, Dir 230)	0.10	-0.14	0.08	0.28
Control 6 (H_s 5 m, T_p 15 s, Dir 230)	-0.07	-0.31	-0.10	-0.20
Control 14 (H_s 5 m, T_p 11 s, Dir 230)	0.08	-0.14	0.06	0.14
IR01 (H_s 5 m, T_p 11 s, Dir 225)	0.13	-0.11	0.09	0.19
IR02 (H_s 4 m, T_p 10 s, Dir 225)	0.02	-0.15	0.05	0.11
IR03 (H_s 3 m, T_p 8 s, Dir 225)	0.00	-0.13	0.01	0.04
IR04 (H_s 7 m, T_p 12 s, Dir 230)	0.21	0.17	0.17	0.36
IR05 (H_s 6 m, T_p 12 s, Dir 230)	0.10	0.03	0.11	0.27
IR06 (H_s 5 m, T_p 11 s, Dir 230)	0.06	-0.02	0.08	0.17
IR07 (H_s 4 m, T_p 10 s, Dir 230)	0.02	-0.15	0.04	0.09
IR08 (H_s 3 m, T_p 9 s, Dir 230)	0.00	-0.15	0.02	0.04
IR09 (H_s 2 m, T_p 12 s, Dir 230)	0.00	-0.11	0.00	0.04
IR10 (H_s 7 m, T_p 13 s, Dir 235)	-0.06	-0.09	0.11	0.33
IR11 (H_s 6 m, T_p 12 s, Dir 235)	0.05	-0.05	0.07	0.22
IR12 (H_s 5 m, T_p 15 s, Dir 235)	0.11	-0.14	0.04	0.23
IR13 (H_s 4 m, T_p 15 s, Dir 235)	-0.01	-0.25	0.02	0.15
IR14 (H_s 3 m, T_p 14 s, Dir 235)	-0.01	-0.19	0.01	0.08
IR15 (H_s 2 m, T_p 13 s, Dir 235)	0.00	-0.11	0.00	0.03
IR16 (H_s 5 m, T_p 16 s, Dir 240)	-0.09	-0.27	0.01	0.18
IR17 (H_s 4 m, T_p 15 s, Dir 240)	-0.02	-0.27	0.00	0.10
IR18 (H_s 3 m, T_p 15 s, Dir 240)	-0.01	-0.19	0.00	0.06
IR19 (H_s 5 m, T_p 14 s, Dir 250)	-0.02	-0.22	-0.06	-0.14
IR20 (H_s 4 m, T_p 13 s, Dir 250)	-0.02	-0.21	-0.03	-0.08
IR21 (H_s 3 m, T_p 12 s, Dir 250)	-0.02	-0.18	-0.01	-0.04
IR22 (H_s 7 m, T_p 14 s, Dir 260)	-0.98	-0.79	-0.20	-0.48
IR23 (H_s 6 m, T_p 12 s, Dir 260)	-0.28	-0.46	-0.13	-0.27
IR24 (H_s 5 m, T_p 11 s, Dir 260)	-0.09	-0.32	-0.08	-0.17
IR25 (H_s 4 m, T_p 10 s, Dir 260)	-0.04	-0.24	-0.05	-0.09
IR26 (H_s 3 m, T_p 9 s, Dir 260)	-0.01	-0.15	-0.02	-0.04
IR27 (H_s 4 m, T_p 10 s, Dir 270)	-0.05	-0.25	-0.06	-0.12

4 Manukau Bar Sediment Transport Patterns

4.1 Control Scenarios

Our first aim for this study was to better understand sediment transport processes near the entrance bar of Manukau Harbour. To do so we selected some metocean conditions that would enable us to visualise the main sediment transport patterns. A total of 17 control scenarios were considered as presented in Table 4-1. Some of these scenarios were also used for sensitivity testing and analysis and therefore rerun with different sediment fractions or with additional wind forcing.

Presented below (Figure 4-1 to Figure 4-8) are results from a typical control scenario (Control 3). In this scenario, the 2023 'existing' (no concept navigation channel) bathymetry was applied, with wave boundary conditions characterized by H_s = 5 m, T_p = 15 s and Dir = 230 deg.

Results were extracted every 3 hours to illustrate different stages of the tide: flood, high, ebb and low tide. Here we present maps of wave height and direction, current magnitude and direction, sediment concentration, and erosion/deposition including transport direction.

Around the bar, especially during flood tide, we observe currents and transport towards the shore, flowing in the main South West channel, the South Channel and around the north and south banks (Figure 4-1 and Figure 4-2). High erosion and deposition rates occur around the mouth bar and banks. During the ebb and low tide, stronger currents in the main ebb channel create a counter flow within the main channel, pushing sediment offshore (Figure 4-5). This counter flow encounters the incoming waves at the mouth bar, leading to a dynamic interaction with high erosion and deposition rates and causes the flow to deflect north and south through the breach channels between the lateral bars of the main channel and the mouth bar.

In the case which the concept navigation channel is included (i.e., Control 7, Figure 4-9 to Figure 4-16), the transport within the channel is oriented offshore, resulting in increased erosion within the channel near the bar area, thereby driving sediment deposition just offshore of this region. The difference in deposition and erosion at the end of the 12-h simulation between ‘existing’ (Control 3) and ‘channel’ (Control 7) is illustrated in Figure 4-17, bottom panel. It is important to note that the differences identify areas that are responding to the different configurations (i.e., without or with the channel).

The map of difference in deposition between “existing” and “channel” configurations (Figure 4-17, bottom left) indicates that, when the channel is considered in the bathymetry, sediment tend to accumulate more on both sides of the channel on the bar, and on the terminal lobe. There is also comparatively more accumulation further onshore within the main ebb channel, however the area in between the batter slopes is mainly less depositional.

In terms of erosion between “existing” and “channel” configurations (Figure 4-17, bottom right) the map shows that there is less erosion on the terminal lobe when the channel is present (as this was an area dominated by deposition). The majority of the erosion occurs at the mouth bar. Details on the relationship between the erosion/deposition features and the main sediment transport patterns are presented in Section 4.4.

Table 4-1: Control Scenario parameters.

Scenario	Bathy	Tide	H_s (m)	T_p (s)	D_p (˚N)	Notes
Control 1	2023 existing	Typical	0	0	0	Test on tidal infill
Control 2	2023 channel	Typical	0	0	0	Test on tidal infill
Control 3	2023 existing	Typical	5	15	230	Control - existing
Control 4	2023 existing	Spring	5	15	230	Effect of tide
Control 5	2023 existing	Neap	5	15	230	Effect of tide
Control 6	2023 existing	Typical	5	13	260	Test NW dir
Control 7	2023 channel	Typical	5	15	230	Control - channel
Control 8	2023 channel	Spring	5	15	230	Effect of tide
Control 9	2023 channel	Neap	5	15	230	Effect of tide
Control 10	2023 channel	Typical	5	13	260	Test NW dir
Control 11	1989 channel	Typical	5	15	230	Effect of bathy - SW
Control 12	1989 channel	Typical	5	13	260	Effect of bathy - NW
Control 13	1989 existing	Typical	5	15	230	Control - existing
Control 14	2023 existing	Typical	5	11	230	Control - existing
Control 15	2023 channel	Typical	5	11	230	Control - channel
Control 16	2023 existing	Typical	2	12	230	Typical condition existing
Control 17	2023 existing	Typical	1	7	230	Typical condition existing

“Existing” scenario:

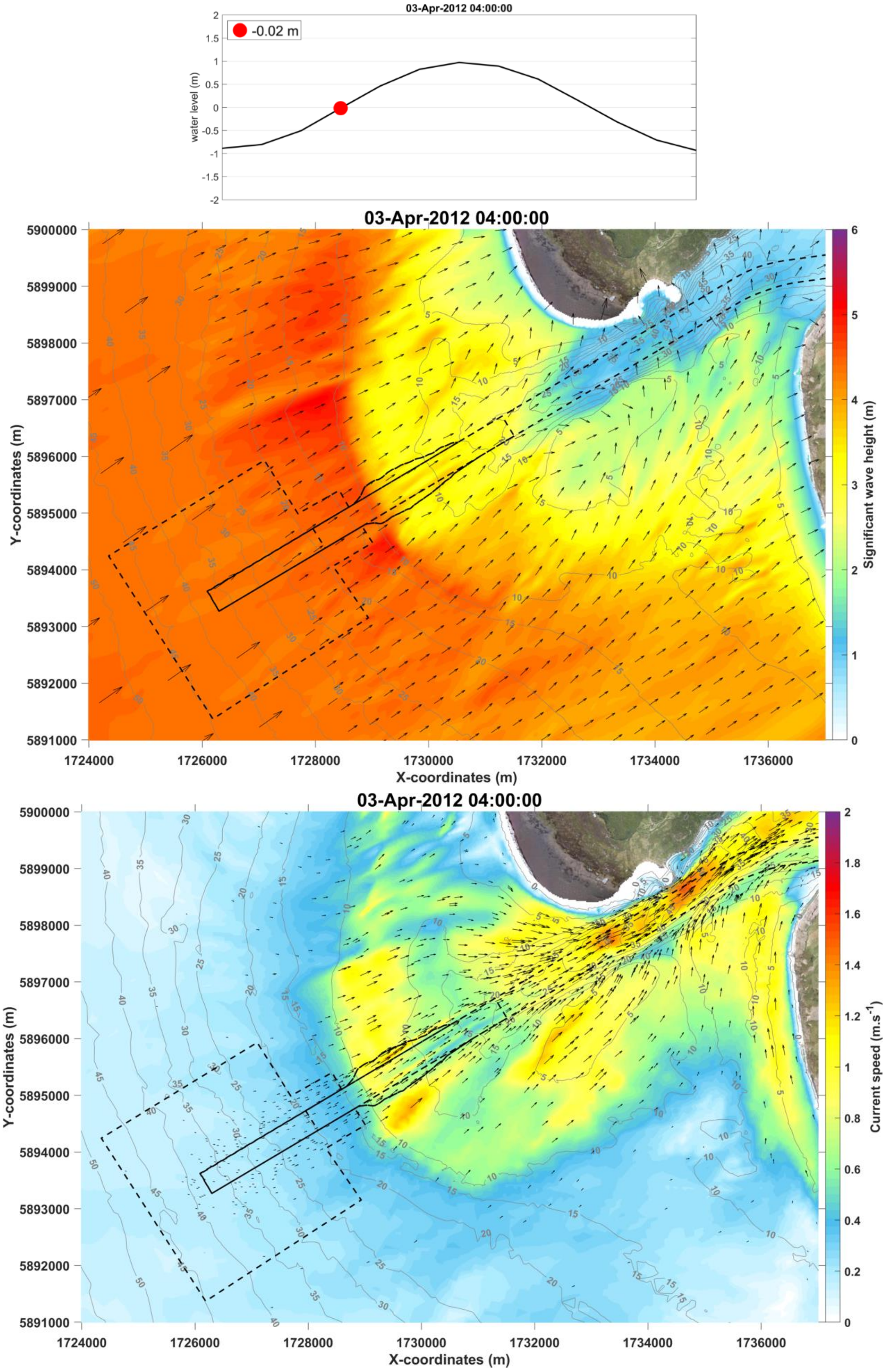

Figure 4-1 Map results of wave (middle panel) and current (bottom panel) magnitude (colormap) and direction (vectors) during the flood tide for Control 3 (H_s = 5 m, T_p = 15 s and Dir = 230 deg). Isobaths illustrate the bathymetry of existing scenario with the position of the concept channel shown as dashed lines in the figures.

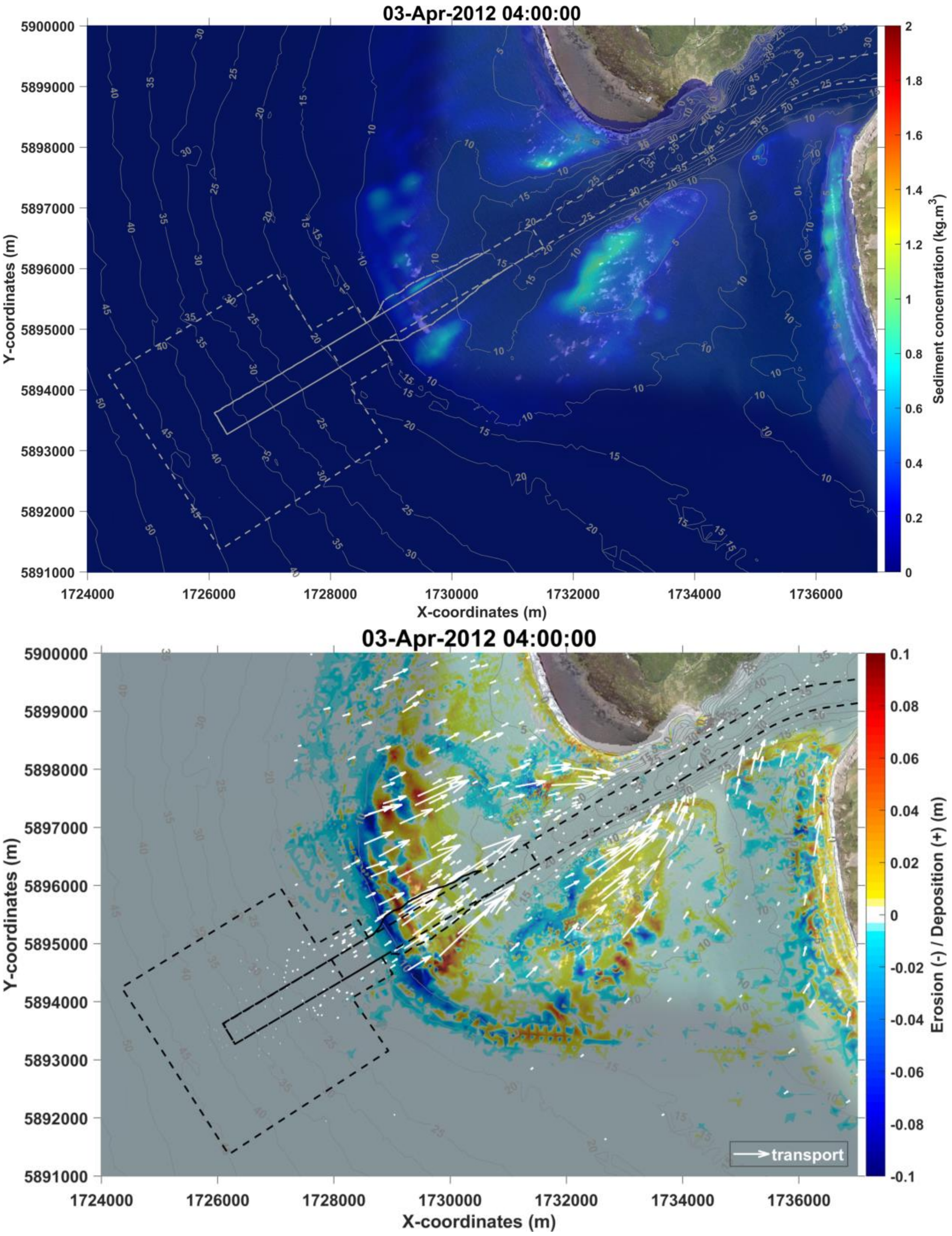

Figure 4-2 Map results of sediment concentration (top panel) and erosion/deposition (bottom panel). For bottom panel: negative values (blue) represent erosion and positive values (red) represent deposition of sediment. White arrows show sediment transport direction. Results during the flood tide for Control 3 (H_s = 5 m, T_p = 15 s and Dir = 230 deg). Isobaths illustrate the bathymetry of existing scenario with the position of the concept channel shown as dashed lines in the figures.

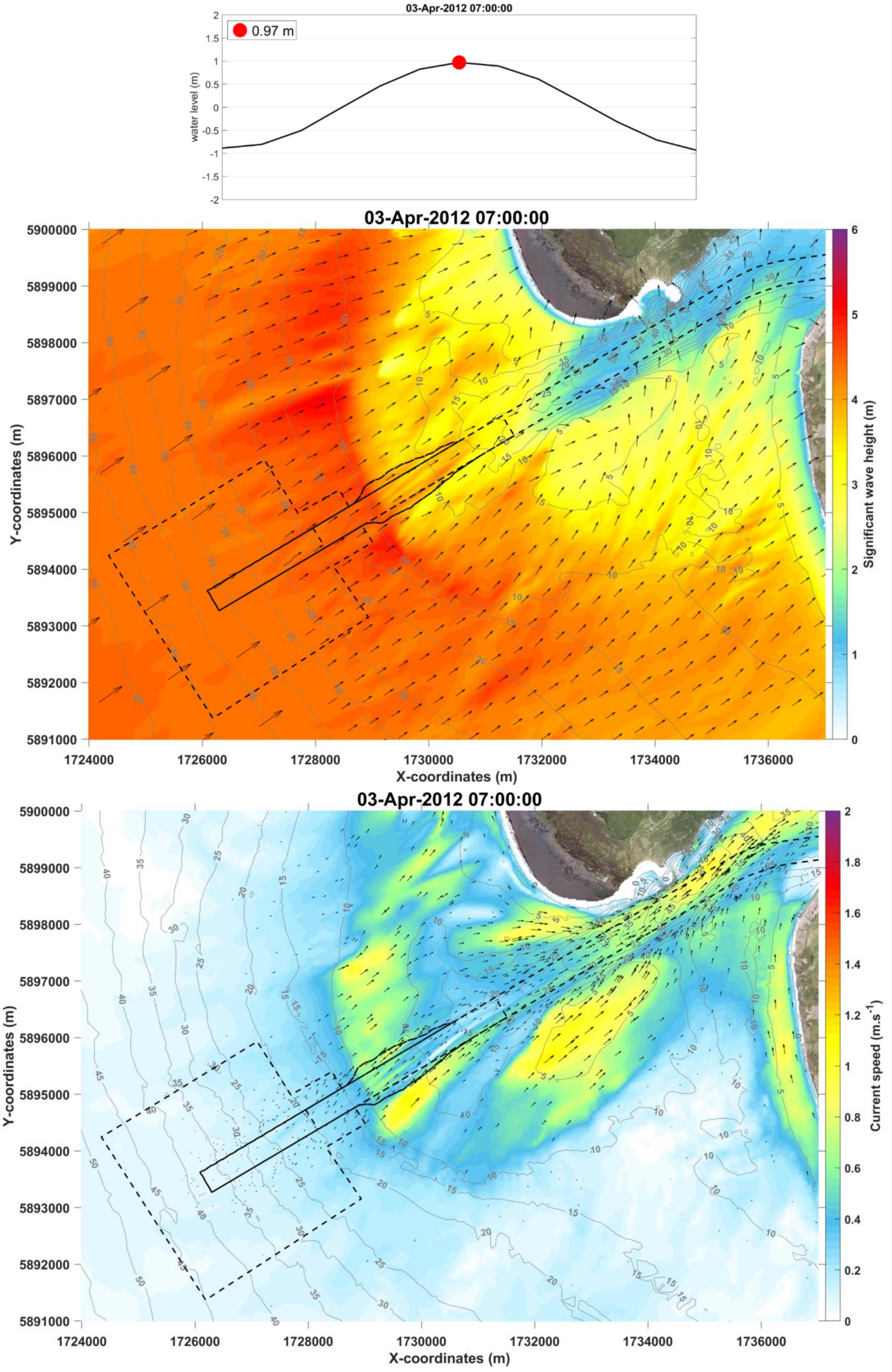

Figure 4-3 Map results of wave (middle panel) and current (bottom panel) magnitude (colormap) and direction (vectors) at high tide for Control 3 (H_s = 5 m, T_p = 15 s and Dir = 230 deg). Isobaths illustrate the bathymetry of existing scenario with the position of the concept channel shown as dashed lines in the figures.

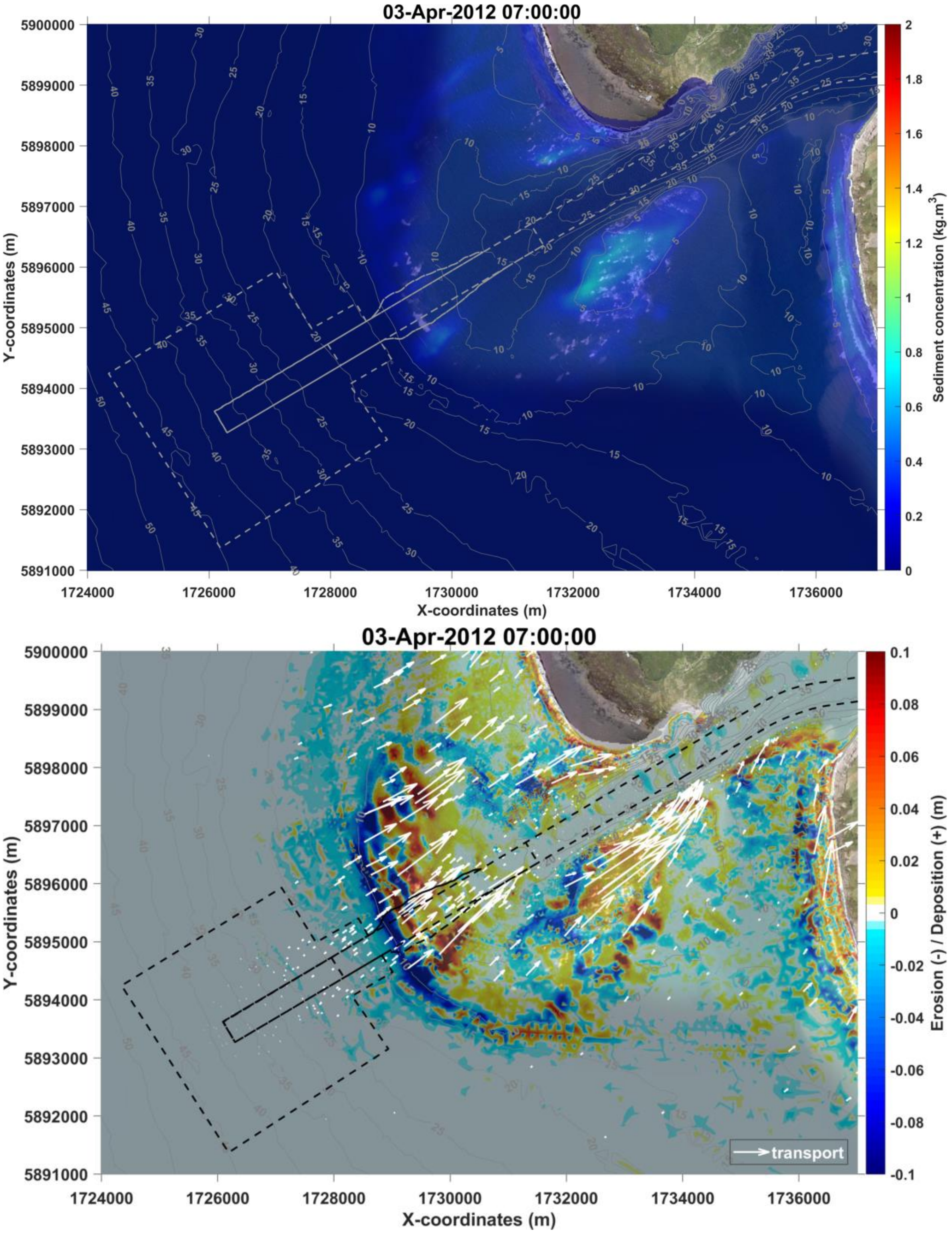

Figure 4-4 Map results of sediment concentration (top panel) and erosion/deposition (bottom panel). For bottom panel: negative values (blue) represent erosion and positive values (red) represent deposition of sediment. White arrows show sediment transport direction. Results at high tide for Control 3 (H_s = 5 m, T_p = 15 s and Dir = 230 deg). Isobaths illustrate the bathymetry of existing scenario with the position of the concept channel shown as dashed lines in the figures.

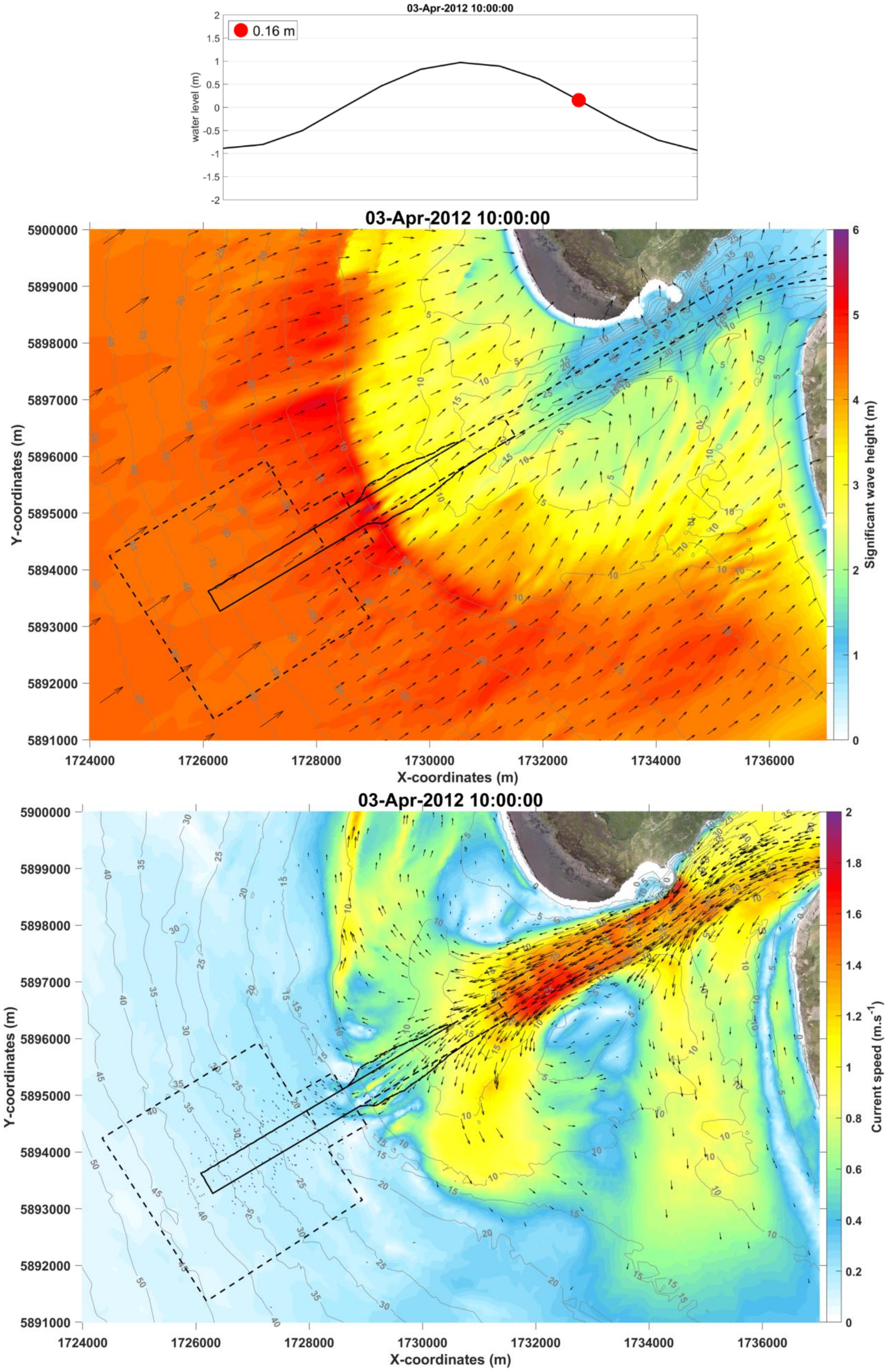

Figure 4-5 Map results of wave (middle panel) and current (bottom panel) magnitude (colormap) and direction (vectors) during the ebb tide for Control 3 (H_s = 5 m, T_p = 15 s and Dir = 230 deg). Isobaths illustrate the bathymetry of existing scenario with the position of the concept channel shown as dashed lines in the figures.

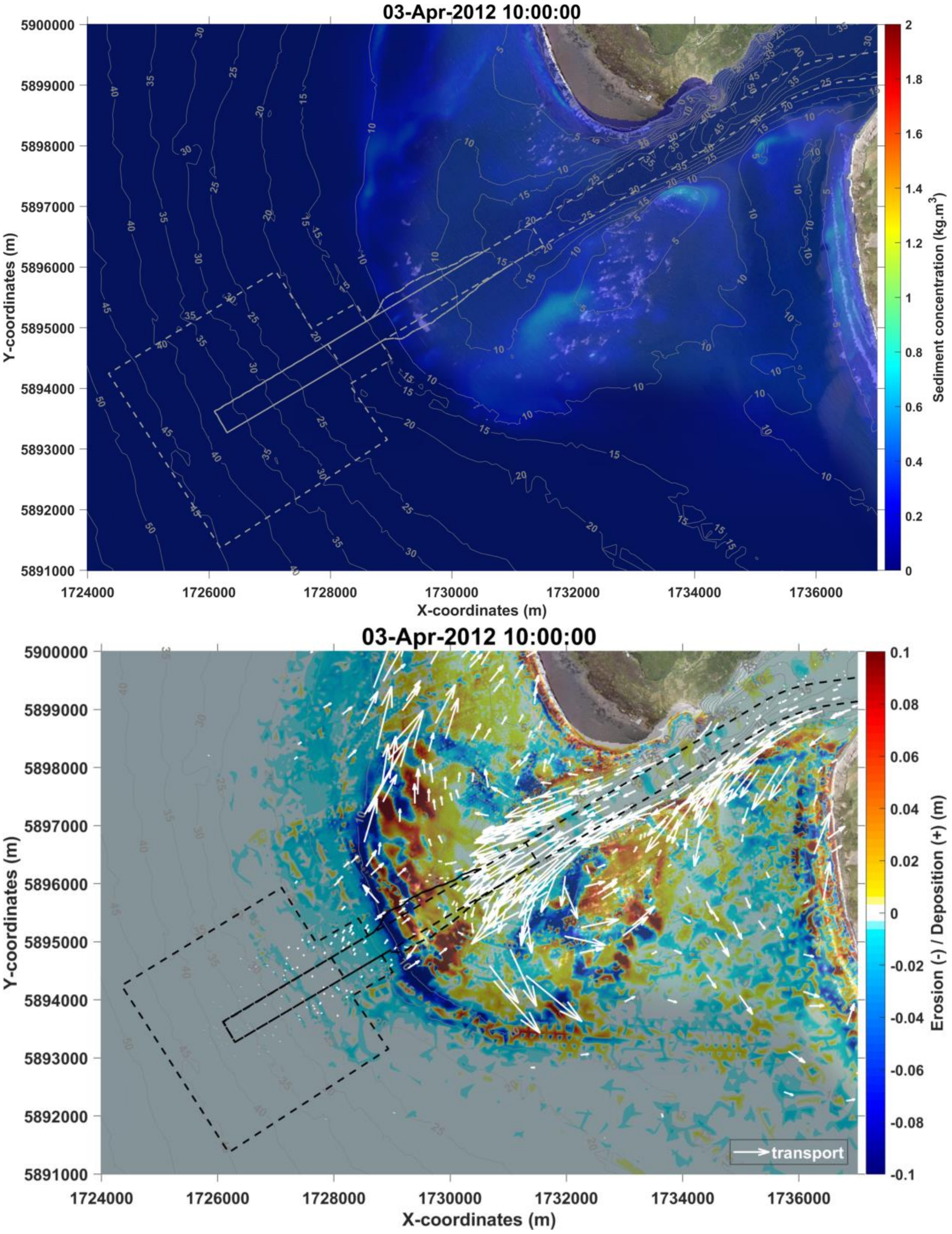

Figure 4-6 Map results of sediment concentration (top panel) and erosion/deposition (bottom panel). For bottom panel: negative values (blue) represent erosion and positive values (red) represent deposition of sediment. White arrows show sediment transport direction. Results during the ebb tide for Control 3 (H_s = 5 m, T_p = 15 s and Dir = 230 deg). Isobaths illustrate the bathymetry of existing scenario with the position of the concept channel shown as dashed lines in the figures.

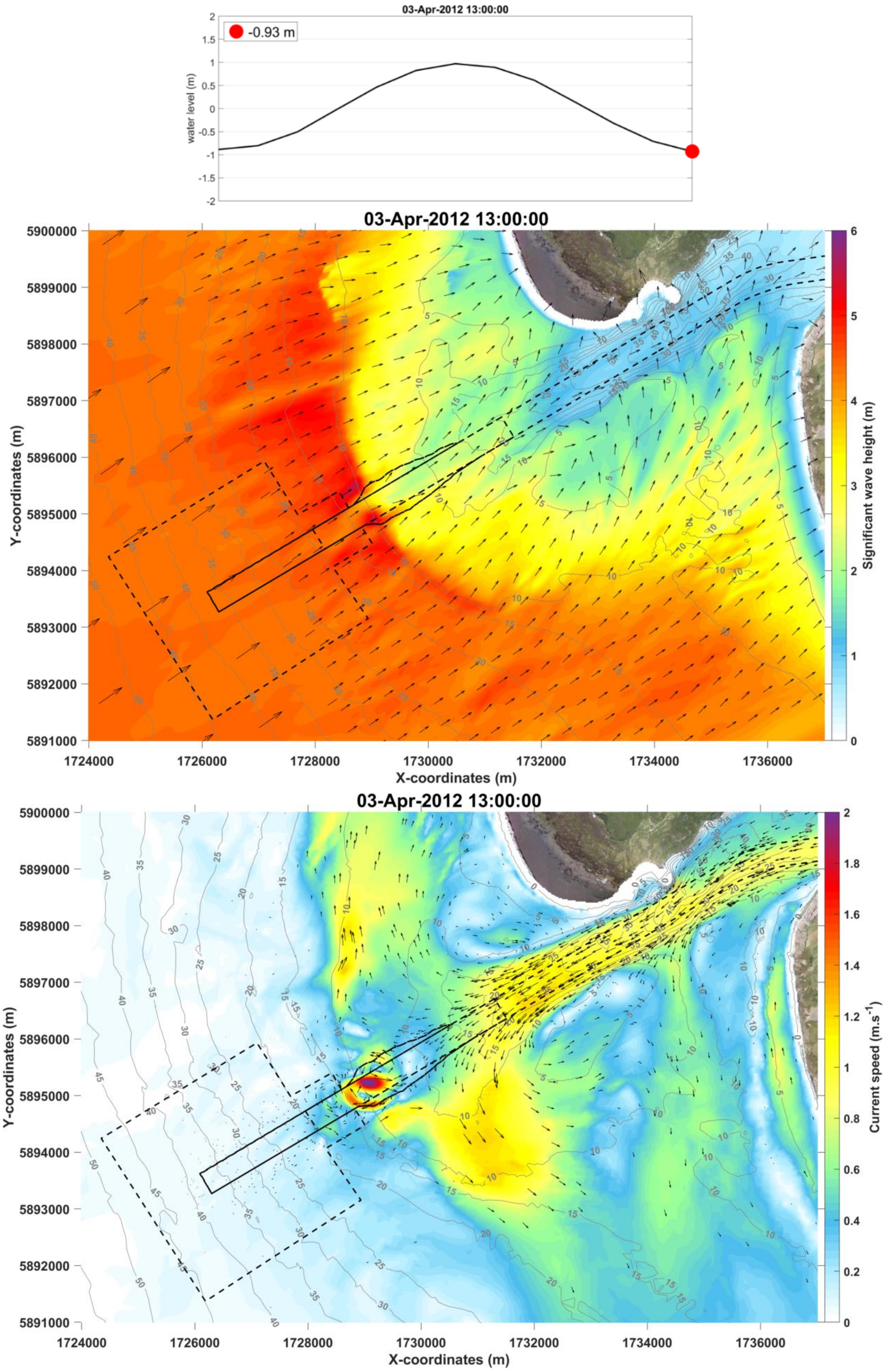

Figure 4-7 Map results of wave (middle panel) and current (bottom panel) magnitude (colormap) and direction (vectors) at low tide for Control 3 (H_s = 5 m, T_p = 15 s and Dir = 230 deg). Isobaths illustrate the bathymetry of existing scenario with the position of the concept channel shown as dashed lines in the figures.

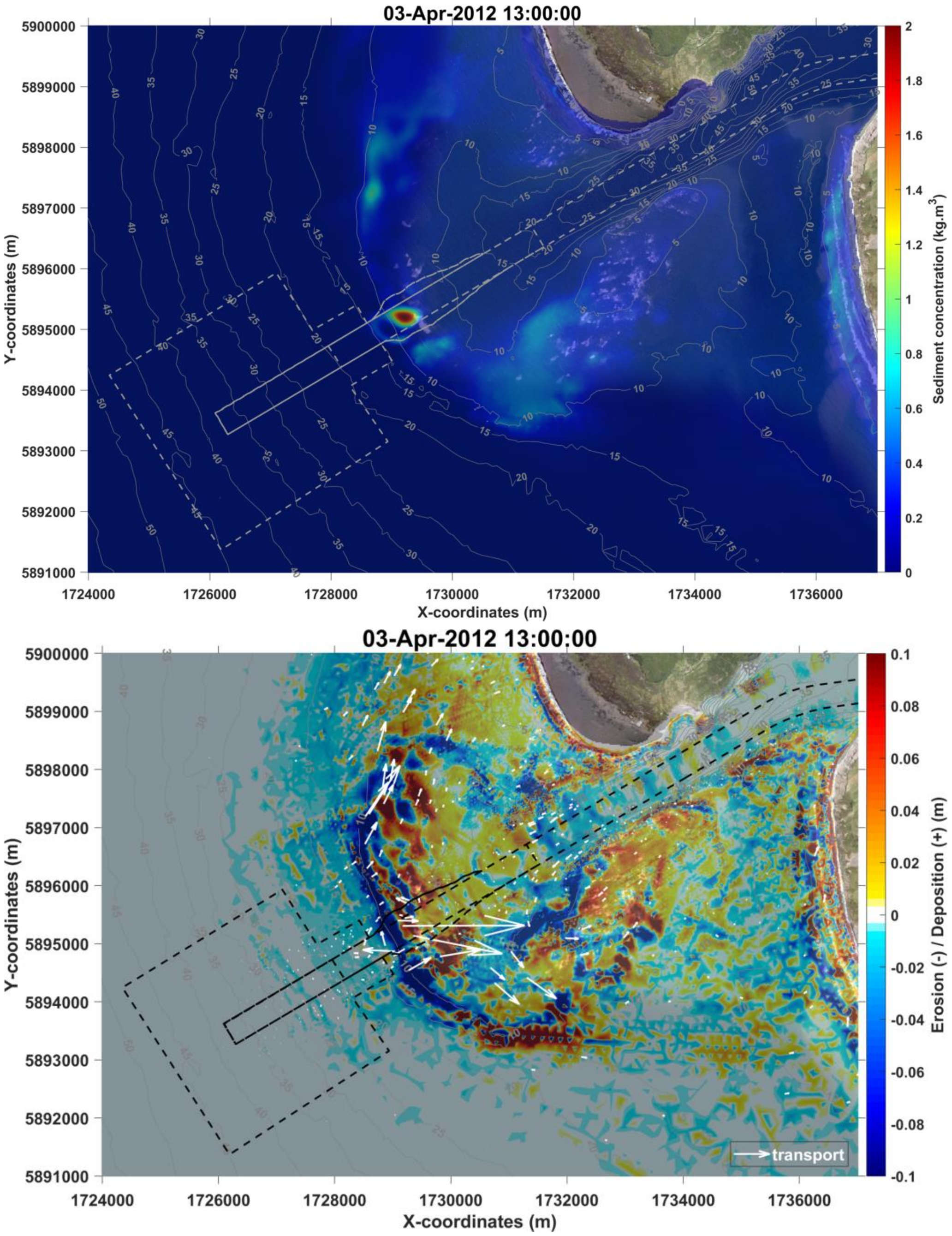

Figure 4-8 *Map results of sediment concentration (top panel) and erosion/deposition (bottom panel). For bottom panel: negative values (blue) represent erosion and positive values (red) represent deposition of sediment. White arrows show sediment transport direction. Results at low tide for Control 3 (H_s = 5 m, T_p = 15 s and Dir = 230 deg). Isobaths illustrate the bathymetry of existing scenario with the position of the concept channel shown as dashed lines in the figures.*

“Channel” scenario:

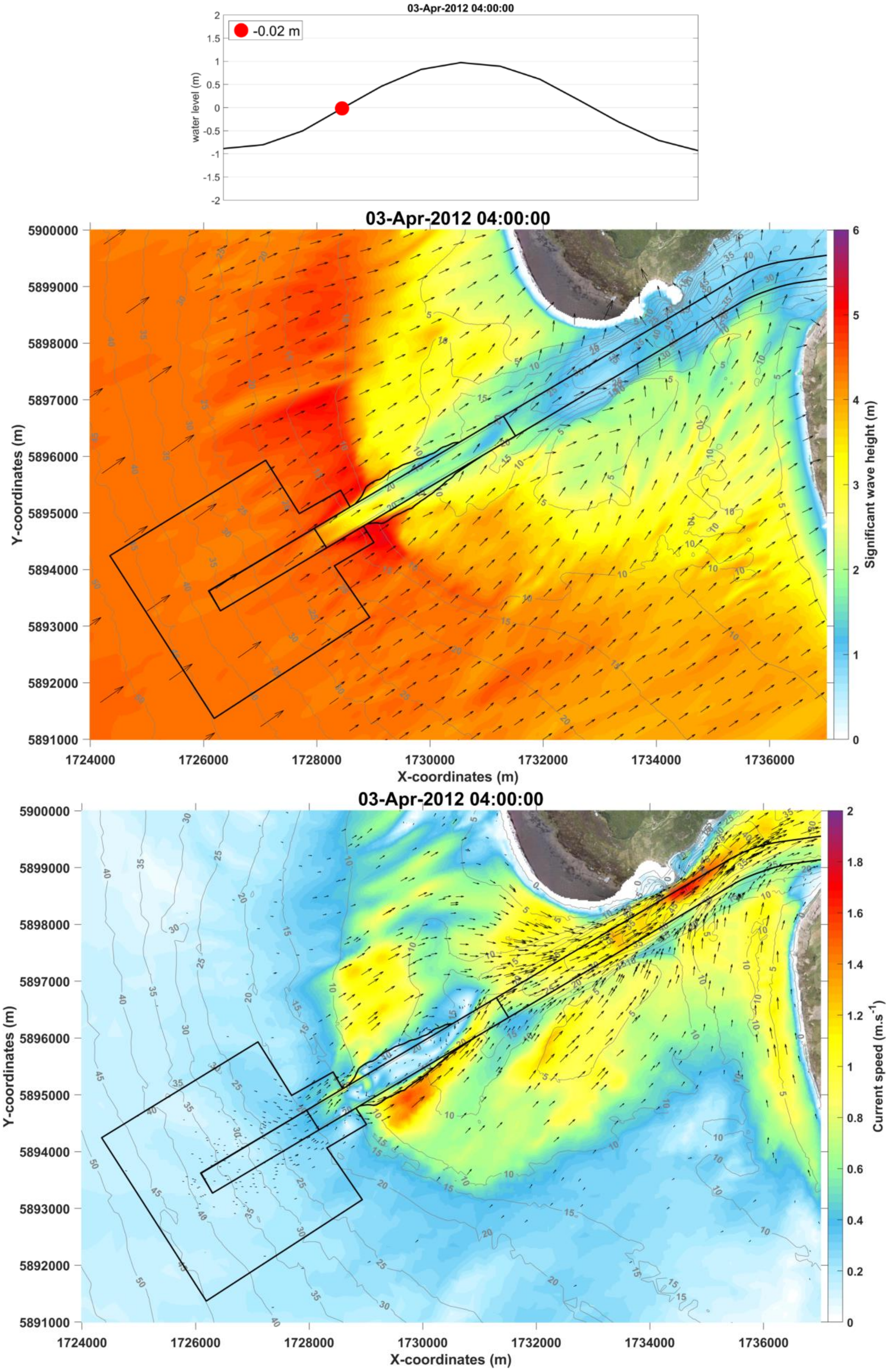

Figure 4-9 Map results of wave (middle panel) and current (bottom panel) magnitude (colormap) and direction (vectors) during the flood tide for Control 7 (H_s = 5 m, T_p = 15 s and Dir = 230 deg). Isobaths illustrate the bathymetry of channel scenario with the position of the concept channel shown as solid lines in the figures.

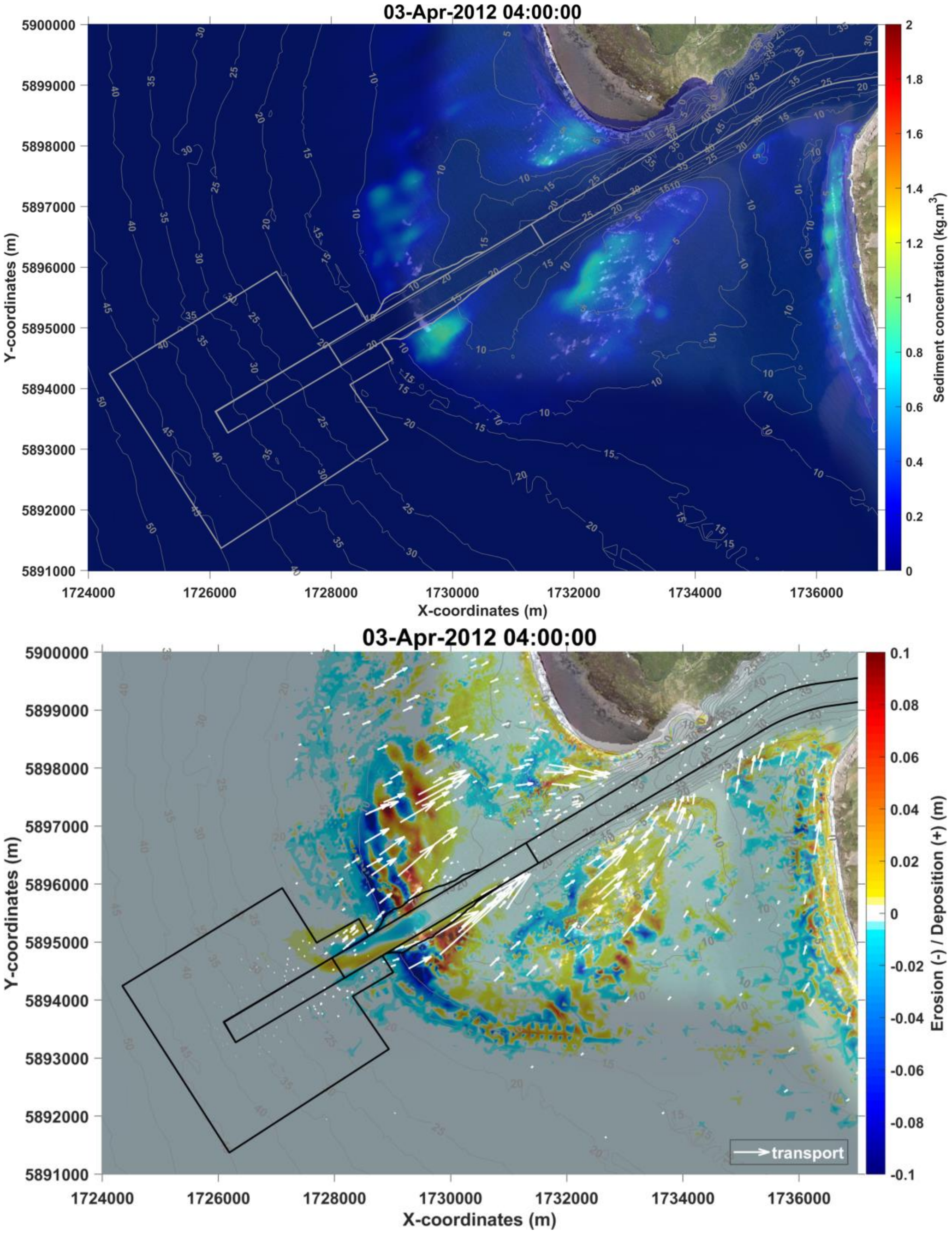

Figure 4-10 Map results of sediment concentration (top panel) and erosion/deposition (bottom panel). For bottom panel: negative values (blue) represent erosion and positive values (red) represent deposition of sediment. White arrows show sediment transport direction. Results during the flood tide for Control 7 (H_s = 5 m, T_p = 15 s and Dir = 230 deg). Isobaths illustrate the bathymetry of channel scenario with the position of the concept channel shown as solid lines in the figures.

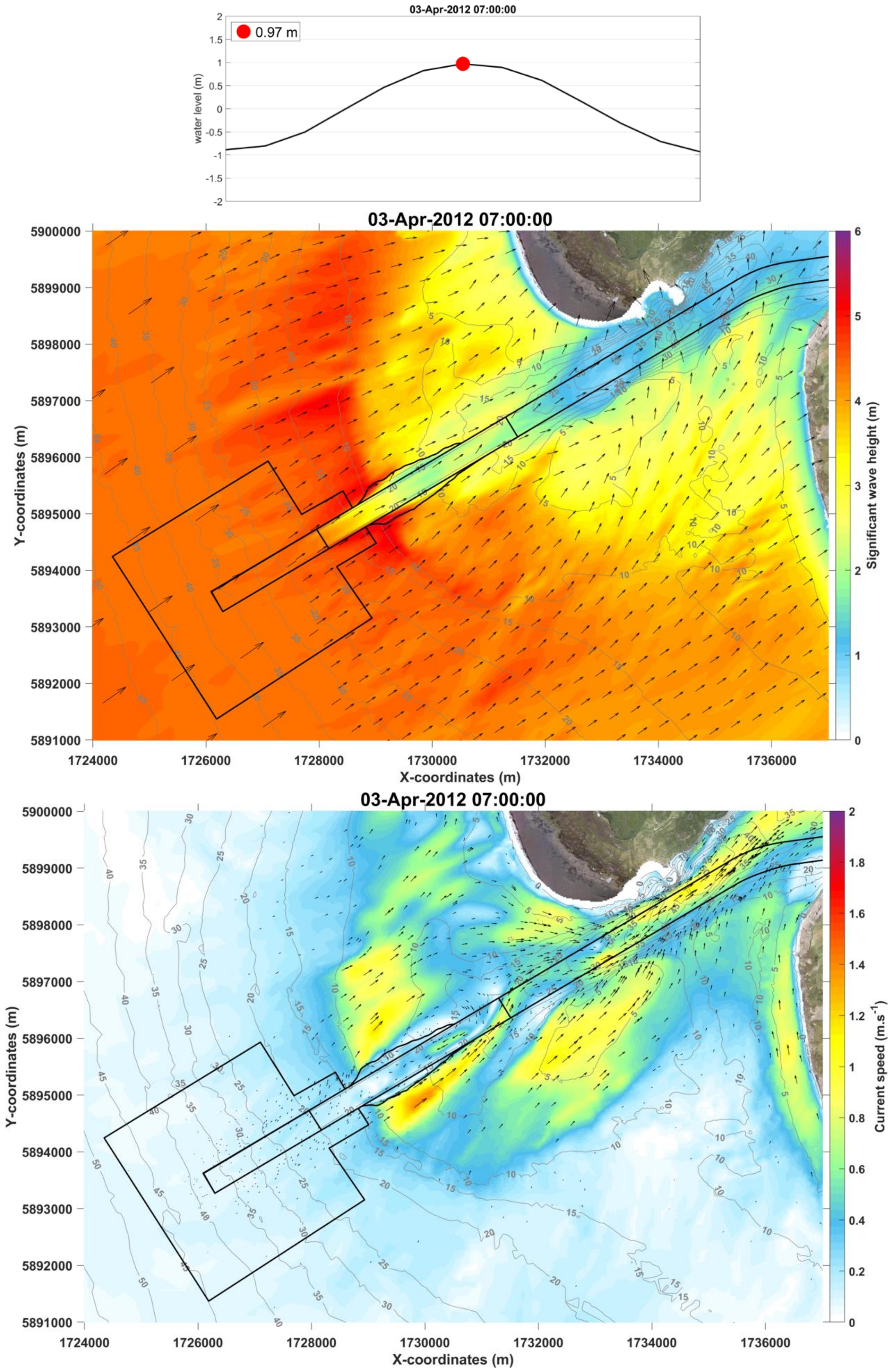

Figure 4-11 Map results of wave (middle panel) and current (bottom panel) magnitude (colormap) and direction (vectors) at high tide for Control 7 (H_s = 5 m, T_p = 15 s and Dir = 230 deg). Isobaths illustrate the bathymetry of channel scenario with the position of the concept channel shown as solid lines in the figures.

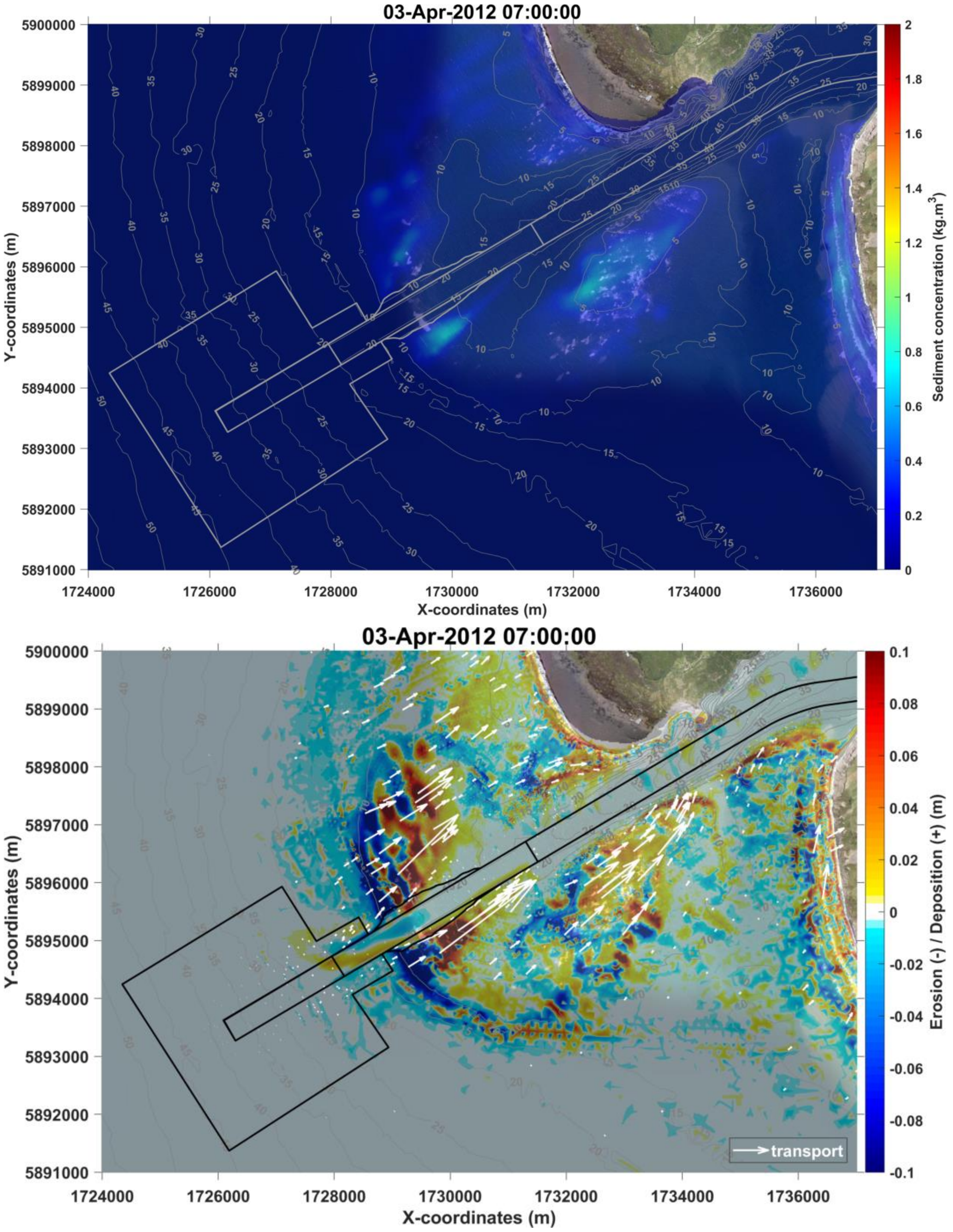

Figure 4-12 Map results of sediment concentration (top panel) and erosion/deposition (bottom panel). For bottom panel: negative values (blue) represent erosion and positive values (red) represent deposition of sediment. White arrows show sediment transport direction. Results at high tide for Control 7 (H_s = 5 m, T_p = 15 s and Dir = 230 deg). Isobaths illustrate the bathymetry of channel scenario with the position of the concept channel shown as solid lines in the figures.

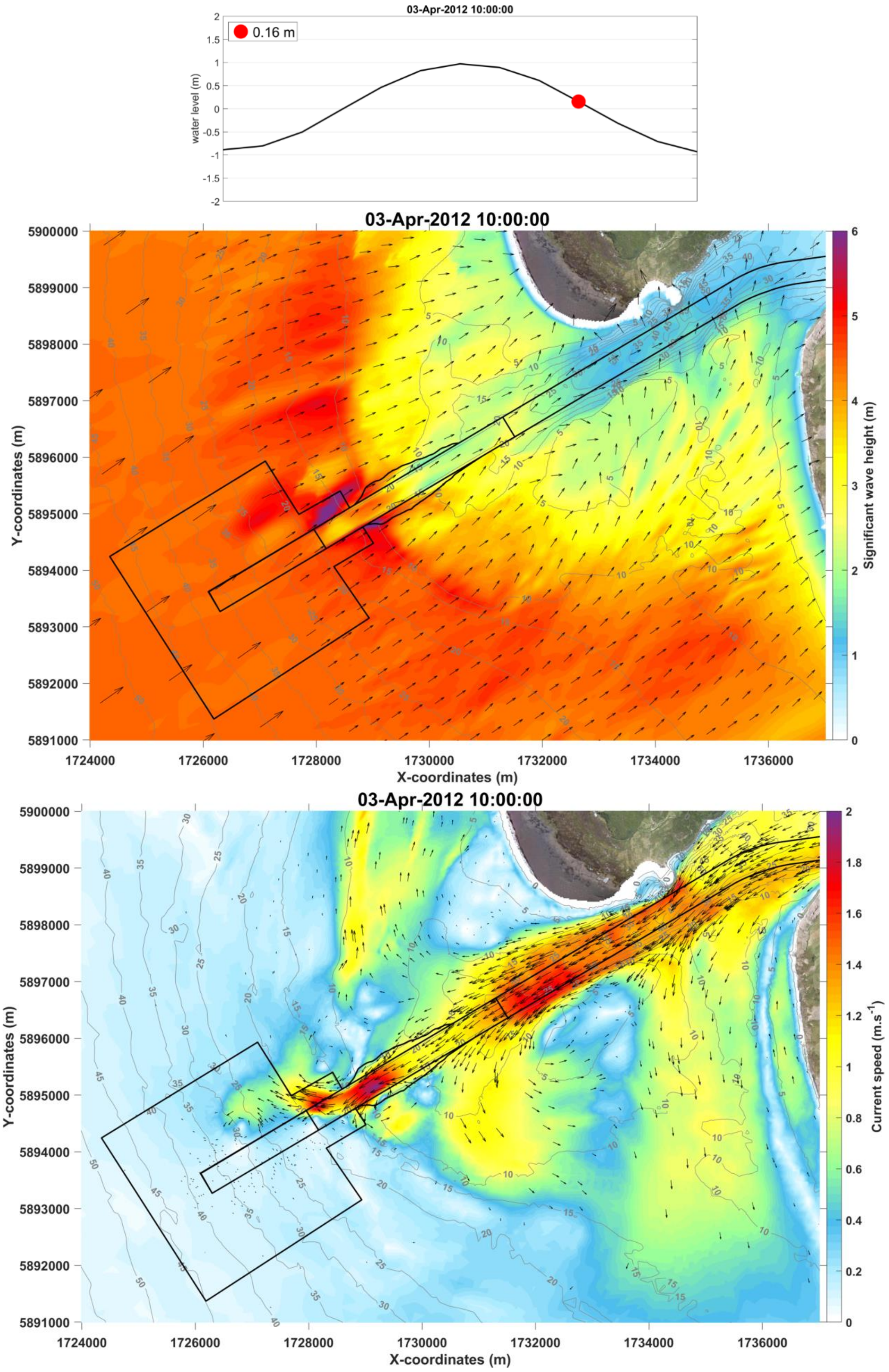

Figure 4-13 Map results of wave (middle panel) and current (bottom panel) magnitude (colormap) and direction (vectors) during the ebb tide for Control 7 (H_s = 5 m, T_p = 15 s and Dir = 230 deg). Isobaths illustrate the bathymetry of channel scenario with the position of the concept channel shown as solid lines in the figures.

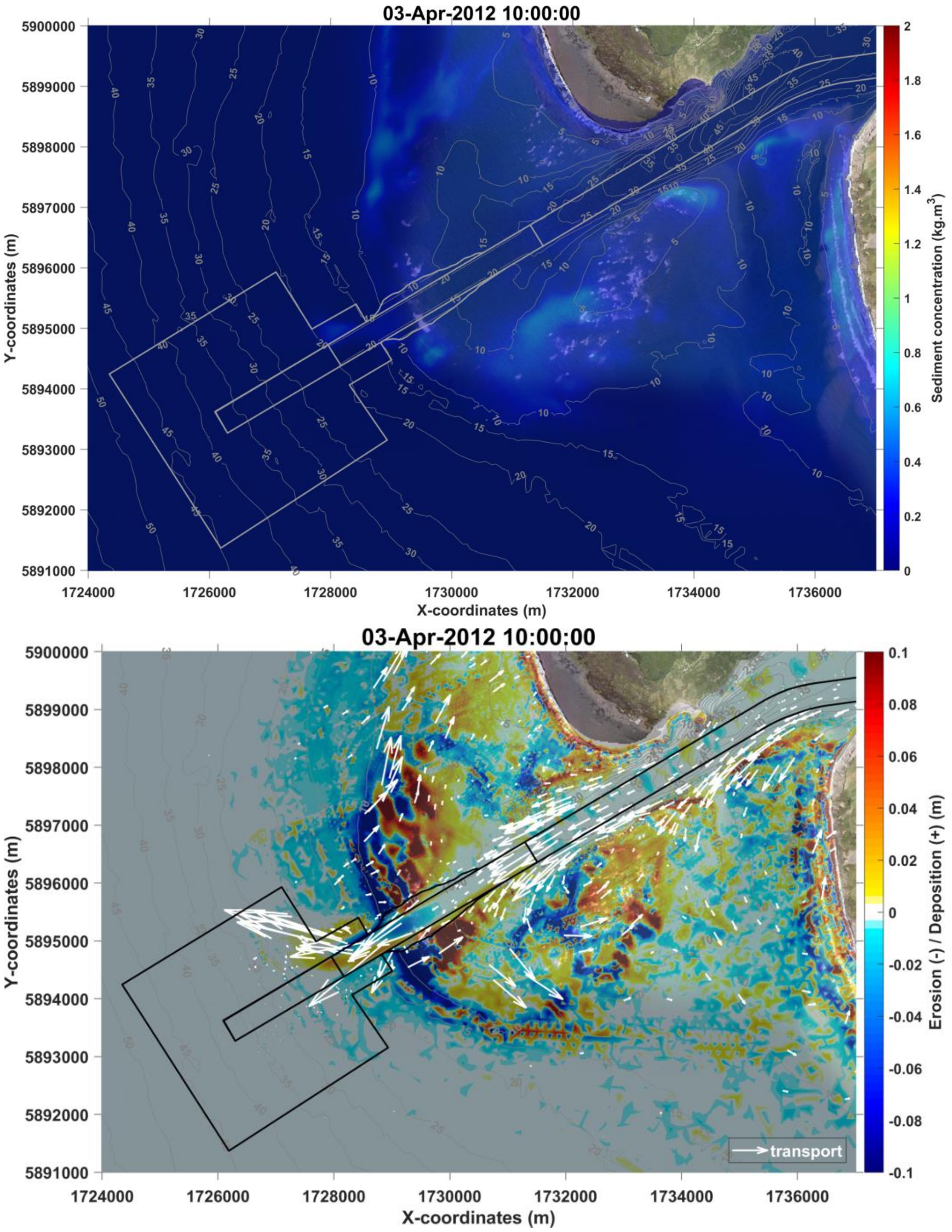

Figure 4-14 Map results of sediment concentration (top panel) and erosion/deposition (bottom panel). For bottom panel: negative values (blue) represent erosion and positive values (red) represent deposition of sediment. White arrows show sediment transport direction. Results during the ebb tide for Control 7 (H_s = 5 m, T_p = 15 s and Dir = 230 deg). Isobaths illustrate the bathymetry of channel scenario with the position of the concept channel shown as solid lines in the figures.

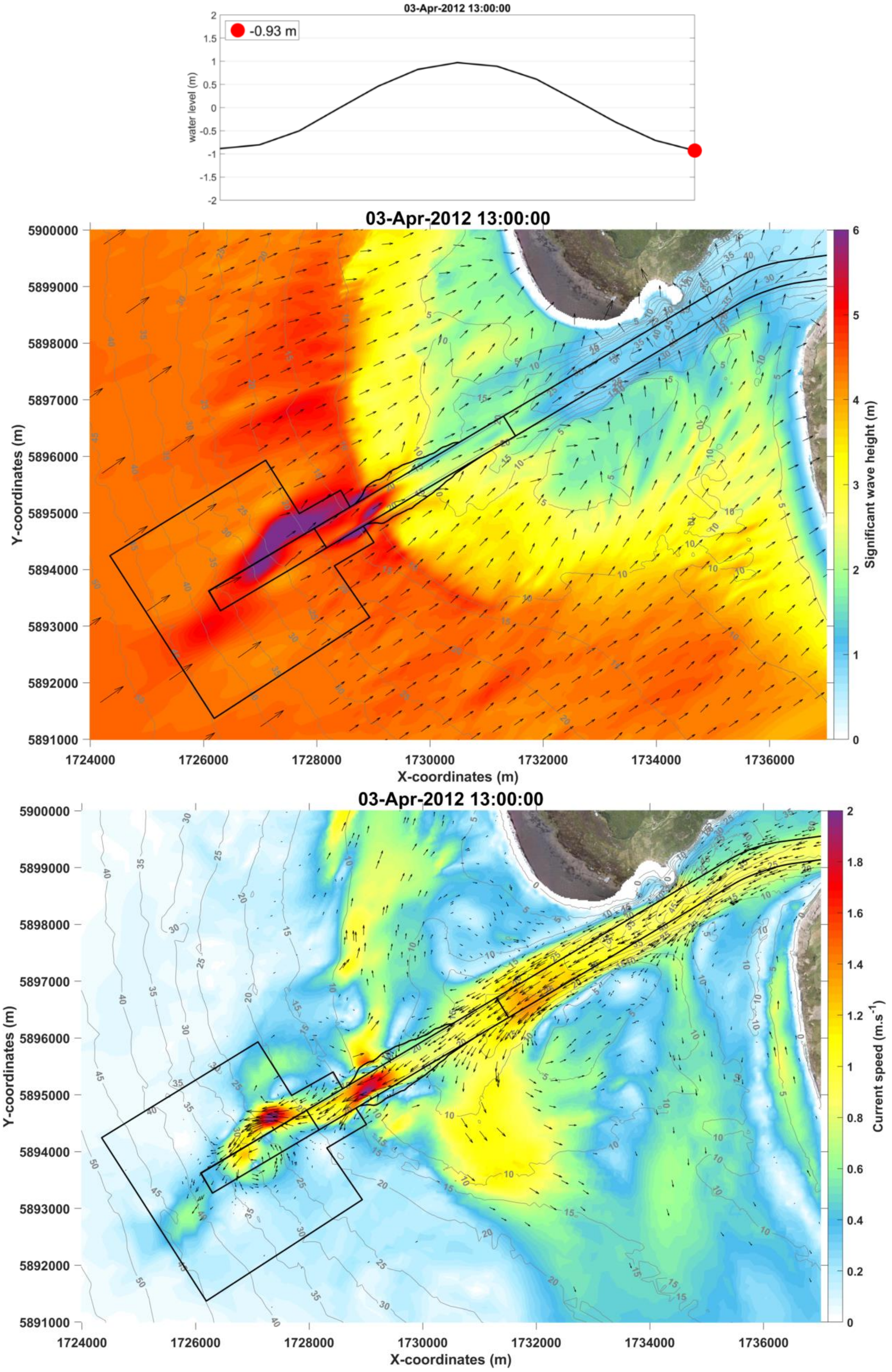

Figure 4-15 Map results of wave (middle panel) and current (bottom panel) magnitude (colormap) and direction (vectors) at low tide for Control 7 (H_s = 5 m, T_p = 15 s and Dir = 230 deg). Isobaths illustrate the bathymetry of channel scenario with the position of the concept channel shown as solid lines in the figures.

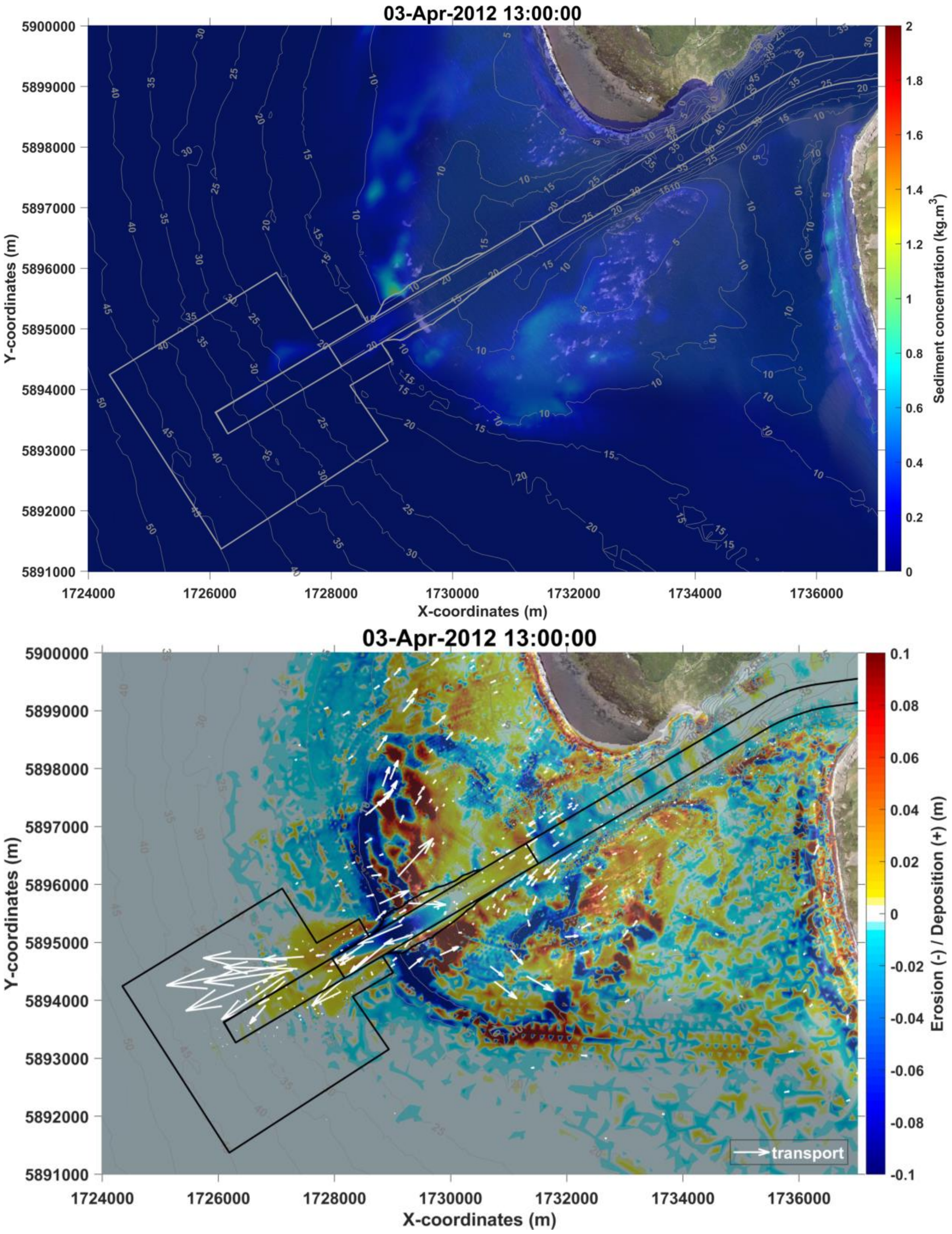

Figure 4-16 Map results of sediment concentration (top panel) and erosion/deposition (bottom panel). For bottom panel: negative values (blue) represent erosion and positive values (red) represent deposition of sediment. White arrows show sediment transport direction. Results at low tide for Control 7 (H_s = 5 m, T_p = 15 s and Dir = 230 deg). Isobaths illustrate the bathymetry of channel scenario with the position of the concept channel shown as solid lines in the figures.

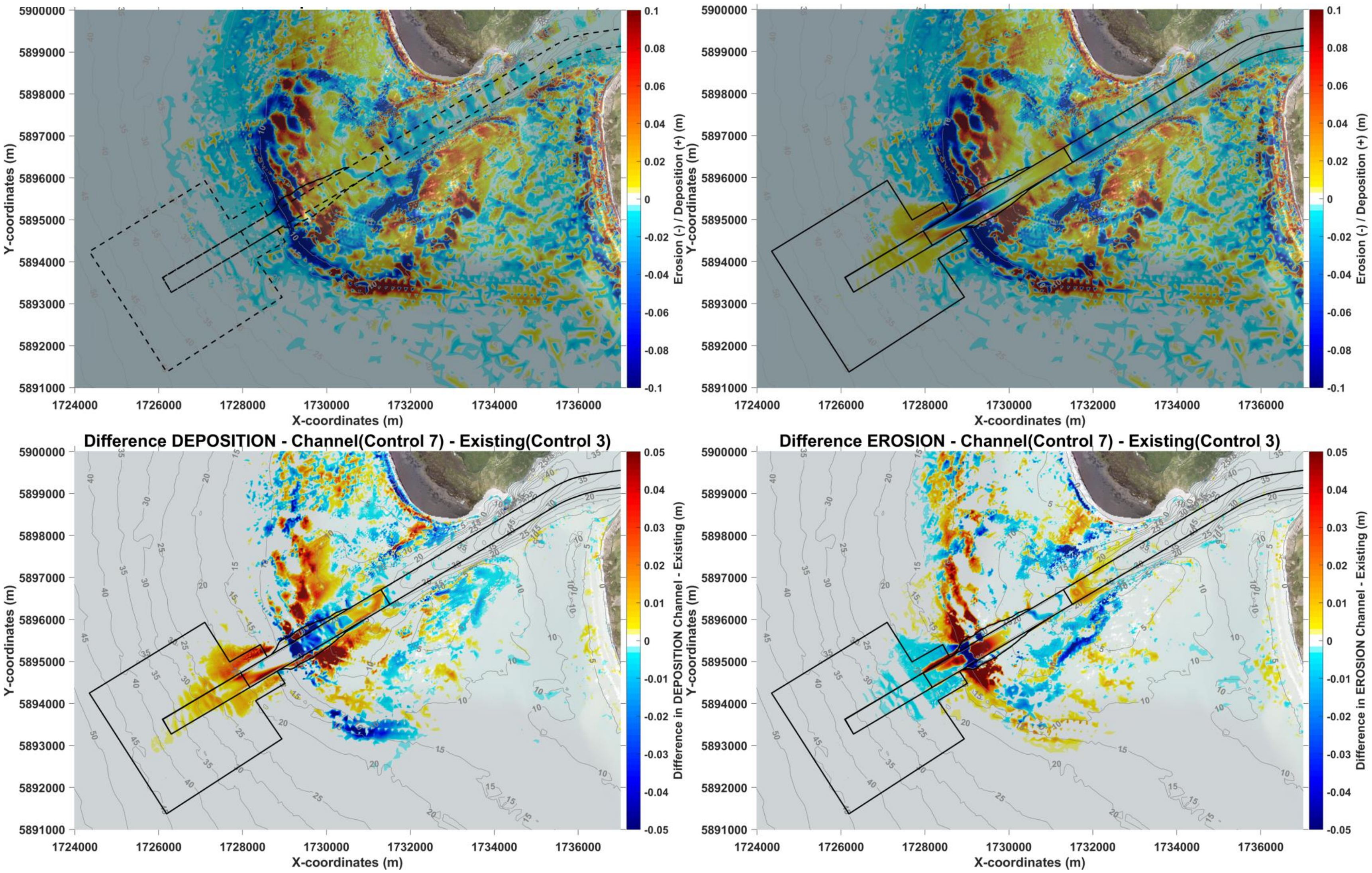

Difference DEPOSITION - Channel(Control 7) - Existing(Control 3)

Difference EROSION - Channel(Control 7) - Existing(Control 3)

Figure 4-17 Top panels show map results of erosion/deposition for runs using the existing bathymetry (top left – Control 3) and including the conceptual navigation channel (top right – Control 7). Wave conditions for both runs were: H_s = 5 m, T_p = 15 s and Dir = 230 deg. Bottom panels show difference in deposition (bottom left) and difference in erosion (bottom right) between scenario including the concept dredge channel (Control 7) and the existing configuration (Control 3).

4.2 Sediment Infill Processing Areas

Infill volumes were calculated within some areas of interest, facilitating a comparison of the various scenarios simulated. The polygons used to represent those areas of interest are shown in Figure 4-18. They are polygons 3 and 4, located in the South West channel near the bar, and polygons 5 and 6, representing the north and south batter slope areas next to polygon 3.

For the infill volumes, we considered:

- All sediment deposited after the 12-hour run, this assessed deposition occurring above the design dredged depth, this is represented by the red polygon in Figure 4-19. Noting that some deposition took place in areas deeper than the design depth (blue polygon in Figure 4-19) and would not be accounted for dredging at initial stages.
- The net volumes which considers both deposition and erosion rates after the 12-hour run. These net infill rates were mostly erosive or showed a low net positive infill. This volume is the sum of the red, blue and green polygons in Figure 4-19, where the green polygon are negative values as accounts for areas of erosion.

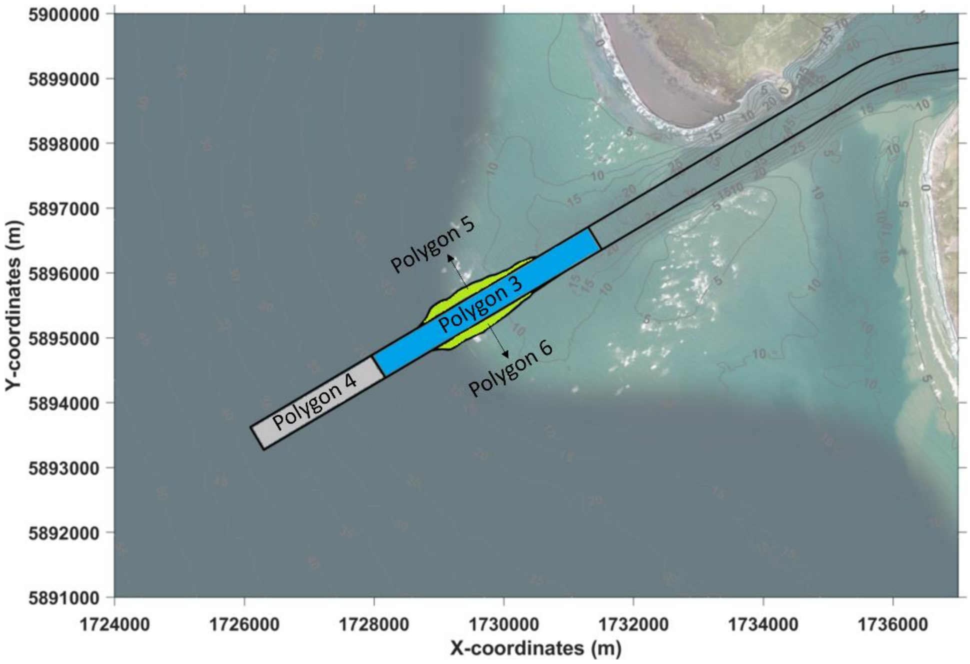

Figure 4-18 Polygons used to calculate infill rates at the bar.

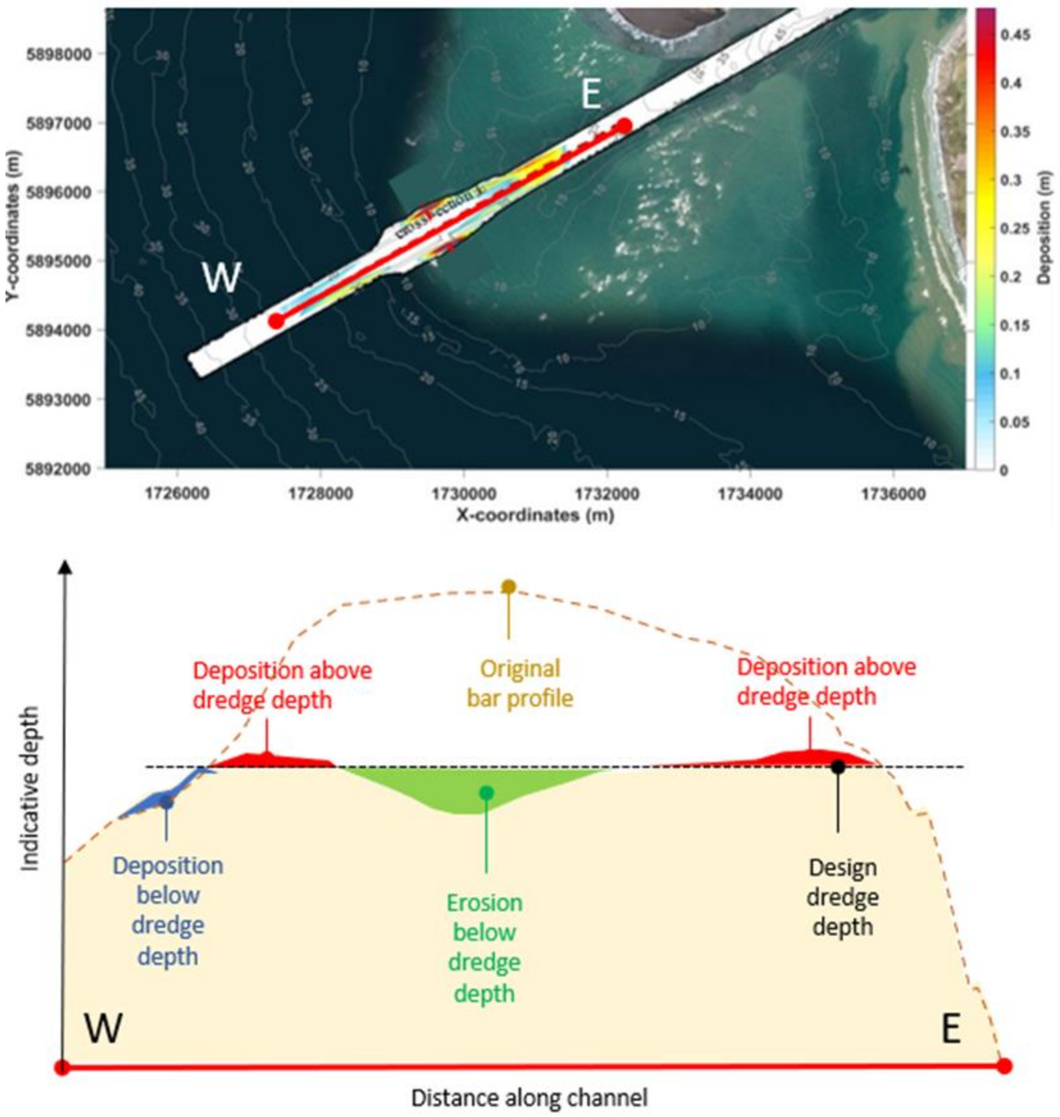

Figure 4-19 Schematic showing definition of areas used to calculate infill volumes.

4.3 Sedimentation

After completing all control scenarios, we calculate the infill volume within the areas described in Section 4.2, facilitating a comparison of the various scenarios simulated. This section presents and discusses the infill volumes for the different scenarios. The sediment transport pathways are described in more detail in the next section (Section 4.4).

Within the 'bar' polygons (3+4+5+6), infill volumes varied from approximately 1,200 m^3 for a tide-only simulation to around 60,400 m^3 for a 5 m wave scenario, including for three sediment classes (Table 4-2).

Considering the area of each polygon, it is important to note that the seabed is not uniformly flat (e.g., Figure 4-19). Consequently, there are regions within the polygons characterized by peaks and troughs. Peak areas typically undergo erosion, while troughs tend to accumulate sediment (e.g. Figure 4-20). When considering both erosion and deposition, the net infill rates were mostly erosive or showed a low net positive infill. The net erosion suggests that within the polygon, there are more peak areas that are eroding than troughs areas that are infilling.

Infill above design depth are presented only for scenarios which included the concept navigation channel (Figure 4-21).

Table 4-2: Infill volumes for the 'bar' (polygons 3+4+5+6) after 12h (m^3). Infill above design depth are presented only for scenarios which included the concept navigation channel.

Scenario	Infill bar–- deposition after 12h (m^3)	Infill bar–- NET after 12h (m^3)	Infill bar–- deposition above design depth (m^3)
Control 1	1718	233	n/a
Control 1 (3 sed)	2729	659	n/a
Control 2	1,222	907	944
Control 2 (3 sed)	2,672	2,335	2,155
Control 3	33,583	-1,618	n/a
Control 3 (3 sed)	44,610	-21,920	n/a
3a	36,326	637	n/a
Control 4	43,134	-3,132	n/a
4a	51,106	-1,396	n/a
Control 5	28,418	-452	n/a
5a	27,499	-1,132	n/a
Control 6	26,190	-658	n/a
Control 7	30,591	-7,589	23,979
Control 7 (3 sed)	60,398	-21,368	47,414
Control 8	45,404	-10,261	31,384
Control 9	32,370	710	28,269
Control 10	23,380	-14,976	18,883
Control 11	23,808	-35,703	21,857
Control 12	39,101	-1,783	34,844
Control 13	44,313	-8,865	n/a
Control 14	22,604	-1,172	n/a
Control 15	15,784	-7,155	11,784
Control 16	7283	-522	n/a
Control 17	4482	-86	n/a

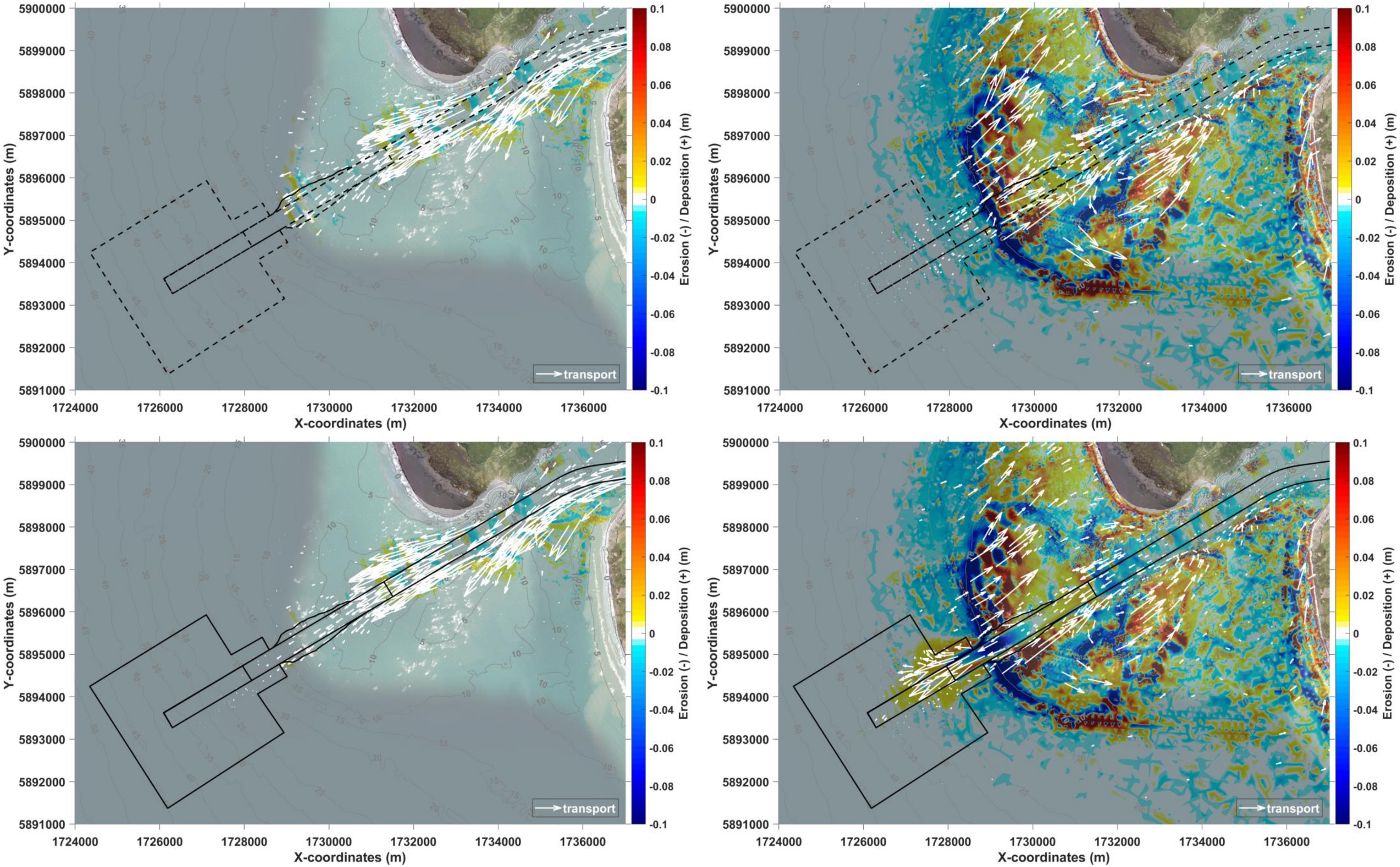

Figure 4-20 Examples of maps of erosion (negative, blue) and deposition (positive, red) results for scenario using the existing (top) and channel (bottom) bathymetries. Arrows show the transport direction. Top left: Control 1 (tide only, no waves), Bottom left: Control 2 (tide only, no waves), Top right: Control 3 (H_s = 5 m, T_p = 15 s and Dir = 230 deg), and Bottom right: Control 7 (H_s = 5 m, T_p = 15 s and Dir = 230 deg).

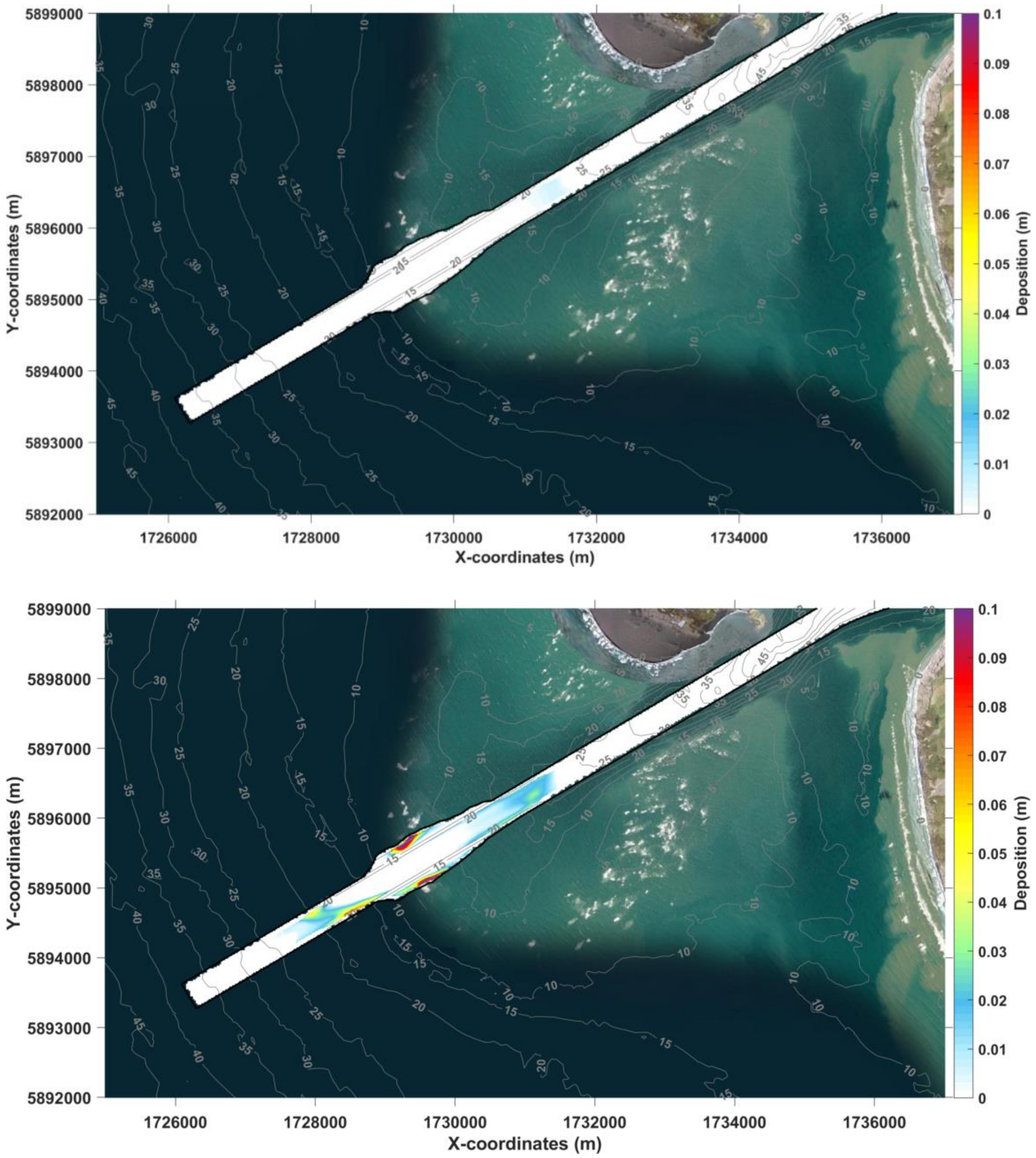

Figure 4-21 Examples of maps of deposition above design depth, for Control 2 (left, tide only, no waves) and Control 7 (right, H_s = 5 m, T_p = 15 s and Dir = 230 deg).

Wind vs no wind scenarios

In scenarios including wind (control 3a, 4a, and 5a), the infill volume at the bar generally exhibited higher values compared to scenarios without wind (control 3, 4, and 5) – 2,700 to 8,000 m^3 higher, except during neap tides (5a) when overall deposition was reduced. Noting that, in terms of net rates, scenarios with wind showed positive rates for Control 3 and lower erosive net rate for Control 4, but the opposite trend was observed for Control 5. This variation could be due to weaker tides, resulting in less sediment that was eroded in shallower areas, being transported into the channel and bar polygons

SW vs NW wave scenarios

In our control runs, we examined the impact of wave direction from the northwest (NW) on sediment erosion and deposition patterns (Figure 4-22). The scenario using the 2023 existing bathymetry (control 6, H_s 5 m, T_p 13 s, and dir = 260 deg) showed less deposition and overall net rates showing reduced erosion compared to Control 3. With the concept navigation channel (Control 10), results showed that net rates tended to be more erosive compared to the scenario without the channel (Control 6) and the deepened bathymetry for southwest waves (Control 7). The infill volume above the design depth for NW waves was lower than that for the SW wave scenario.

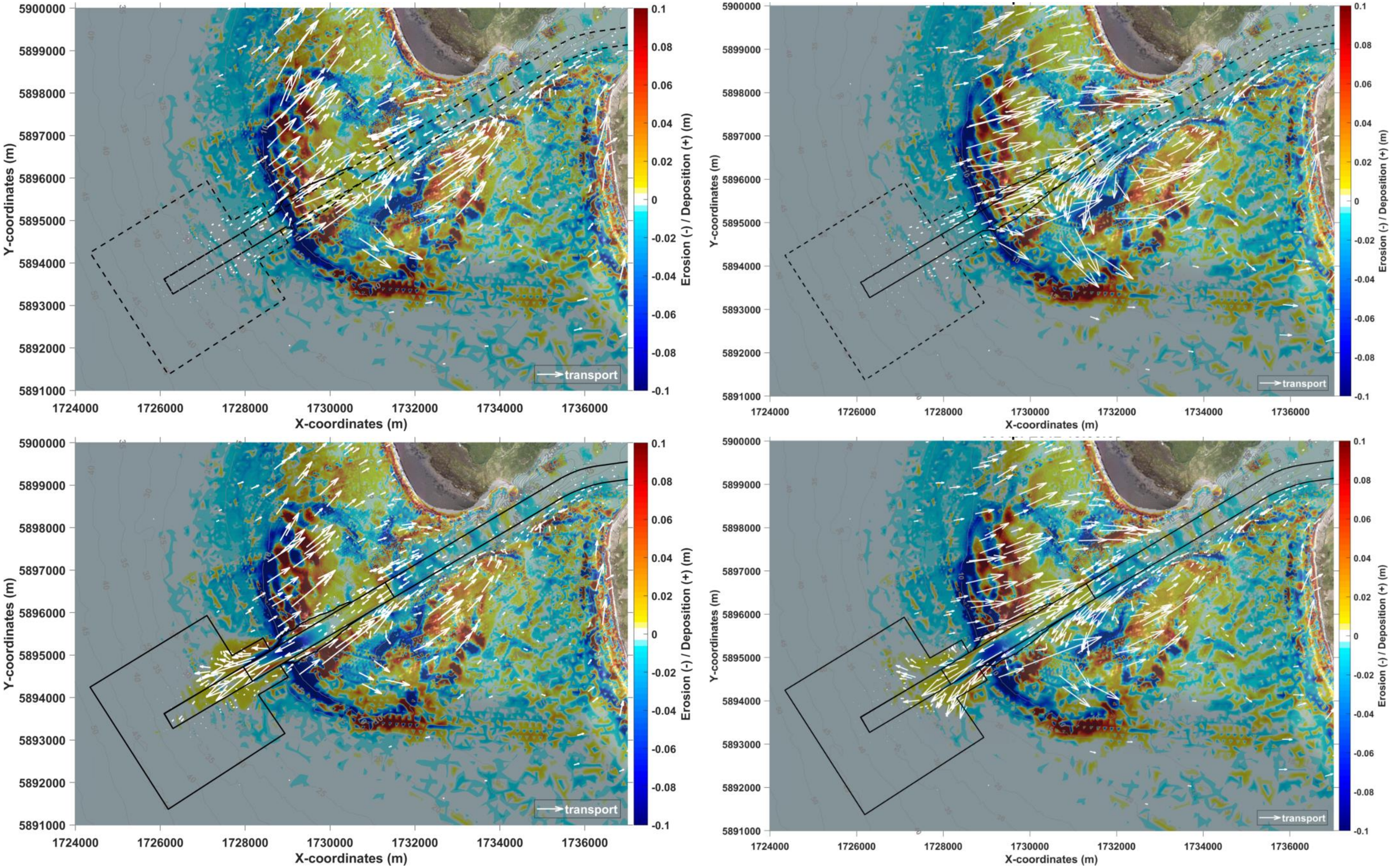

Figure 4-22 Maps of erosion (negative, blue) and deposition (positive, red) results for runs forced by southwest waves (left, H_s = 5 m, T_p = 15 s and Dir = 230 deg) and northwest waves (right, H_s = 5 m, T_p = 13 s and Dir = 260 deg). Top row is the 2023 'existing' bathymetry (Control 3, Control 6), and bottom row is the 2023 bathymetry including the concept navigation channel (Control 7, Control 10).

1989 bathymetry scenarios

Running a different bar configuration (Control 13, 1989 ‘existing’, H_s = 5 m, T_p = 15 s and Dir = 230 deg) yielded an infill volume of approximately 44,300 m^3 compared to approximately 33,600 m^3 for the 2023 existing bathymetry (Control 3). The net rate was erosion of around 8,800 m^3. The 1989 run including the concept navigation channel (Control 11) showed an infill of approximately 23,800 m^3, with a higher net erosion rate of approximately 35,700 m^3 (Figure 4-23).

The results from these two simulations (Control 13 and Control 3) illustrate the variability in infill rates depending on the bar configuration. Given the dynamic nature of the Manukau bar, it becomes essential to account for ongoing natural changes in the wider bathymetry when considering future scenarios of dredging requirements.

The current modelling approach does not allow to infer medium to long term trends; however, as the bathymetry undergoes natural evolution, including adjustments to the dredging (e.g., equilibrium in batter slopes and angles of repose), changes may result in periods characterized by differing levels of maintenance dredging, leading to increased and decreased maintenance demands.

The coastal processes report (TWP03) discusses in more details the geomorphology of the bar (Section 7).

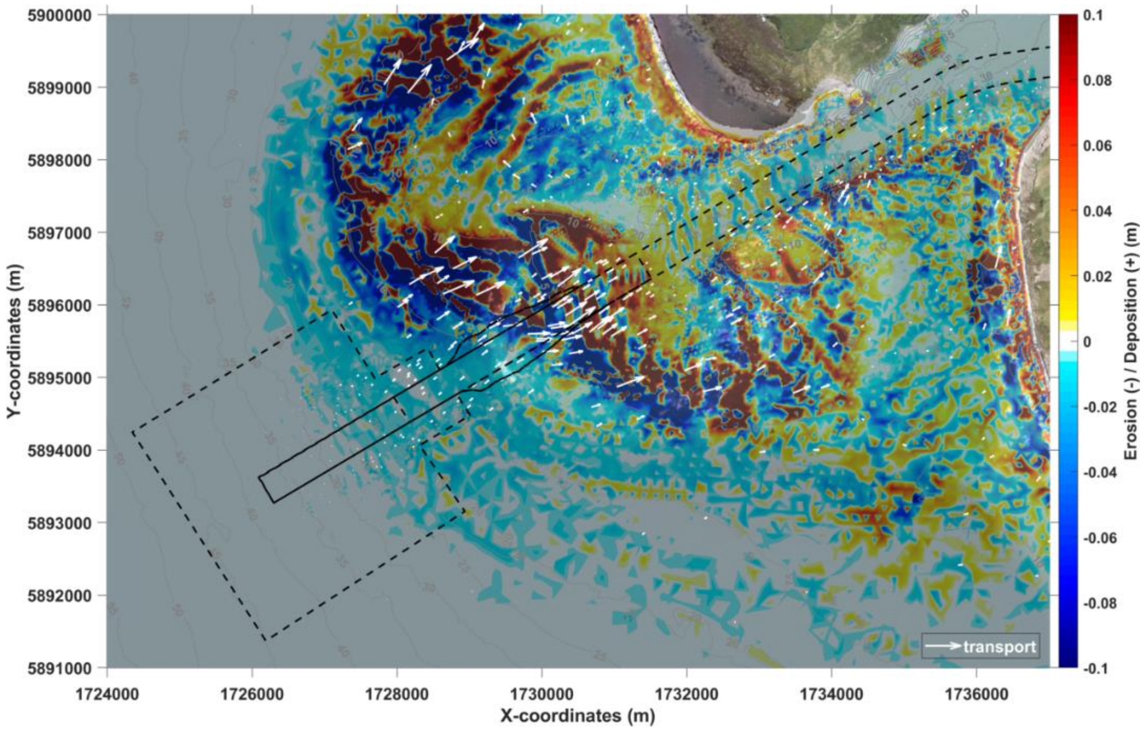

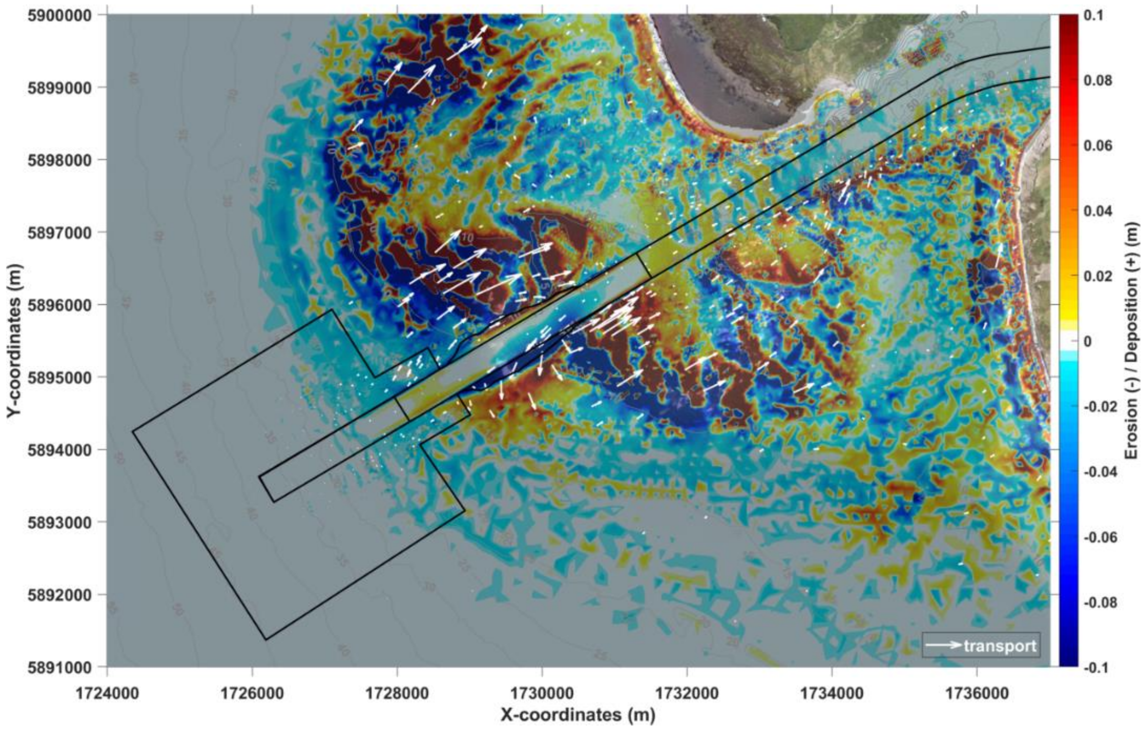

Figure 4-23 Maps of erosion (negative, blue) and deposition (positive, red) results for runs using the 1989 bar configuration (H_s = 5 m, T_p = 15 s and Dir = 230 deg). Left panel is the 1989 'existing' bathymetry (Control 13), and right panel is the 1989 bathymetry including the concept navigation channel (Control 11).

Runs with 3 sediment fractions combined

We ran a few scenarios (Controls 1, 2, 3, and 7) using 3 sediment fractions – 150 µm, 250 µm, and 500 µm – combined in a spatially varying distribution (details on the sediment distribution in Section 3.2.3). Those controls were selected to assess the influence of sediment size on overall sediment transport and sedimentation volume.

Runs which included the 3 sediment fractions presented 1.3 to 2.2 times higher infill volumes than the runs using a single fraction (250 µm). Runs including the channel presented the highest volumes.

It is likely that our estimation of the proportion of fine fractions in the distribution was too high, leading to an overestimation of the infill for those runs. This overestimation occurred because finer fractions are more susceptible to mobilization in the simulations, as evident in the test runs where these fractions were simulated separately, as described below.

Runs using 150 µm and 500 µm sediment fractions

For all the control runs, a single fraction of 250 µm was employed. Additionally, we ran some simulations using a combination of three fractions (150 µm, 250 µm, and 500 µm).

To further investigate the contribution of each of these three fractions to the infill volumes, we carried out separate single-fraction simulations using the finer (150 μm) and coarser (500 μm) fractions.

The results showed, as anticipated, increased sediment transport (Figure 4-24) and higher predicted infill volumes (Table 4-3) for fine sand (150 μm) compared to medium and coarse sand, with the coarser fraction resulting in less infill in comparison to the other fractions.

Table 4-3: Infill volumes for the 'bar' (polygons 3+4+5+6) after 12h (m^3) for runs using a different particle size each (150 μm, 250 μm, and 500 μm). Infill above design depth is presented only for scenarios which included the concept navigation channel. Runs are for H_s = 5 m, T_p = 15 s and Dir = 230 deg.

	Infill bar–- deposition after 12h (m^3)	**Infill bar–- NET after 12h (m^3)**	**Infill bar–- deposition above design depth (m^3)**
Control_03_150	73,069	-41,489	n/a
Control_03_250	33,583	-1,618	n/a
Control_03_500	28,997	1,073	n/a
Control_07_150	109,708	-5,951	89,797
Control_07_250	30,591	-7,588	23,979
Control_07_500	12,310	-8,232	10,187

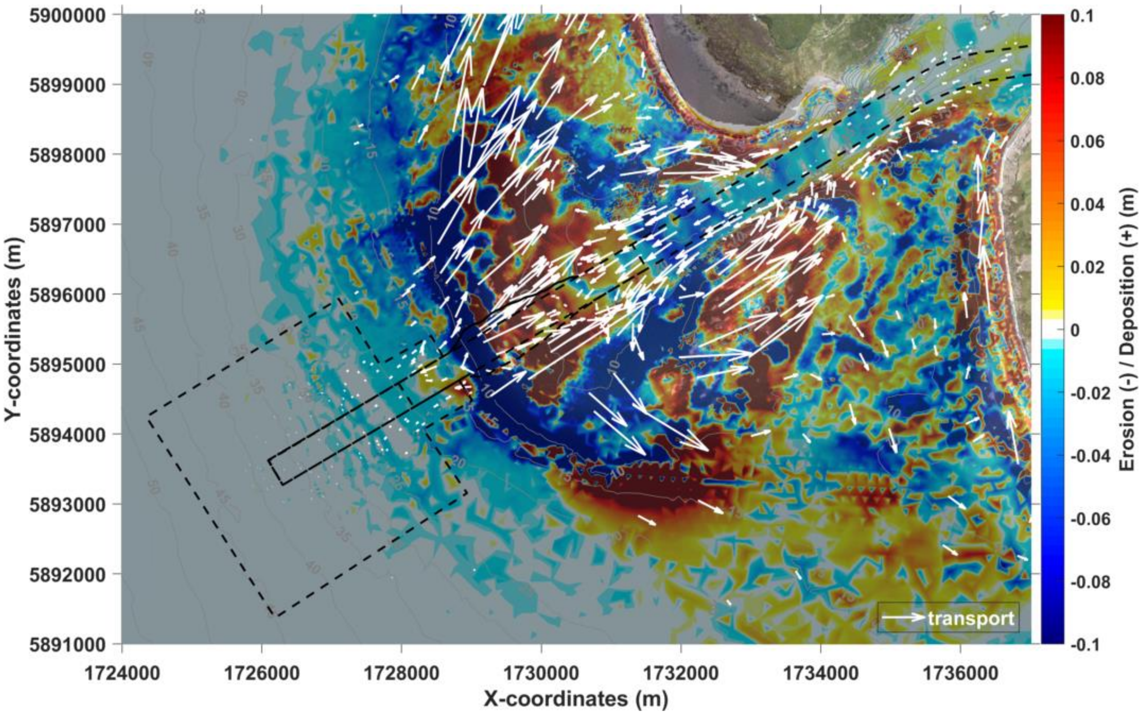

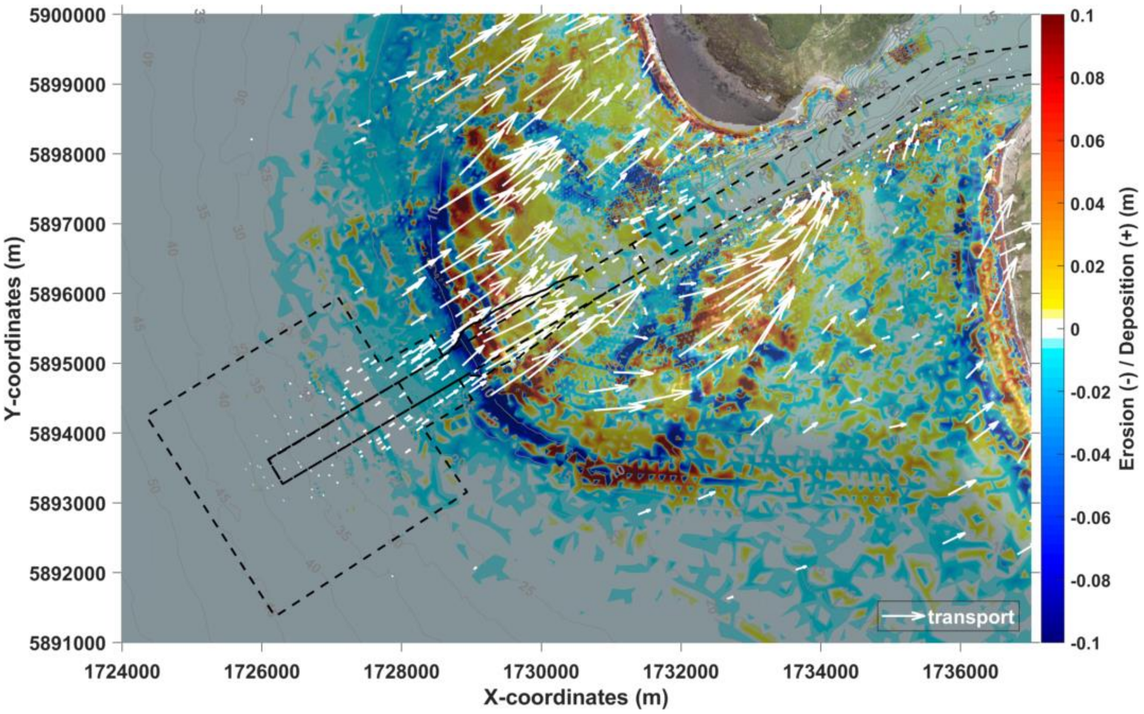

Figure 4-24 Maps of erosion (negative, blue) and deposition (positive, red) results (Control 3, H_s = 5 m, T_p = 15 s and Dir = 230 deg) for runs using 150 µm fraction (top) and 500 µm (bottom).

Bar and open coast transects

In the model verification section (3.2.4), results extracted at three transects show that the transport magnitude at the bar area is greater than that observed along the open coast, south of the channel. Additionally, there is significant infilling of sediment observed for the polygons situated around the bar.

To gain a clearer understanding of transport magnitude and direction around the bar and to compare it with rates along the open coast, we extracted transport rates from model results at various locations (Figure 4-25 for runs with tide only and tide + waves, for the 'existing' and 'channel' bathymetries (Controls 1, 2, 3 and 7). Also, this allowed us to compare rates before and after including the concept navigation channel in the simulations.

Results in Table 4-4 show that transport rates for all transects near the bar area are 2 to 8 times greater than transport rates at the open coast (transects 001 and 006). Transect 000 shows a slight reduction in alongshore transport capacity compared to transect 006.

Transects along the channel (003 and 004) show transport northward and southward, respectively, observed for both existing and with the concept channel scenarios (Control 3 and 7).

Within the channel, transects 014 (landward) and 019 (seaward) show sediment transported onshore into the channel in the existing scenario. However, in the scenario including the concept channel, the transport direction at transect 019 reverses, leading to sediment transport offshore. This change in transport direction is also illustrated in Figure 4-20 (right panels) for the erosion/deposition plots for control 3 ('existing') and 7 ('channel').

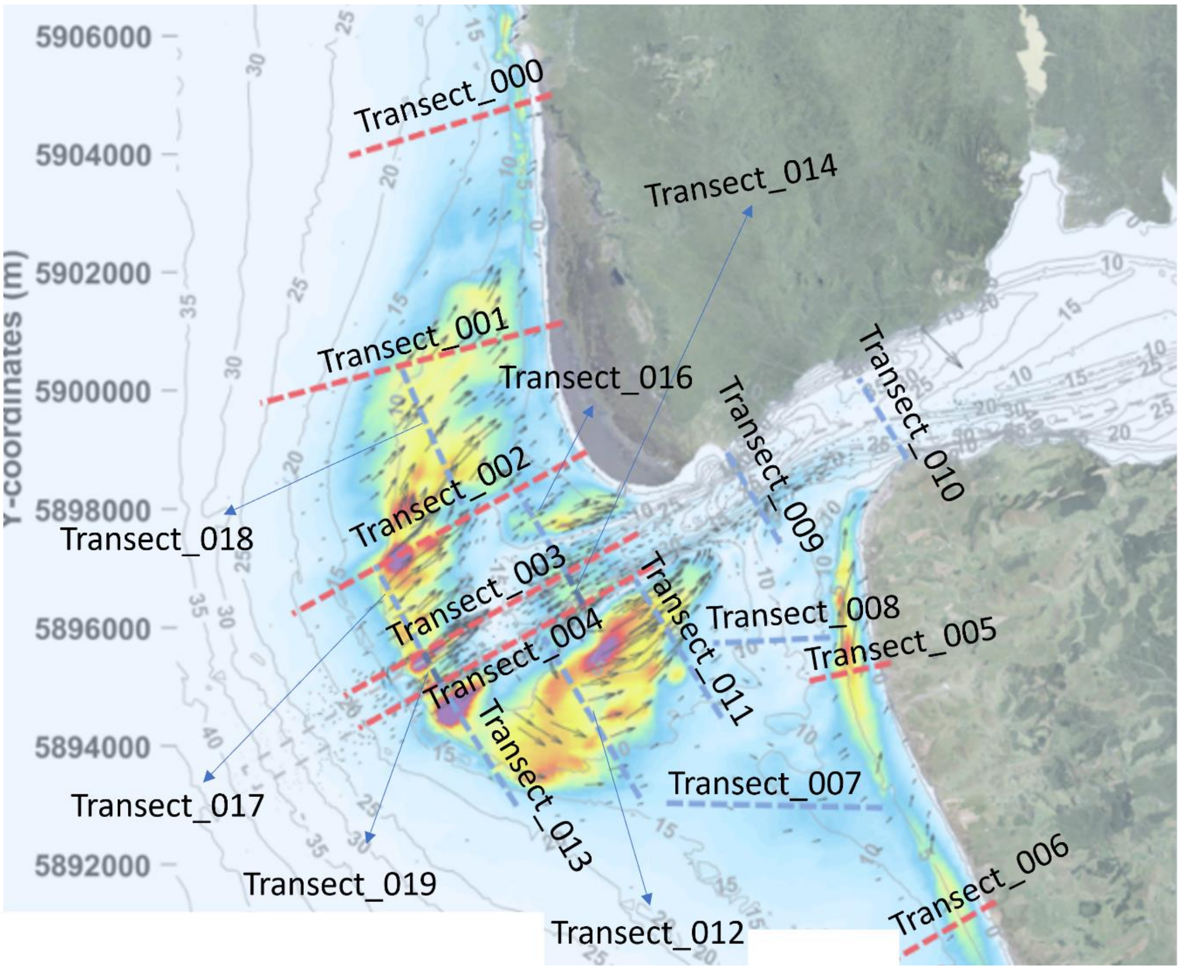

Figure 4-25 Location of transects used to extract model results of sediment transport rates.

Table 4-4 Sediment transport rates at multiple transects for different control scenarios. Control_01 and Control_02 are tide only, no waves. Control_03 and Control_07 are for H_s = 5 m, T_p = 15 s and Dir = 230 deg.

	Control_01	Control_02	Control_03	Control_07
transect 000	0.000	0.000	0.101	0.101
transect 001	0.000	0.000	0.545	0.506
transect 002	0.002	0.001	0.319	0.185
transect 003	0.006	0.006	0.102	0.098
transect 004	-0.015	-0.014	-0.168	-0.161

transect 005	0.000	0.000	0.223	0.233
transect 006	0.000	0.000	0.105	0.104
transect 007	0.000	0.000	-0.197	-0.185
transect 008	0.001	0.001	-0.071	-0.062
transect 009	-0.040	-0.042	-0.067	-0.069
transect 010	-0.014	-0.014	-0.008	-0.008
transect 011	-0.002	-0.001	0.421	0.359
transect 012	-0.003	-0.002	0.233	0.272
transect 013	-0.005	-0.002	0.450	0.798
transect 014	-0.022	-0.030	-0.170	-0.217
transect 016	-0.020	-0.024	-0.061	-0.086
transect 017	-0.002	-0.001	0.313	0.574
transect 018	0.000	0.000	0.375	0.426
transect 019	-0.004	-0.004	0.158	-0.152

Contribution of waves and currents to the sediment transport

Figure 4-26 shows bedload and suspended transport due to currents (top) and to waves (bottom). A comparison between wave-induced and current-induced transport shows that:

- Transport by waves are in general onshore and highest near the seabed.
- Transport by currents occurs mainly as suspended load.
- Most of the transport is observed over the bar crests, however, currents also exhibit increased transport within the channel, likely tide related.
- Currents play an import role in transporting sediment within the channel and towards the offshore terminal lobe.
- Near the coast, south of the harbour entrance, we observe transport onshore and longshore towards the harbour.
- Transport is directed northwards along the downdrift coast.

Figure 4-27 to Figure 4-31 illustrate how the model is representing surf zone processes leading to sediment transport (e.g. alongshore and cross-shore transport due to waves and currents). As mentioned in Section 3.2.3 the wave induced currents is accounted in the current transport. The model uses radiation stress gradients to calculate wave driven currents, and these drive surf zone sediment transport.

Transects 001 and 002 on the bar (Figure 4-27and 28) and transects 006 on the open coast (Figure 4-31) show both normal and tangential transport as waves approach the coast and interact with the seabed on shallower areas (<15m for a wave of approximately 3-3.5 m).

- Suspended transport by currents dominate the total transport along those transect.
- Suspended transport is mainly to the north, however bedload transport due to waves tend to be directed southwards.
- Transport is higher over the bar crests.

Transects 003 and 004 are located along the northern and southern margins of the main ebb channel.

- Transect 003, located on the northern margin of the channel, shows increased suspended transport by currents into the channel and towards the shore (Figure 4-29).
- Along the southern margin (transect 004, Figure 4-30), transport is predominantly towards out of the channel, except for a section in the centre of the transect displaying lower transport rates and where sediment is going in the channel.
- Bedload transport, by waves and currents, is mainly directed towards the shore in transect 004.
- The suspended load shows alternating transport directions (offshore - onshore - offshore) due to the interaction of onshore waves and opposing tidal currents in the region, as depicted in Figure 4-26.

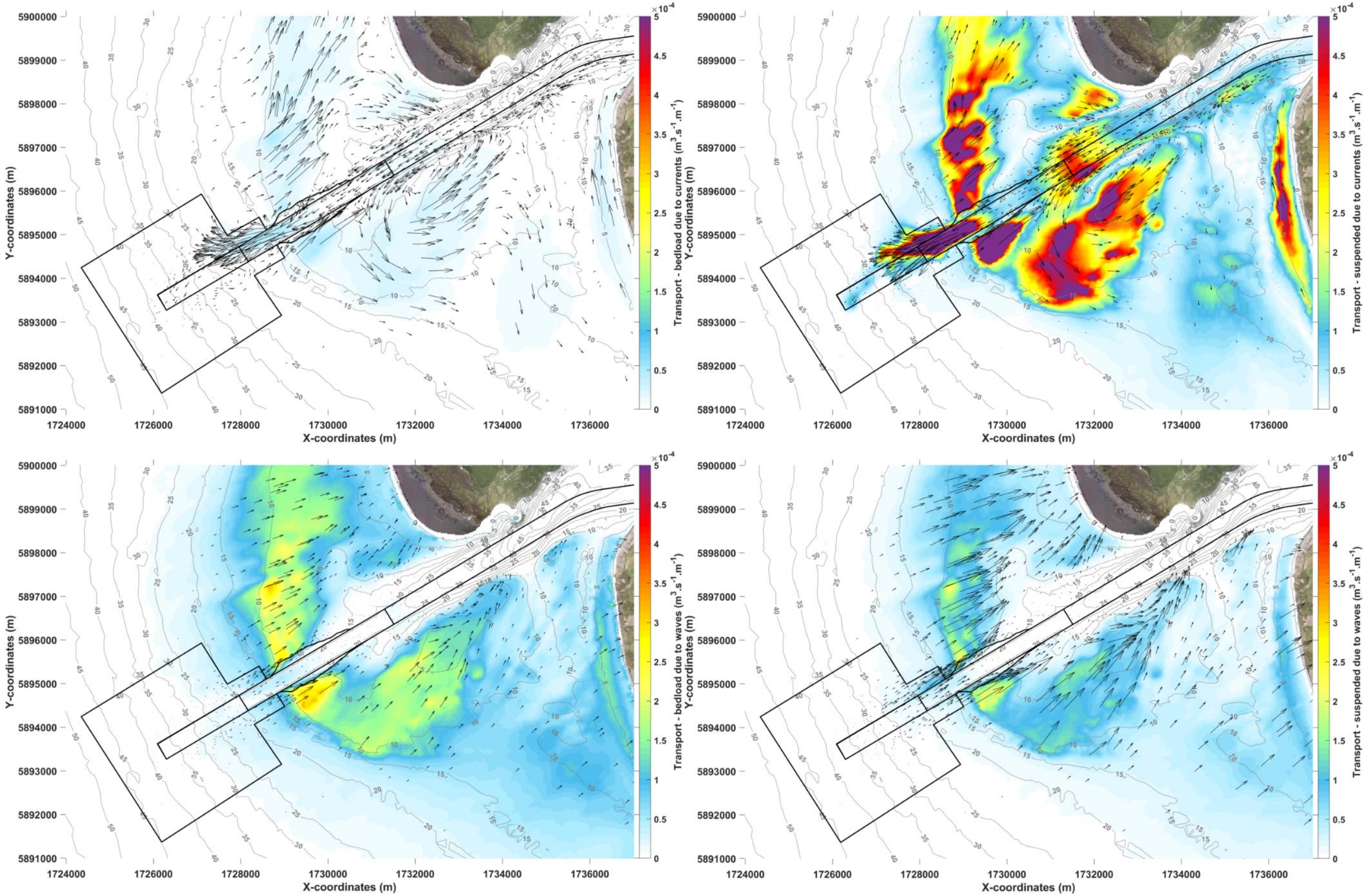

Figure 4-26 Maps of average bedload (left) and suspended (right) sediment transport for runs including the channel (Control 7, H_s = 5 m, T_p = 15 s and Dir = 230 deg). Top row shows transport due to currents and bottom row shows transport due to waves.

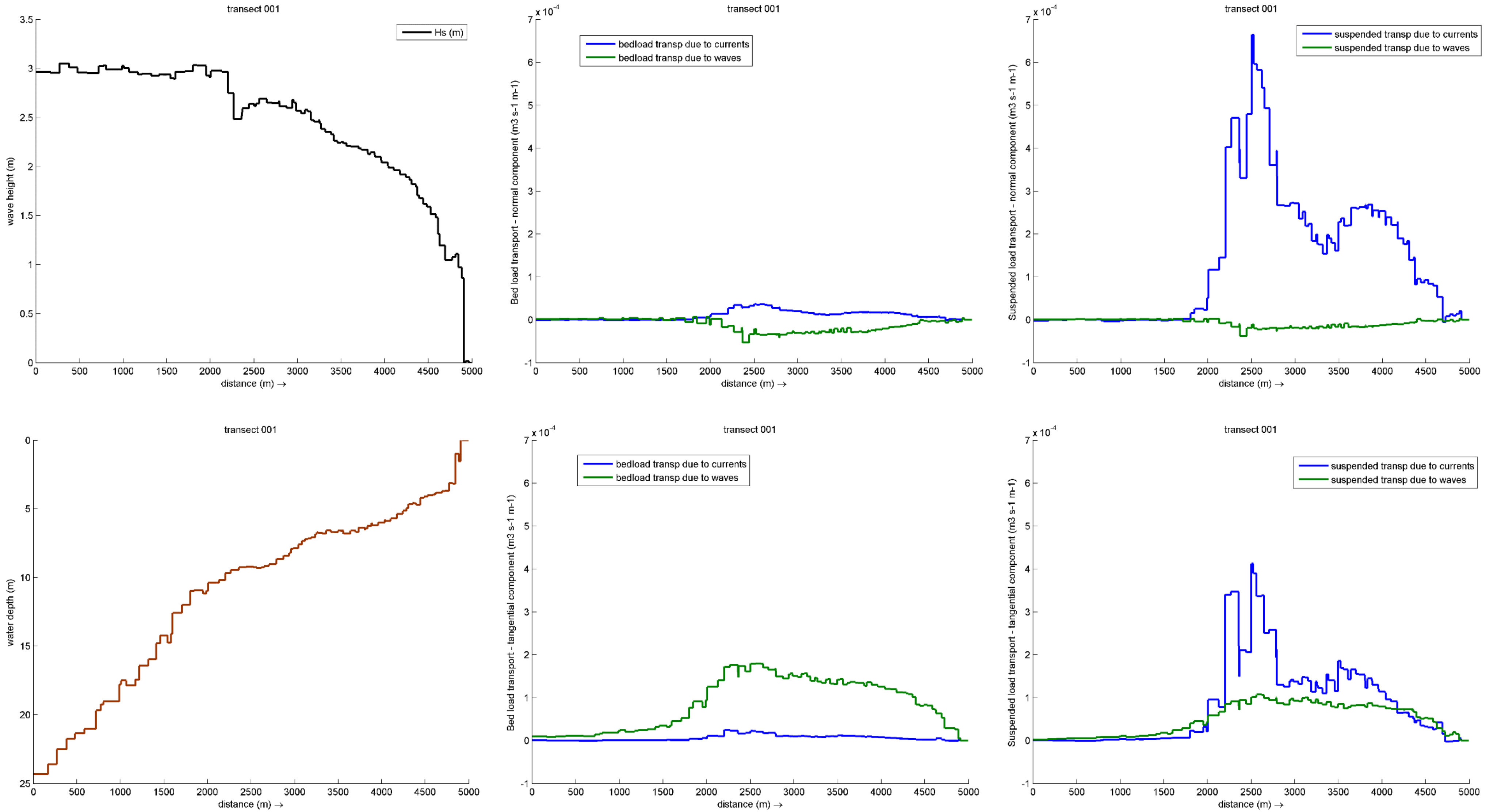

Figure 4-27 Profiles along transect 001 of significant wave height (Hs, top left) and water depth (bottom left), normal component of bedload transport (top middle) and suspended transport (top right) due to currents (blue) and waves (green). Positive values represent transport north and negative values transport south. Bottom row shows the tangential component of bedload transport (bottom middle) and suspended transport (bottom right) due to currents and waves. Positive values represent onshore transport and negative values represent offshore transport. Results are for runs including the channel (Control 7, H_s = 5 m, T_p = 15 s and Dir = 230 deg). Transects locations are presented in Figure 4-25.

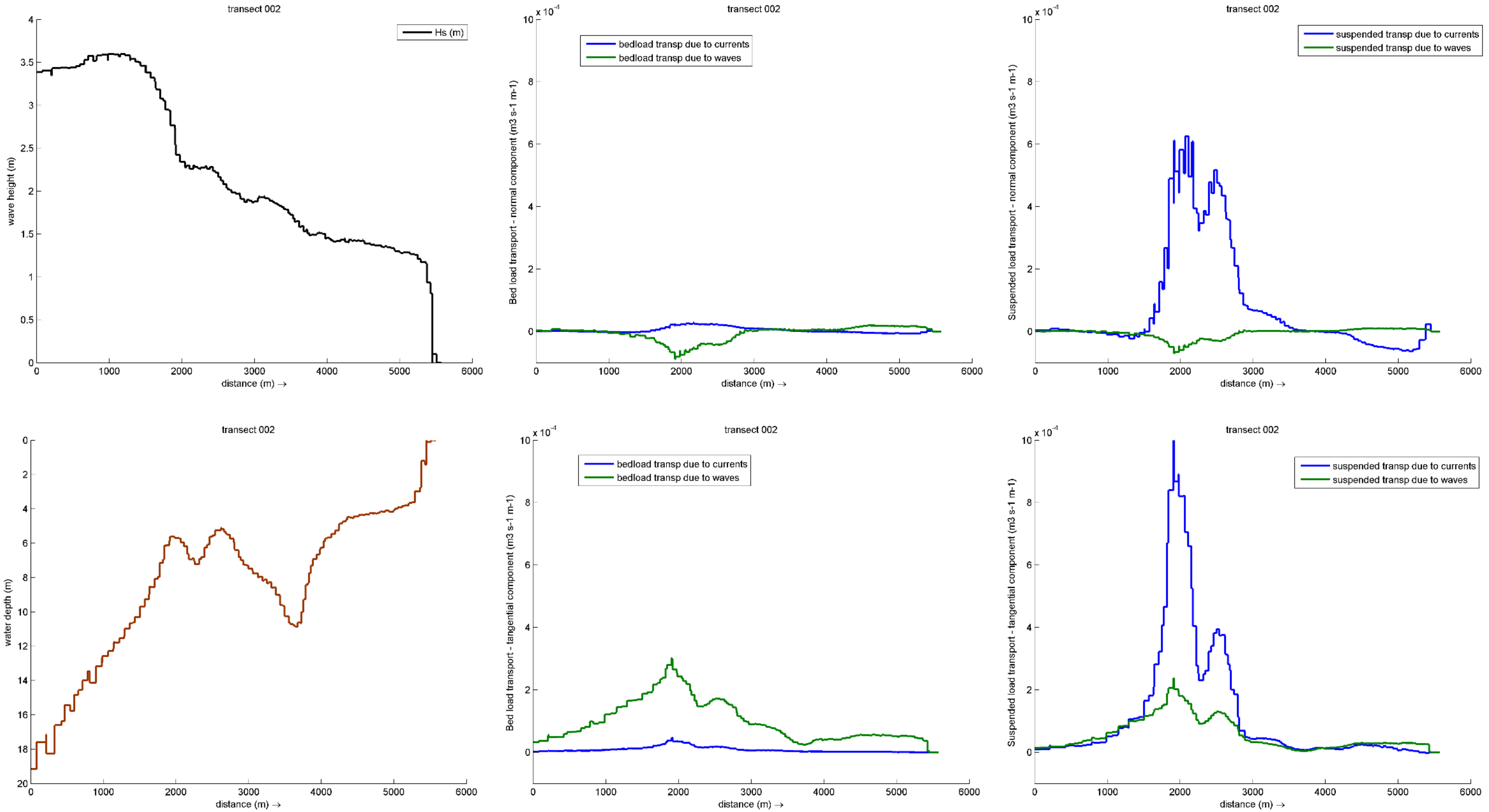

Figure 4-28 Profiles along transect 002 of significant wave height (Hs, top left) and water depth (bottom left), normal component of bedload transport (top middle) and suspended transport (top right) due to currents (blue) and waves (green). Positive values represent transport north and negative values transport south. Bottom row shows the tangential component of bedload transport (bottom middle) and suspended transport (bottom right) due to currents and waves. Positive values represent onshore transport and negative values represent offshore transport. Results are for runs including the channel (Control 7, H_s = 5 m, T_p = 15 s and Dir = 230 deg). Transects locations are presented in Figure 4-25.

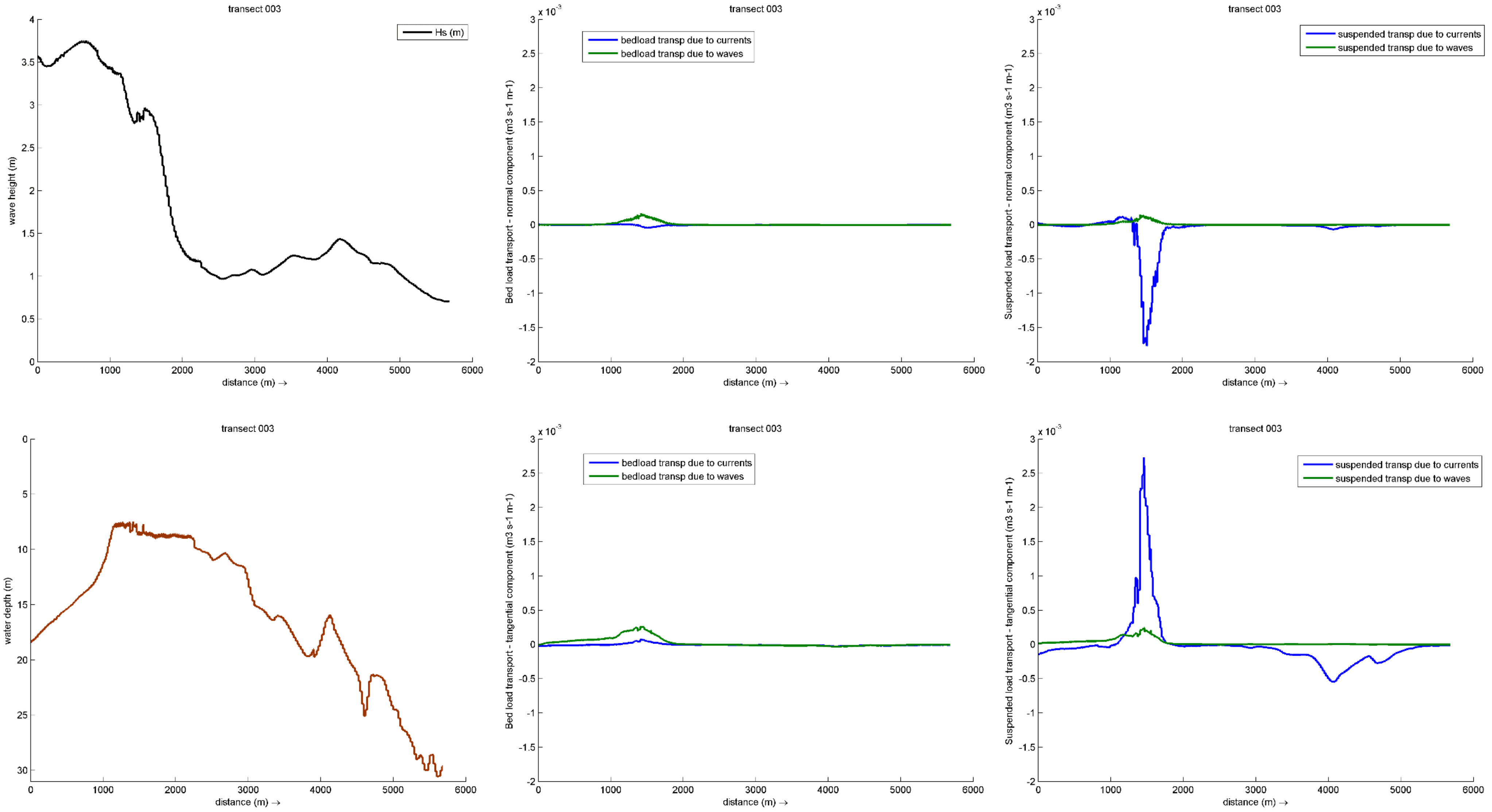

Figure 4-29 Profiles along transect 003 of significant wave height (Hs, top left) and water depth (bottom left), normal component of bedload transport (top middle) and suspended transport (top right) due to currents (blue) and waves (green). Positive values represent transport north and negative values transport south. Bottom row shows the tangential component of bedload transport (bottom middle) and suspended transport (bottom right) due to currents and waves. Positive values represent onshore transport and negative values represent offshore transport. Results are for runs including the channel (Control 7, H_s = 5 m, T_p = 15 s and Dir = 230 deg). Transects locations are presented in Figure 4-25.

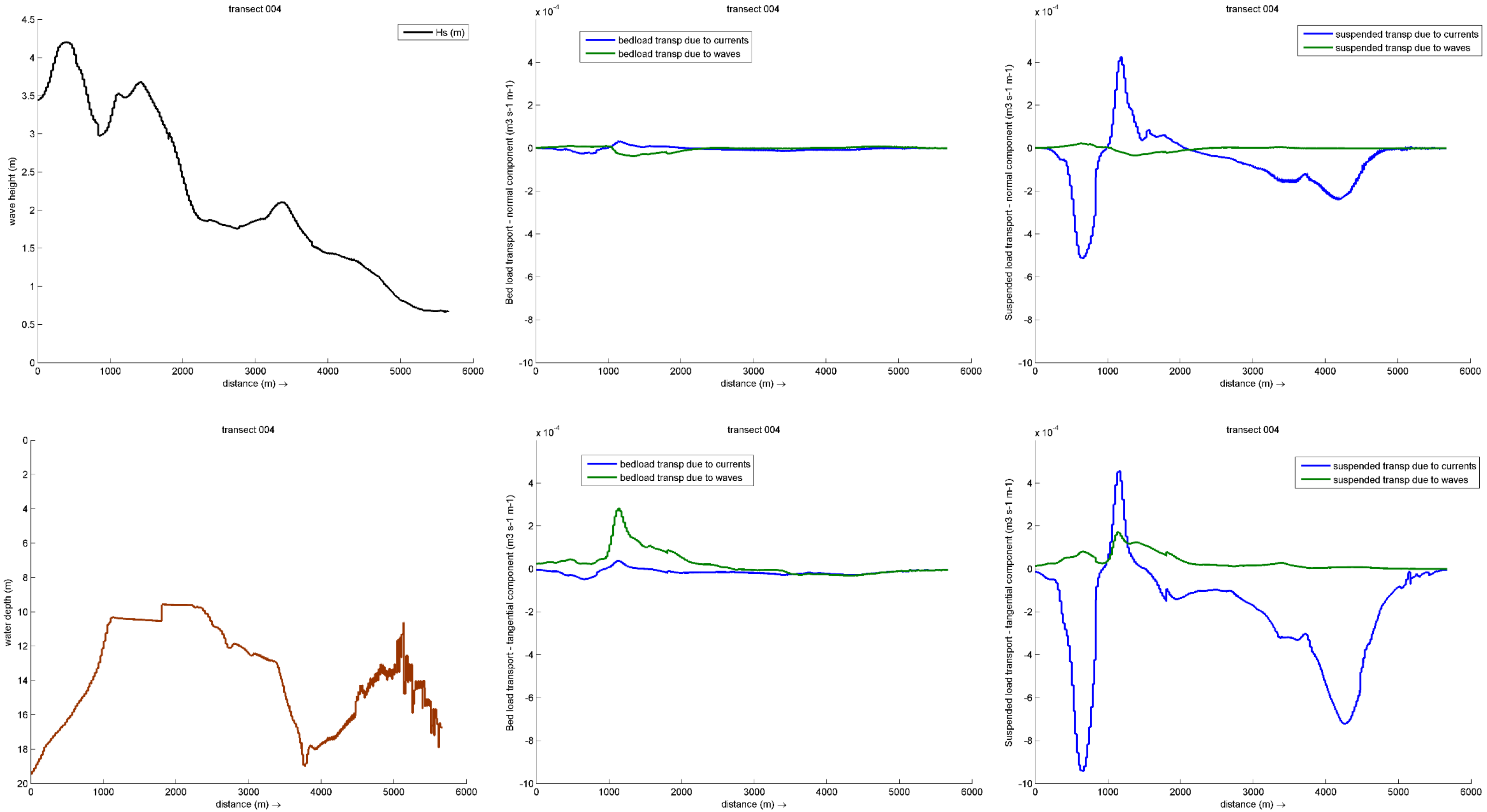

Figure 4-30 Profiles along transect 004 of significant wave height (Hs, top left) and water depth (bottom left), normal component of bedload transport (top middle) and suspended transport (top right) due to currents (blue) and waves (green). Positive values represent transport north and negative values transport south. Bottom row shows the tangential component of bedload transport (bottom middle) and suspended transport (bottom right) due to currents and waves. Positive values represent onshore transport and negative values represent offshore transport. Results are for runs including the channel (Control 7, H_s = 5 m, T_p = 15 s and Dir = 230 deg). Transects locations are presented in Figure 4-25.

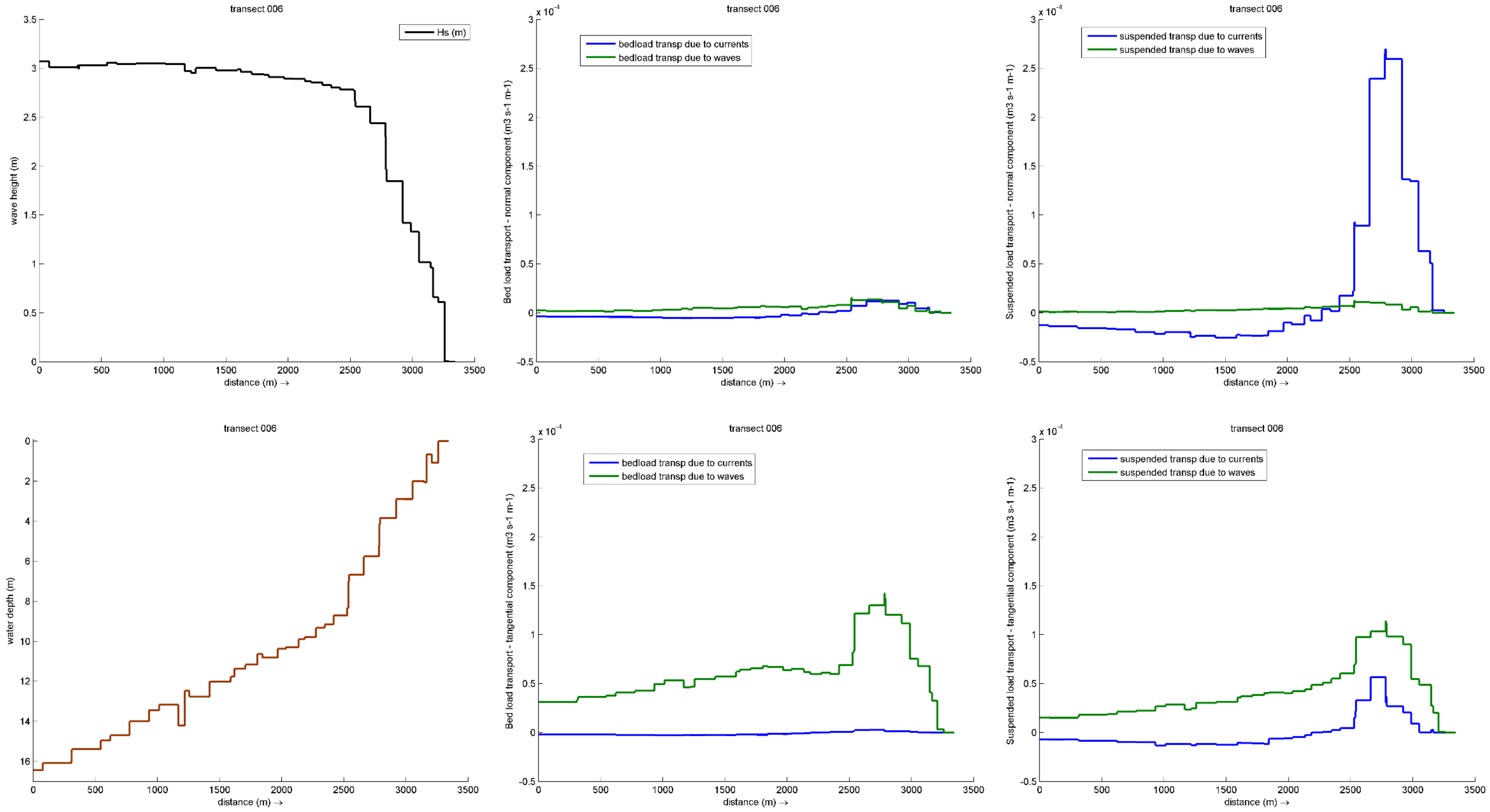

Figure 4-31 Profiles along transect 006 of significant wave height (Hs, top left) and water depth (bottom left), normal component of bedload transport (top middle) and suspended transport (top right) due to currents (blue) and waves (green). Positive values represent transport north and negative values transport south. Bottom row shows the tangential component of bedload transport (bottom middle) and suspended transport (bottom right) due to currents and waves. Positive values represent onshore transport and negative values represent offshore transport. Results are for runs including the channel (Control 7, H_s = 5 m, T_p = 15 s and Dir = 230 deg). Transects locations are presented in Figure 4-25.

Spring tide scenarios

Runs Control 4 and Control 8 provided results for a 12-hour run during spring tide. To evaluate the potential impact of extending the simulation by one hour (making it a 13-hour run) to capture the final stages of the ebbing tide during spring runs, we calculated the infill volume for longer durations.

Our analysis showed that extending the simulation including the channel by an hour resulted in an increase in infill volume of approximately 13% for typical tide runs (Control 7), 22% for spring tides (Control 8), and 8% for neap tides (Control 9). Net volumes, accounting for both deposition and erosion, indicated an increase in erosion during the additional hour for typical and spring tides (Table 4-5).

Note that our sedimentation assessment, presented in Section 5, focused on results from runs using "typical" tide, therefore it did not consider the results of spring tide.

Table 4-5 Infill volumes for the 'bar' (polygons 3+4+5+6) after 12h and 13h (m^3). All scenarios were forced with waves: H_s = 5 m, T_p = 15 s and Dir = 230 deg. Control 3, 4 and 5 are scenarios including existing bathymetry and control 7, 8 and 9 included the proposed channel.

	EXISTING			**CHANNEL**		
	Typical	**Spring**	**Neap**	**Typical**	**Spring**	**Neap**
	Control_3	**Control_4**	**Control_5**	**Control_7**	**Control_8**	**Control_9**
ACCRETION						
12h	33,583	43,134	28,418	30,591	45,404	32,370
13h	36,067	45,978	31,411	34,479	55,508	35,012
Difference	2,484	2,844	2,993	3,888	10,104	2,642
%				**13%**	**22%**	**8%**
NET						
12h	-1,618	-3,132	-452	-7,589	-10,261	710
13h	-1,911	-1,995	-265	-8,494	-12,116	1,521
Difference	-293	1,137	187	-905	-1,855	811

Effects of sea level rise on the current scenarios

According to Khojasteh et al (2021), in a scenario of sea level rise (SLR), the propagation of the tidal waves from the mouth to the upstream tidal limit of an estuary may be amplified, dampened, reflected, and/or deformed depending on the shape of an estuary. The authors reviewed several studies on how SLR may affect estuarine processes and created conceptual models of the effects of SLR on estuarine hydrodynamics.

Overall, in terms of tidal hydrodynamics, the potential effects of an increase in sea level at Manukau may be: upstream migration of the tides, increase inundation of the intertidal area, increased tidal attenuation due to the activation of floodplain areas, and decreased drainage during the ebb tide cycle due to the elevated low tide at the ocean boundary.

In terms of sediment dynamics and net transport, SLR can potentially alter the tidal asymmetry, i.e., flood or ebb dominance, affecting the formation of flood and ebb tidal deltas and how much sediment is transported landward and seaward (Khojasteh et al, 2021). These effects also depend on the local hydrodynamics and sediment characteristics.

4.4 Conceptual Model for Sediment Pathways

Based on the results of sediment transport, we created a conceptual model for sediment pathways using control scenarios representative of distinct sediment dynamics. In the conceptual model, bold blue arrows provide a conceptual representation of the main transport patterns.

Focusing on scenarios characterized by tide-only conditions and no waves for existing and design channel (i.e., Control 1 and Control 2), we observe that most sediment transport is directed offshore in the main ebb channel (Figure 4-32).

When waves are included (i.e. Control 3), the transport map shows a higher potential for onshore transport at the terminal lobe, influenced by wave processes on the bar. Conversely, within the channel, tidal currents contribute to sediment transported offshore. This pattern is consistent across various Control runs that were forced by southwest waves. With the inclusion of the dredged channel (Control 7), the flow is not blocked by the mouth bar redirecting the transport of sediments offshore to deeper areas (Figure 4-33).

In contrast to the scenarios with southwest waves, the simulations forced by northwest waves showed downdrift transport more oriented towards the channel rather than northward. At the bar, northwest waves induced transport more towards the southeast direction rather than directly onshore as observed in Control 3 (Figure 4-34). Note that waves coming from the northwest are not as frequent as shown in wave roses in the metocean report. Wave rose presented in Figure 5-4 of the Metocean Report (TWP03b) shows that, at site o1 and based on the wave hindcast, the main wave direction is from the southwest, with low occurrence of waves from the northwest.

Sediment transported along the updrift coast from the south follows a longshore transport path directed into the harbour. Additionally, some of the sediment tends to be transported along the western shoals, moving towards the downdrift coast.

These findings provide insights into the complex interaction of wave conditions, bathymetry, and tidal forces shaping and moving shoals on ebb-tidal deltas.

The study of Ridderinkhof et al. (2016) shows that shoals grow and migrate due to an imbalance between the local bathymetry and wave conditions. The study conducted by Ridderinkhof et al. (2016) offers a comprehensive overview of sediment transport and shoal migration mechanisms, suggesting similarities to the modelled patterns at Manukau. The dissipation of wave energy over shallow features generates radiation stress gradients, driving residual currents toward the coast. These currents, together with wave stirring in shallower water, result in the convergence of sediment transport on top and landward of the shoal. Ebb-tidal deltas lack a closed boundary immediately beyond the coastline, leading to landward residual currents induced by waves and these have a significant role in the net sediment transport.

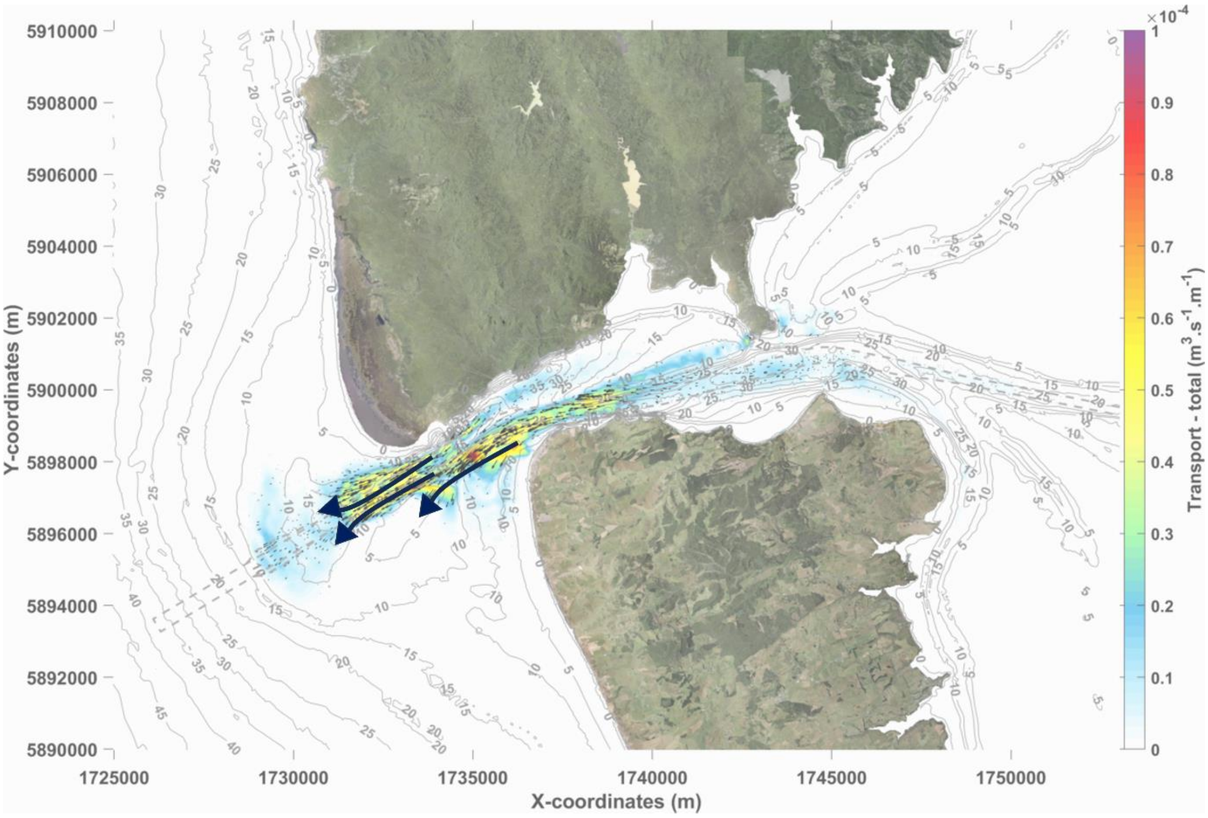

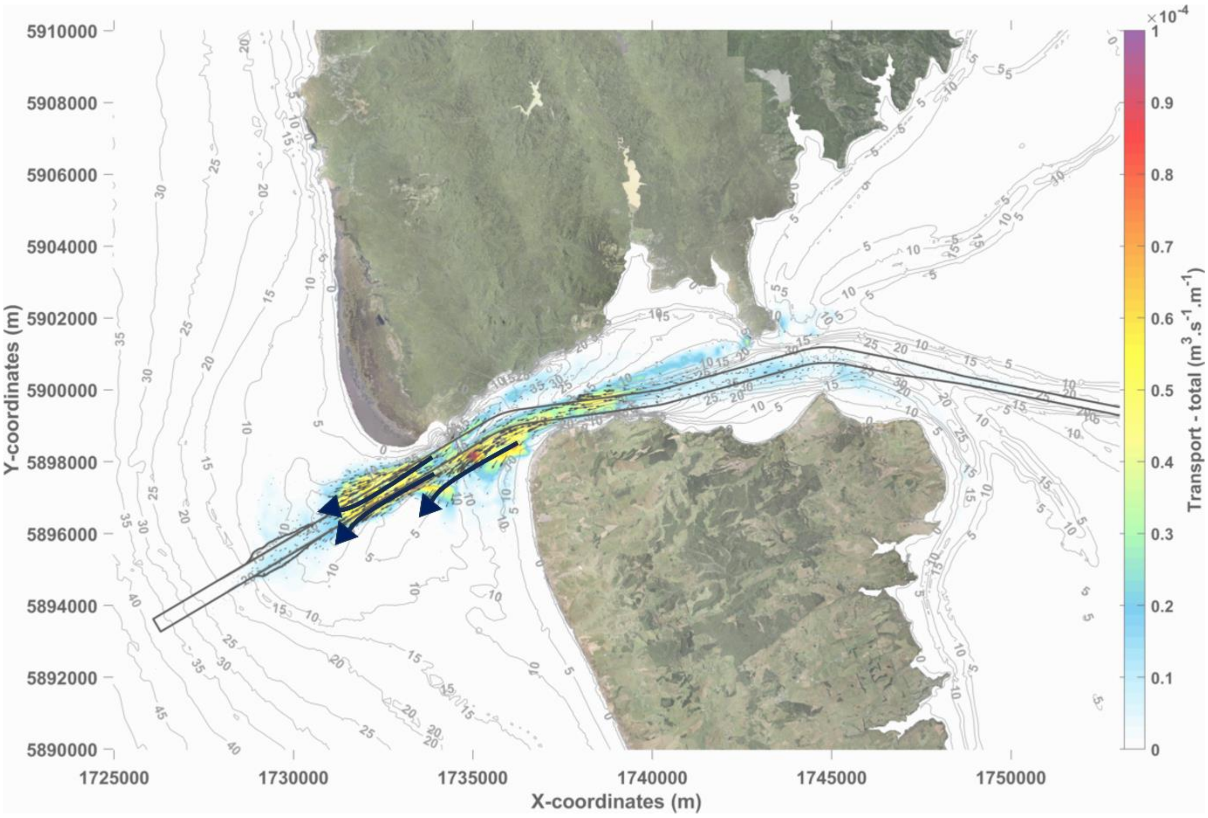

Figure 4-32 Sediment transport magnitude (colormap) and direction (thin black arrows) for runs with tide only, no waves. Control 1, existing bathymetry (top) and Control 2, bathymetry including the concept navigation channel (bottom). Bold blue arrows represent the main transport pattern.

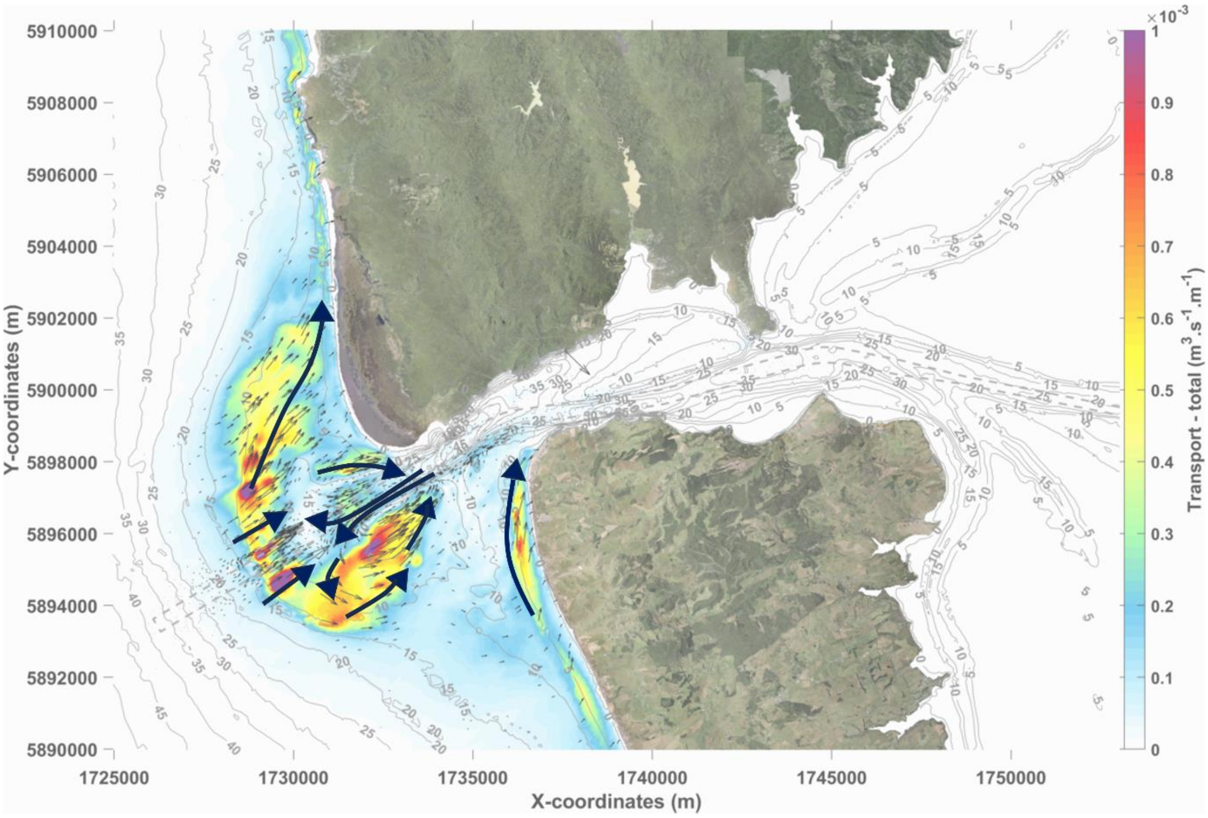

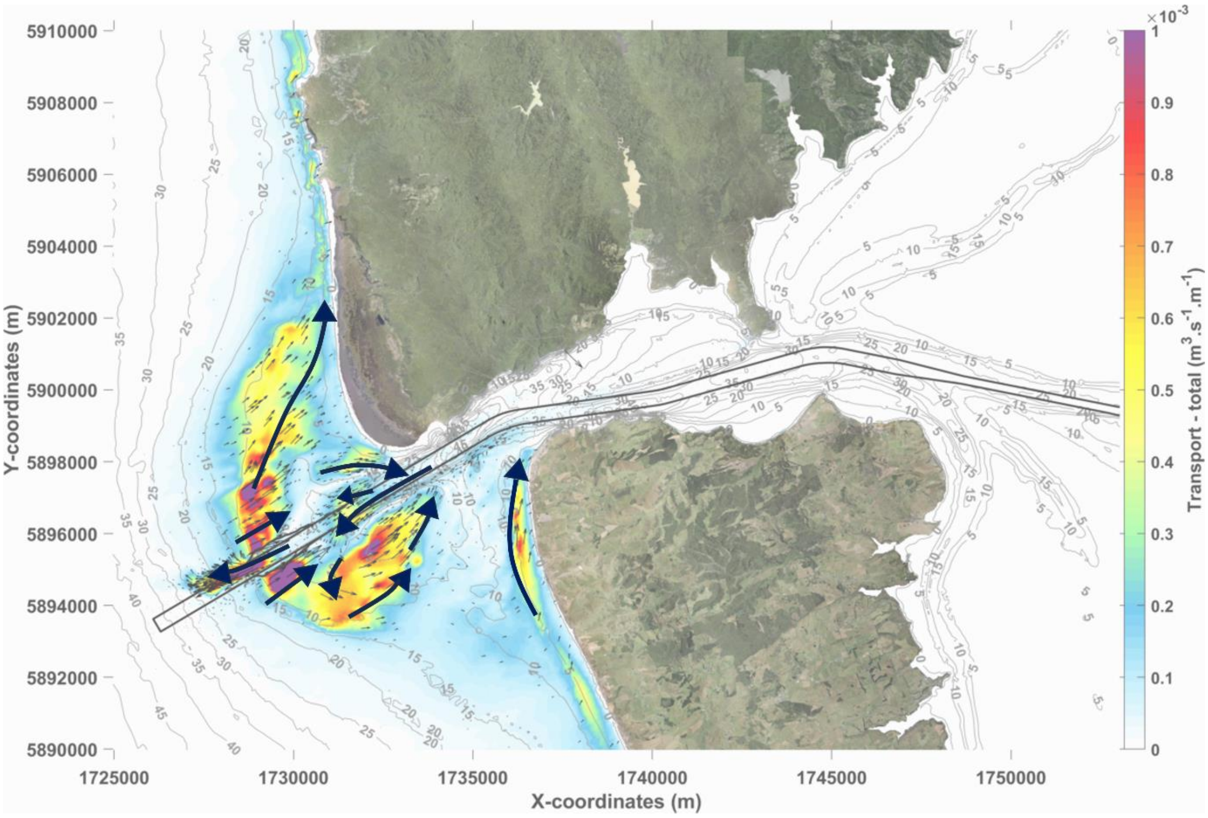

Figure 4-33 Sediment transport magnitude (colormap) and direction (thin black arrows) for runs including waves (H_s = 5 m, T_p = 15 s and Dir = 230 deg). Control 3, existing bathymetry (top) and Control 7, bathymetry including the concept navigation channel (bottom). Bold blue arrows represent the main transport pattern.

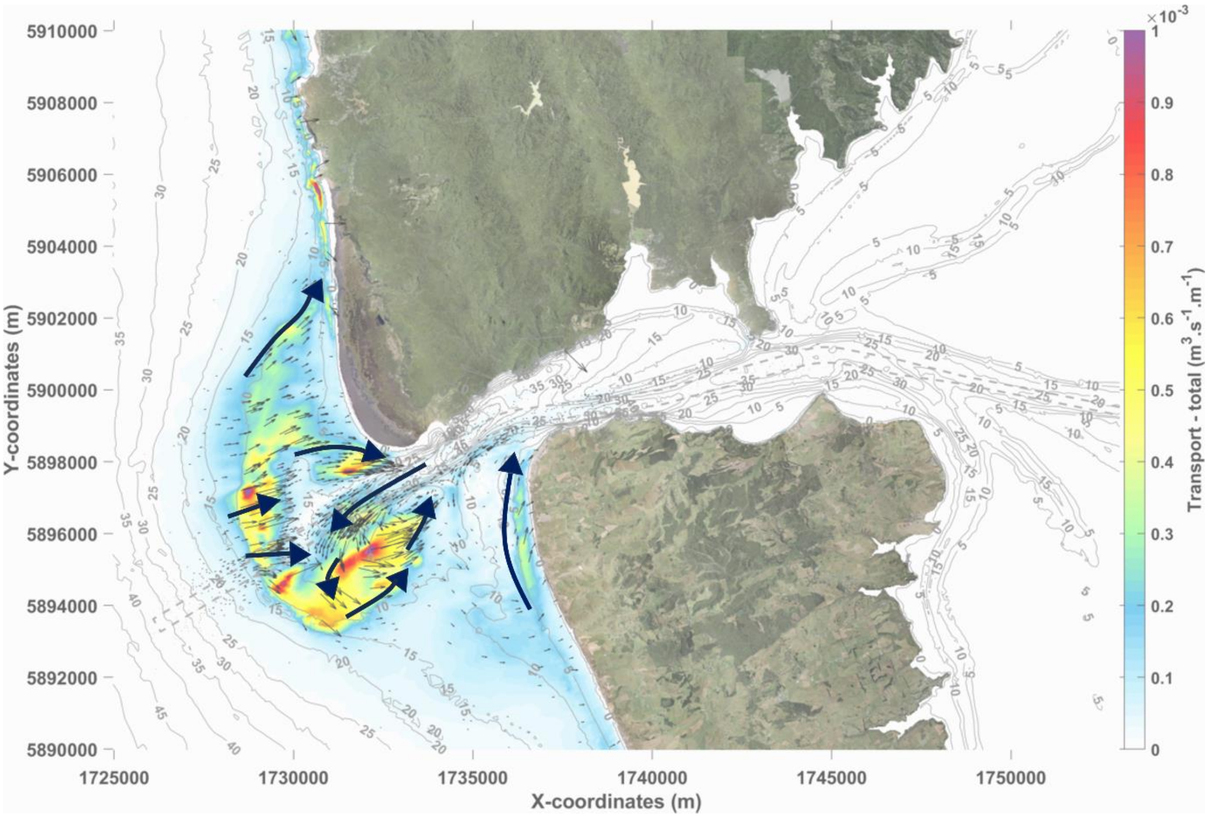

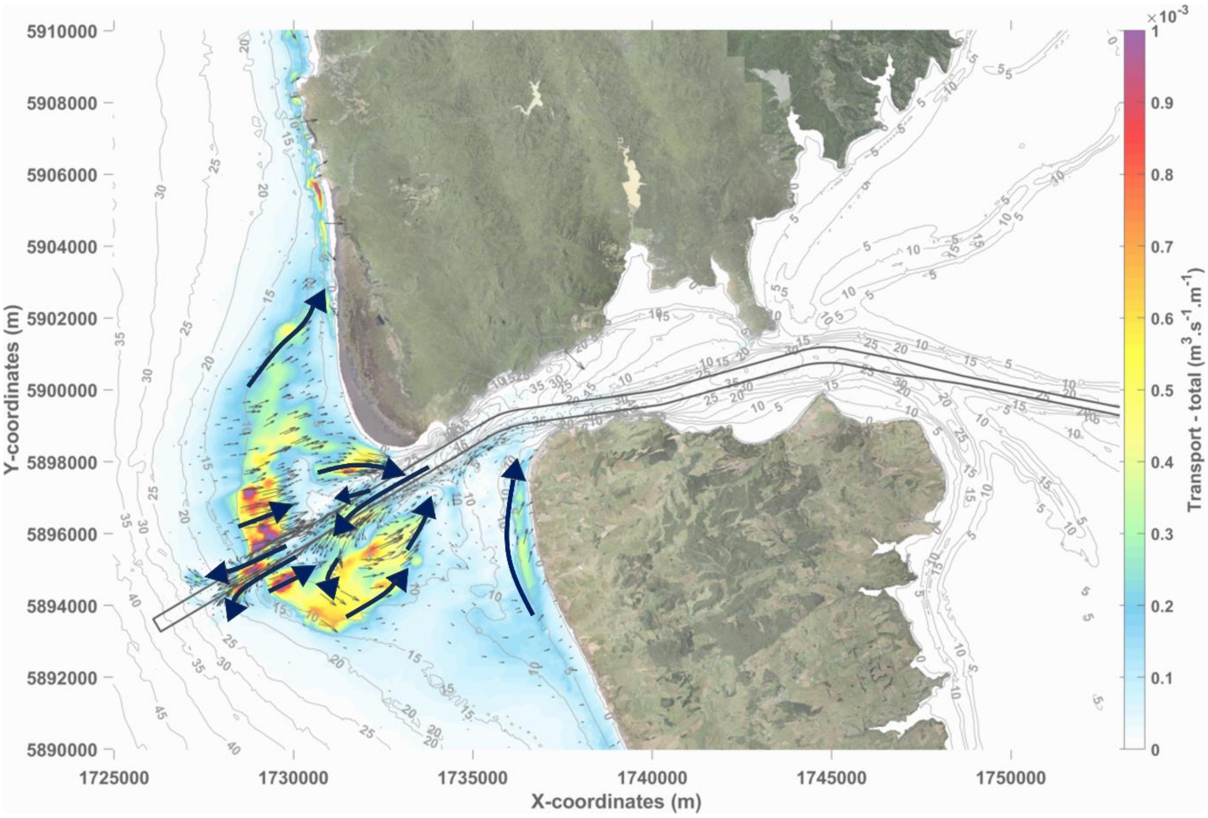

Figure 4-34 Sediment transport magnitude (colormap) and direction (thin black arrows) for runs including NW waves (H_s = 5 m, T_p = 15 s and Dir = 260 deg). Control 6, existing bathymetry (top) and Control 10, bathymetry including the concept navigation channel (bottom). Bold blue arrows represent the main transport pattern.

5 Sedimentation Assessment

5.1 Methodology

5.1.1 Input Reduction Scenario Matrix

In our approach to quantify sediment transport processes near the entrance bar of Manukau Harbour, we focused on the wave climate in the area to select Input Reduction (IR) events covering the range of wave conditions present at the site.

We first conducted a joint probability analysis of wave height (H_s) and direction (D_p) using the offshore wave hindcast (O1). The scatter plot of wave height, direction and period shown on Figure 5-1 illustrates how the wave climate is dominated by waves coming from between 230 and 260 degrees with heights ranging from 1 to 10 meters. An initial selection of IR scenarios was defined based on wave height varying in 1m increment, wave direction in 10° spacing and wave period in 1 second spacing.

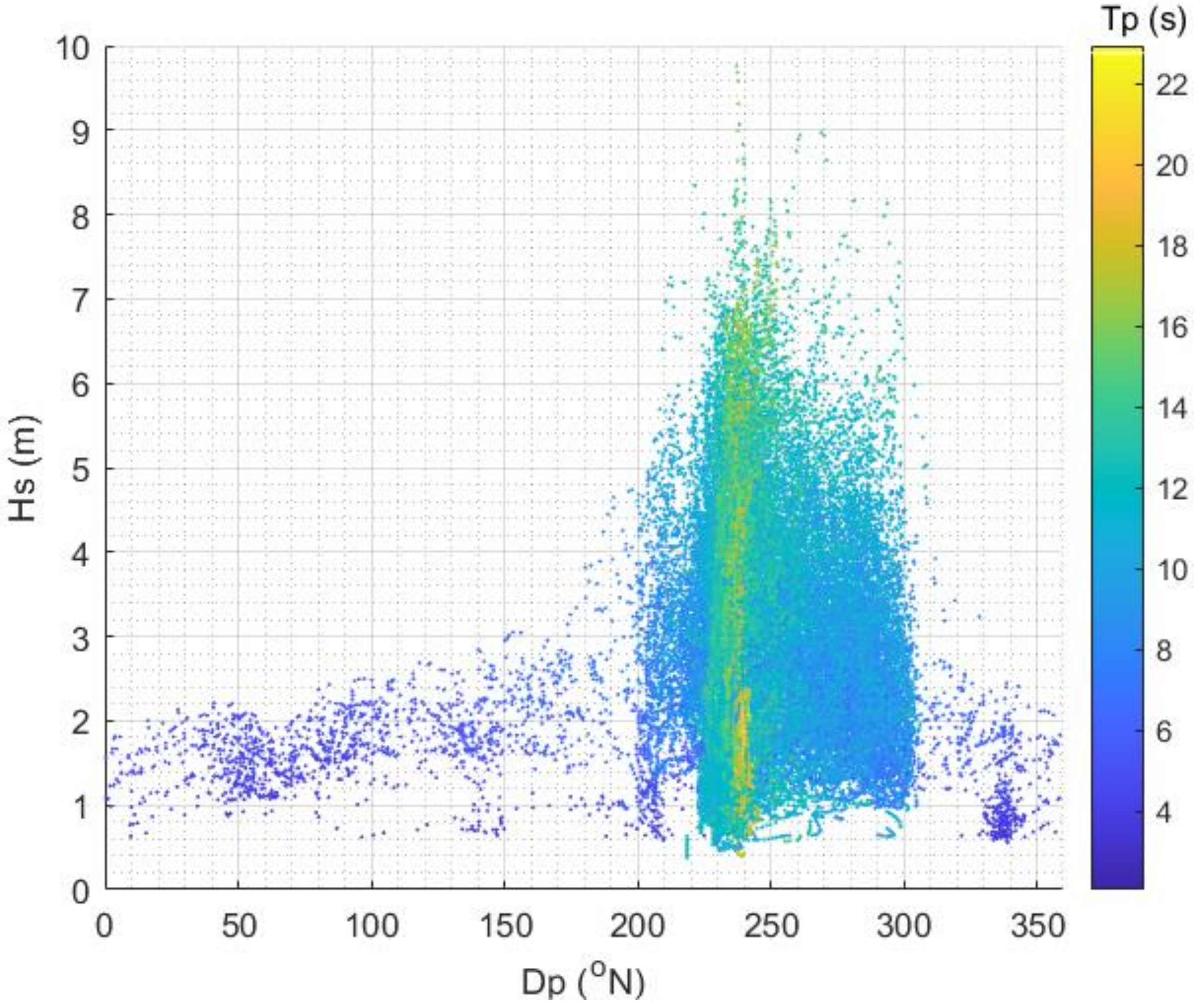

Figure 5-1 Selection of representative wave events using a joint probability of H_s and D_p.

Density scatter maps of the wave parameters from the offshore wave hindcast are presented together with the IR scenario wave forcing in Figure 5-2.

Our aim was to build a robust transformation matrix and ensure the full range of wave conditions were represented and that there was not an unrealistic extrapolation past lower and upper bounding parameters. As a result, extra runs were added that are less common but nonetheless important to bound the scatter interpolation function used to transform the wave hindcast.

The lowest H_s value used in the IR scenarios was 1 m, therefore the tide only run was used to set values for wave conditions of 0 m H_s which bound the lower portion of the transformation matrix and prevented the interpolation of negative infilling volumes for hindcast H_s less than 1 m.

The final set of scenarios used in the generation of the run matrix is displayed in Table 5-1.

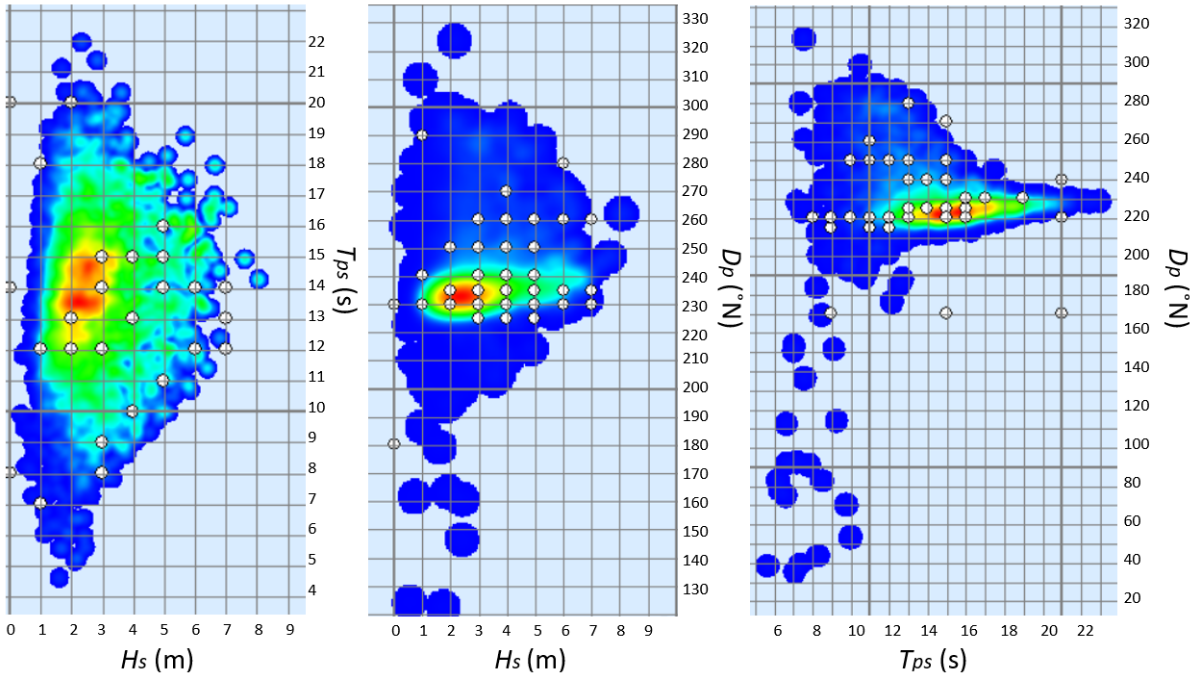

Figure 5-2 Heat density maps of the hindcast wave parameters (where red is the highest density of occurrence and blue is the least) and the wave forcing from the IR runs.

Table 5-1: Final scenarios used for the run matrix

Scenario	Bathy	Tide	H_s (m)	T_p (s)	D_p (˚N)
IR01	2023 channel	Typical	5	11	225
IR02	2023 channel	Typical	4	10	225
IR03	2023 channel	Typical	3	8	225
IR04	2023 channel	Typical	7	12	230
IR05	2023 channel	Typical	6	12	230
IR06	2023 channel	Typical	5	11	230
IR07	2023 channel	Typical	4	10	230
IR08	2023 channel	Typical	3	9	230
IR09	2023 channel	Typical	2	12	230
IR10	2023 channel	Typical	7	13	235
IR11	2023 channel	Typical	6	12	235
IR12	2023 channel	Typical	5	15	235
IR13	2023 channel	Typical	4	15	235
IR14	2023 channel	Typical	3	14	235
IR15	2023 channel	Typical	2	13	235
IR16	2023 channel	Typical	5	16	240
IR17	2023 channel	Typical	4	15	240
IR18	2023 channel	Typical	3	15	240
IR19	2023 channel	Typical	5	14	250
IR20	2023 channel	Typical	4	13	250
IR21	2023 channel	Typical	3	12	250
IR22	2023 channel	Typical	7	14	260
IR23	2023 channel	Typical	6	12	260
IR24	2023 channel	Typical	5	11	260
IR25	2023 channel	Typical	4	10	260
IR26	2023 channel	Typical	3	9	260
IR27	2023 channel	Typical	4	10	270
IR28	2023 channel	Typical	1	7	230
IR29	2023 channel	Typical	2	20	250
IR30	2023 channel	Typical	6	14	280
IR31	2023 channel	Typical	1	18	240
IR32	2023 channel	Typical	1	12	290
IR33*	2023 channel	Typical	5	15	230
IR34**	2023 channel	Typical	0	0	0

* IR33 is the same simulation as Control 7

** IR34 is the same simulation as Control 2

5.1.2 Transformation Process

A schematic of the transformation process used to determine the sediment infill estimate in presented on Figure *5-3*.

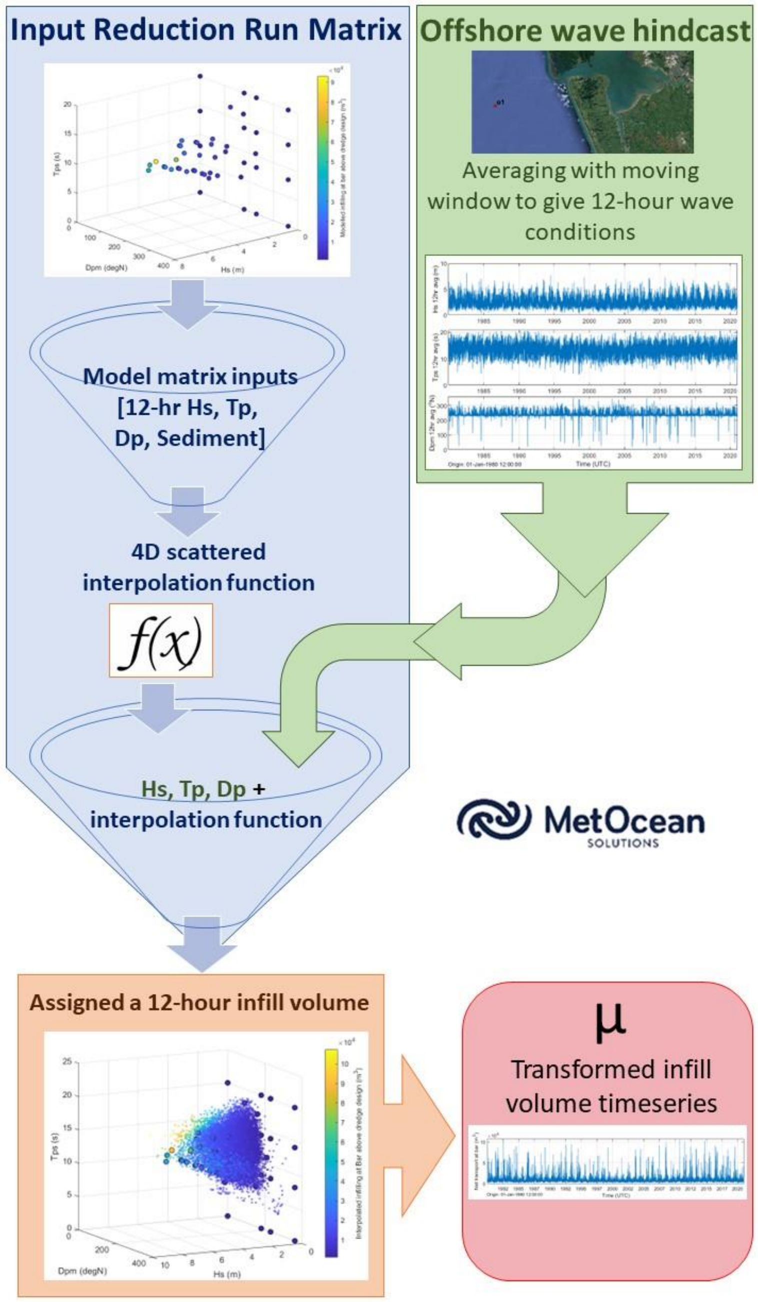

Figure 5-3: Schematic for the sediment infill estimate transformation process methodology.

The offshore 41-year (1980-2020) SWAN wave hindcast (with existing bathymetry) from model output location O1 was used which was in 70 m MSL water depth. The timeseries of the wave conditions used in the process is displayed in Figure 5-4. As the infilling and sedimentation results were calculated over 12-hour intervals the wave hindcast was resampled to give the 12-hour average wave conditions.

During processing the hindcast wave height was given an upper limit of 7 m, higher H_s values were set as 7 m. Due to the orientation of the coastline, any waves with a direction of northerly and easterly were set to have an H_s of 0 m which allocated them the tide only run volumes.

The transformation was undertaken through a 4D scattered interpolation using the IR scenarios (run matrix) shown in Table 5-1. The 12-hour wave parameter timeseries is interpolated against the run matrix and assigned a 12-hour infill volume. Figure 5-5 displays the interpolation of the hindcast infill volumes above design depth at the bar for the 41-year wave hindcast along with the values from the IR scenario (run matrix) used to create the scattered interpolation function. The transformed 12-hour infill volumes are presented in Section 5.2.1.

For the final annual infill estimate we have repeated this methodology by shifting the start of the 12-hour averaging window by one-hour increments. This was carried out to consider the joint occurrence of wave and tide over the 12-hours. A total of 12 sets of the sediment transport timeseries were prepared using the method in Figure *5-3* and were averaged to give the final infill timeseries.

A sensitivity analysis on climate change impacts on wave height was also undertaken. A 5% increase in H_s was applied to the hindcast to account for climate change. This value was arrived upon in the coastal processes report (TWP03), which suggests +5% increase to account for the impact of higher wave heights due to climate change on the transport and infill rates.

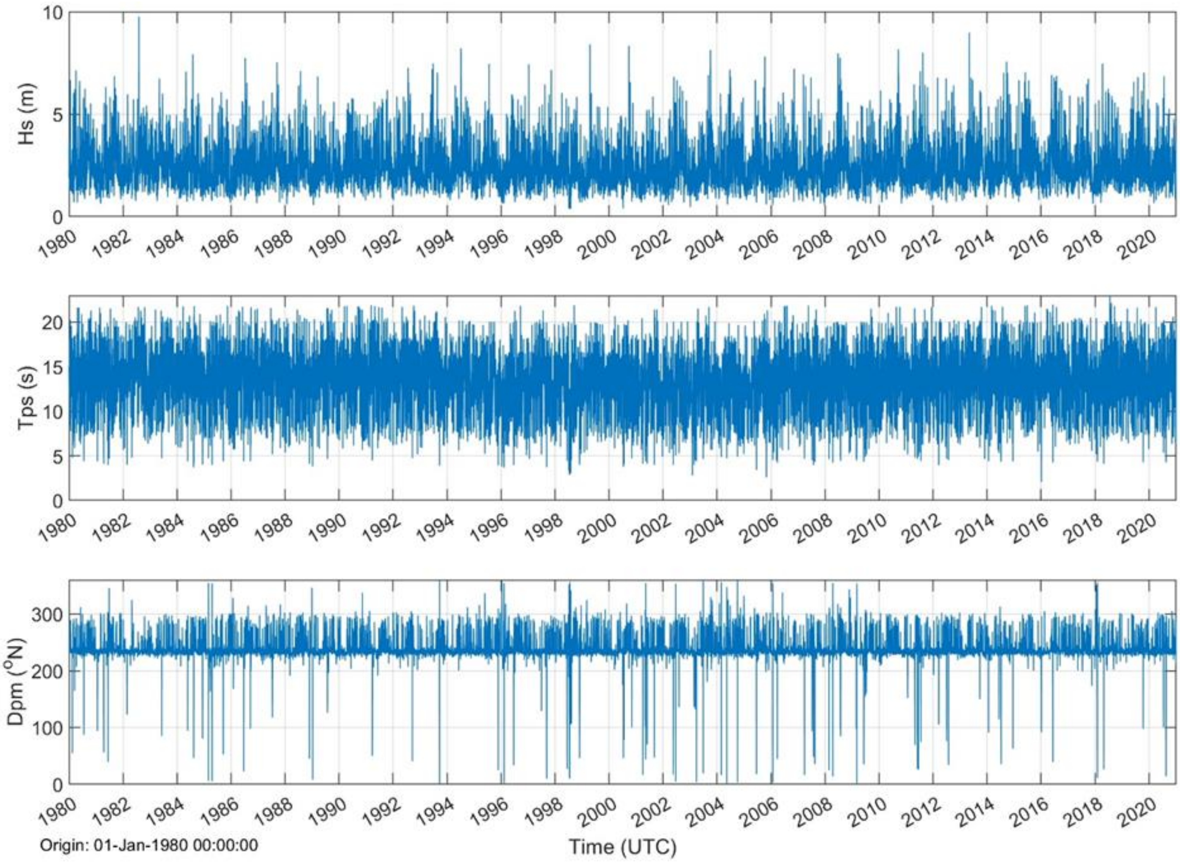

Figure 5-4 41-year wave hindcast from the existing simulation at site O1 (off the bar) in 70 m water depth.

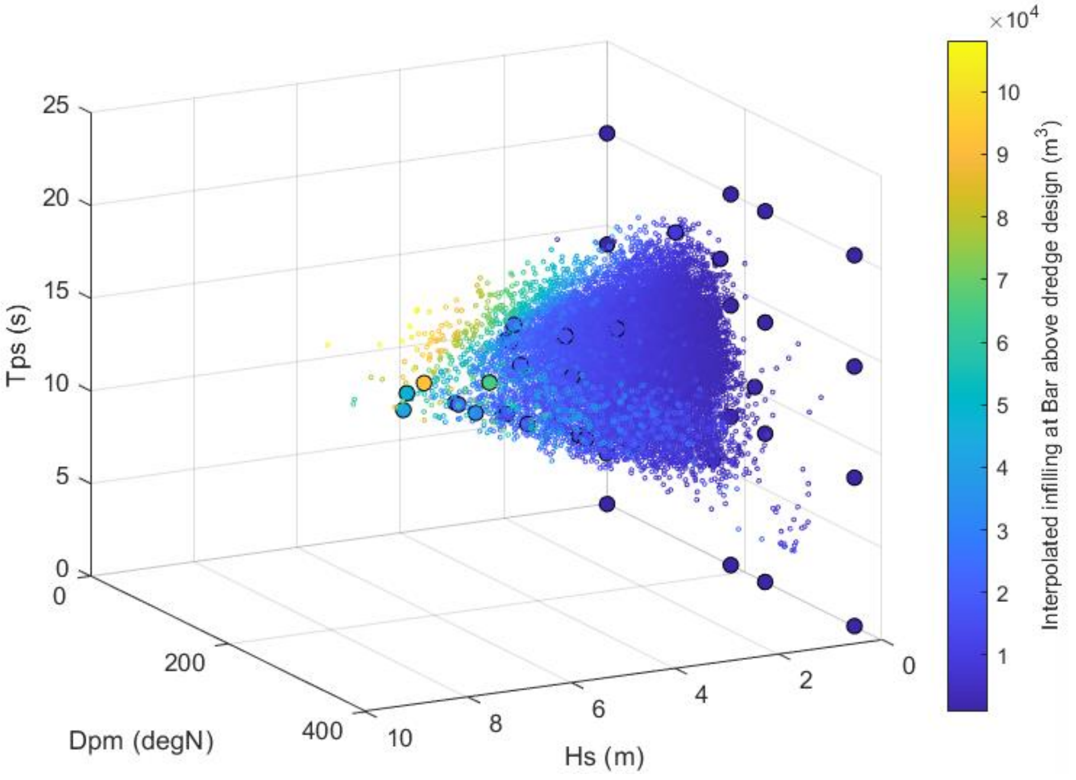

Figure 5-5 Interpolated hindcast infill volumes above design depth at the bar for the 41-year wave hindcast (small, coloured dots) and the values from the IR scenario run matrix (large, coloured dots).

5.1.3 Synthetic Storm

The aim to run a synthetic storm simulation was to determine if the IR method (several events of 12 hours each) provided an adequate representation of the infill that could occur during a continuous storm event of 10 days.

The approach involved constructing an event by stacking 12-hour blocks of the selected events, starting from no waves and progressively increasing wave height and corresponding period, followed by a decrease back to no waves (Figure 5-6). Each wave condition was run for 2 sets of 12 hours (24 hours), totalling 10 days. The aim of using 12-hour blocks of wave conditions was to compare the continuous long run (synthetic storm) with the results obtained from the separate 12-hour runs (IR runs) and transformation process for sediment infill estimate. Wave characteristics from selected IR scenarios included a range of wave heights and periods with H_s varying from 2 to 7 m and Tp from 9 to 12 s. The inclusion of no waves (H_s = 0 m and T_p = 0 s), IR34, was also considered (Table 5-2).

To facilitate the comparison with the IR runs, a synthetic tide was also created, repeating the typical 12-hour tide timeseries used in the control (and IR) simulations for the length of the synthetic storm run (Figure 5-7).

In the storm run, update in the bathymetry was considered throughout the simulation (i.e. morphological change was enabled). This means that changes in bed level resulting from sediment erosion and deposition will have a feedback mechanism, affecting the hydrodynamic and wave conditions, which will be adjusted in accordance with the updated bed morphology for every time step throughout the 10-day morphological run.

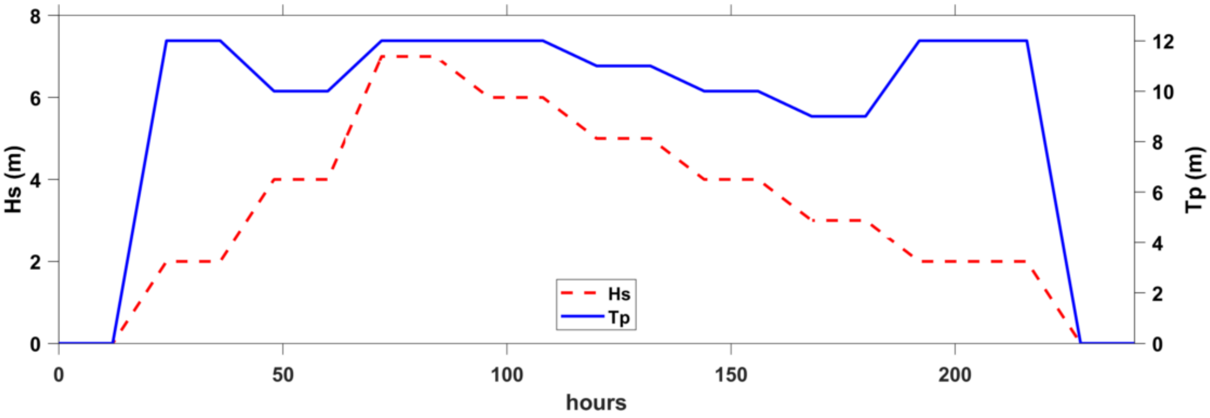

Figure 5-6 Synthetic timeseries of H_s and T_p used in the storm simulation.

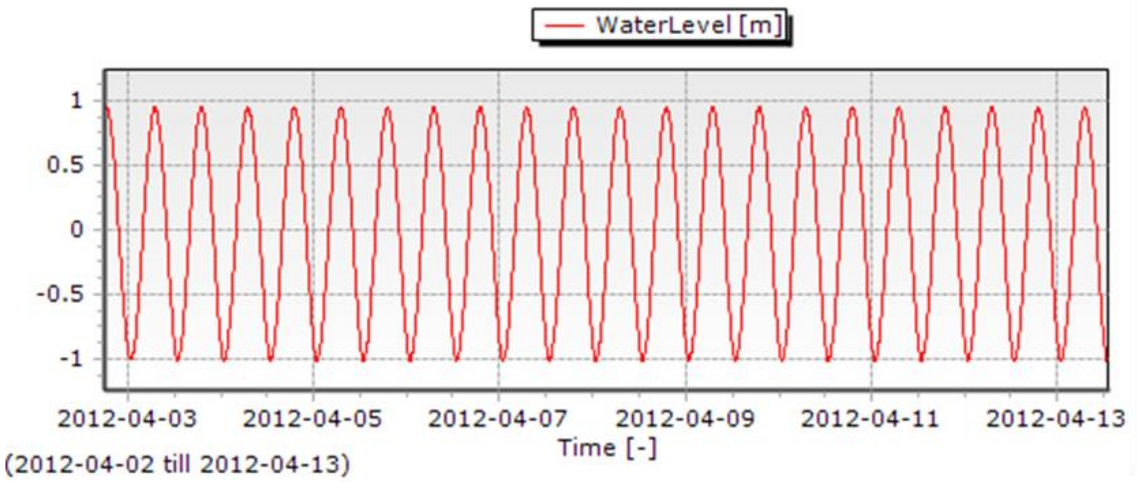

Figure 5-7 Example of synthetic tide timeseries used in one of the boundary points for the storm simulation.

Table 5-2: Selected events considered in the synthetic storm run.

Scenario	Bathy	Tide	H_s (m)	T_p (s)	D_p (°N)
IR04	2023 channel	Typical	7	12	230
IR05	2023 channel	Typical	6	12	230
IR06	2023 channel	Typical	5	11	230
IR07	2023 channel	Typical	4	10	230
IR08	2023 channel	Typical	3	9	230
IR09	2023 channel	Typical	2	12	230
IR34	2023 channel	Typical	0	0	0

5.2 Results

5.2.1 Predicted Bar Annual Infill

The 41-year wave hindcast (O1) was transformed to give the 12-hour infill volumes above the design depth and the 12-hour net sediment transport volumes. The areas for analysis of the sedimentation results are the same as those used in the control scenarios that are described in Section 4.2. The 41-year timeseries of 12-hour infill volumes at the bar that were above the design depth are presented in Figure 5-8.

Table 5-3 and Table 5-4 present the annual volumes at the bar which are the final cumulative values at the end of the calendar year. The annual infill volume above the design depth is presented in Table 5-3 and the annual net sediment transport/infill is presented in Table 5-4. A sensitivity analysis on climate change impacts on wave height was also undertaken. A 5% increase in H_s was applied to the hindcast to account for the impact of higher wave heights due to climate change on the transport and infill rates. The percentage increase in annual volumes due to the 5% increase in Hs are also displayed alongside the annual volumes in Table 5-3 and Table 5-4.

The annual cumulative infill volume at the bar above the design depth is presented in Figure 5-9. The annual cumulative net infill volume at the bar is presented in Figure 5-10. The annual totals and Figure 5-9 suggest that there is quite a big change in bed level above design depth at the bar with infill rates between 5.03M to 7.68M m^3/year (average of 6.54M m^3/year). Whereas the small annual net change between -0.33M to -1.33M m^3/year suggests that while there is a high volume of sediment moving at the bar there is also a large amount of net loss/erosion. This is supported by observations of the existing channel not rapidly filling with sediment at the rates suggested by considering the infill volume above design depth alone.

With a potential increase in wave height of 5% due to climate change the increase is a mean annual infill is about 500,000 m^3/year (6.54M m^3/year to 7.06M m^3/year) or about 8% increase in infill. The maximum annual infill calculated is then 8.37M m3 for the year 2016.

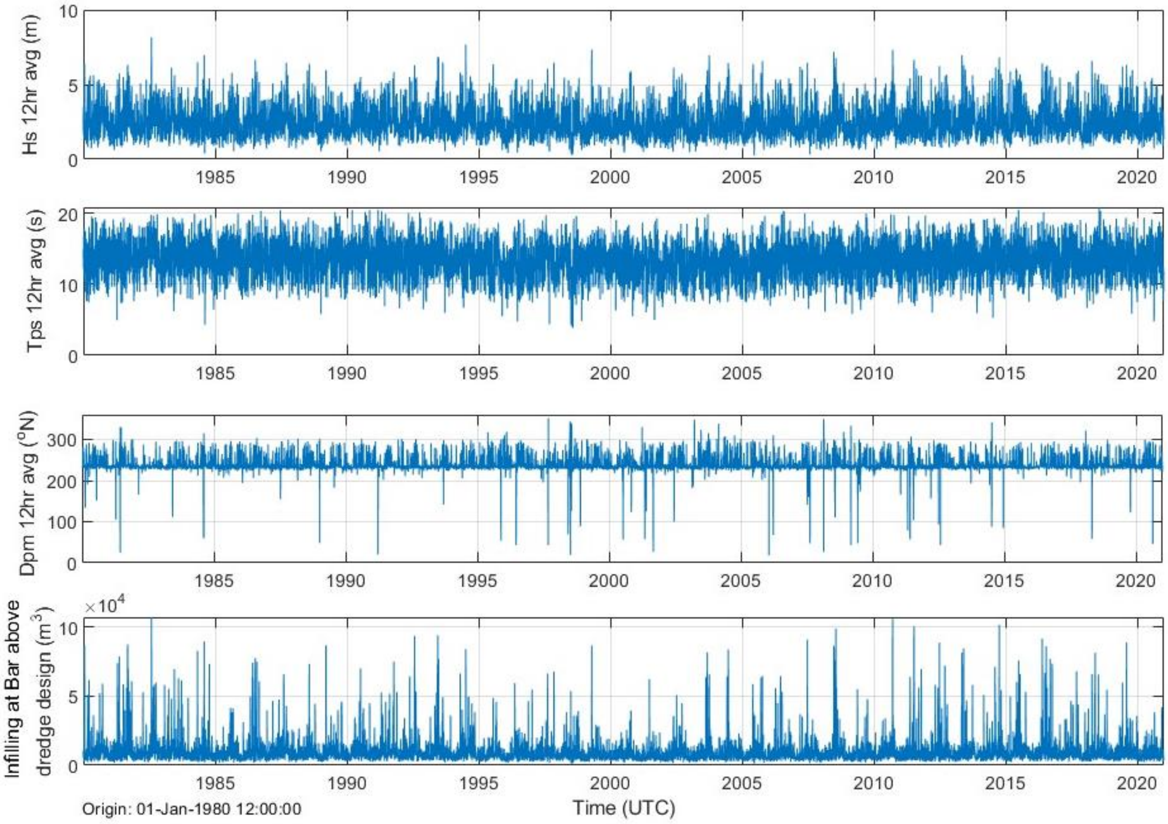

Figure 5-8 12-hour average wave hindcast parameters and the transformed 12-hour infill volumes above the design depth at the bar.

Table 5-3: Transformed annual total infill volumes above design depth at the bar and the percentage increase in annual infill volumes when a 5% increase in H_s is applied to the hindcast to account for climate change.

Year	Annual infill volume above design depth at the bar (m^3)	Percentage increase in annual infill volumes with 5% increase in H_s (%)	Year	Annual infill volume above design depth at the bar (m^3)	Percentage increase in annual infill volumes with 5% increase in H_s (%)
1980	7,033,938	8.62	**2001**	5,028,516	6.67
1981	7,293,770	9.59	**2002**	5,951,463	7.78
1982	7,327,464	8.43	**2003**	5,913,538	7.01
1983	7,584,902	8.70	**2004**	6,266,218	7.13
1984	6,234,956	7.04	**2005**	5,698,267	7.93
1985	5,617,267	7.25	**2006**	6,753,417	7.54
1986	7,152,115	7.77	**2007**	5,794,436	7.84
1987	7,253,170	8.65	**2008**	6,896,680	7.86
1988	6,572,767	7.31	**2009**	5,820,080	7.64
1989	6,308,108	7.00	**2010**	6,725,632	7.72
1990	7,056,954	7.95	**2011**	7,004,177	8.62
1991	7,482,474	8.20	**2012**	6,771,356	8.51
1992	6,970,360	7.96	**2013**	6,511,849	8.05
1993	7,313,246	8.05	**2014**	7,302,090	8.04
1994	6,905,200	8.49	**2015**	7,360,727	8.42
1995	5,887,713	6.76	**2016**	7,680,120	9.07
1996	5,694,240	7.08	**2017**	6,361,201	7.70
1997	6,206,409	7.26	**2018**	6,691,272	7.73
1998	6,222,551	7.44	**2019**	6,756,975	9.02
1999	5,509,075	6.59	**2020**	5,929,605	6.98
2000	5,539,336	7.03			

Table 5-4: Transformed annual total net infill volumes at the bar and the percentage increase in annual infill volumes when a 5% increase in H_s *is applied to the hindcast to account for climate change.*

Year	Annual net infill volume at the bar (m^3)	Percentage increase in annual infill volumes with 5% increase in H_s (%)	Year	Annual net infill volume at the bar (m^3)	Percentage increase in annual infill volumes with 5% increase in H_s (%)
1980	-1,057,772	14.89	**2001**	-331,910	38.06
1981	-642,382	5.99	**2002**	-528,645	26.44
1982	-1,329,532	9.42	**2003**	-373,468	33.94
1983	-1,192,464	9.02	**2004**	-789,979	22.43
1984	-642,346	22.43	**2005**	-364,486	23.00
1985	-612,649	20.01	**2006**	-952,606	14.61
1986	-750,272	15.33	**2007**	-550,925	19.04
1987	-1,055,816	10.76	**2008**	-569,560	16.13
1988	-879,789	19.74	**2009**	-571,605	21.09
1989	-890,336	17.97	**2010**	-1,050,831	15.11
1990	-992,112	12.42	**2011**	-476,439	14.15
1991	-1,122,931	14.30	**2012**	-781,930	12.09
1992	-911,891	14.69	**2013**	-891,908	14.51
1993	-1,001,500	12.52	**2014**	-1,100,171	12.24
1994	-928,890	11.89	**2015**	-1,222,399	11.85
1995	-751,026	20.92	**2016**	-1,180,874	9.64
1996	-435,641	32.15	**2017**	-751,732	18.05
1997	-852,284	16.02	**2018**	-854,539	15.21
1998	-670,261	15.79	**2019**	-1,019,840	10.31
1999	-523,204	25.34	**2020**	-700,017	21.72
2000	-548,328	25.32			38.06

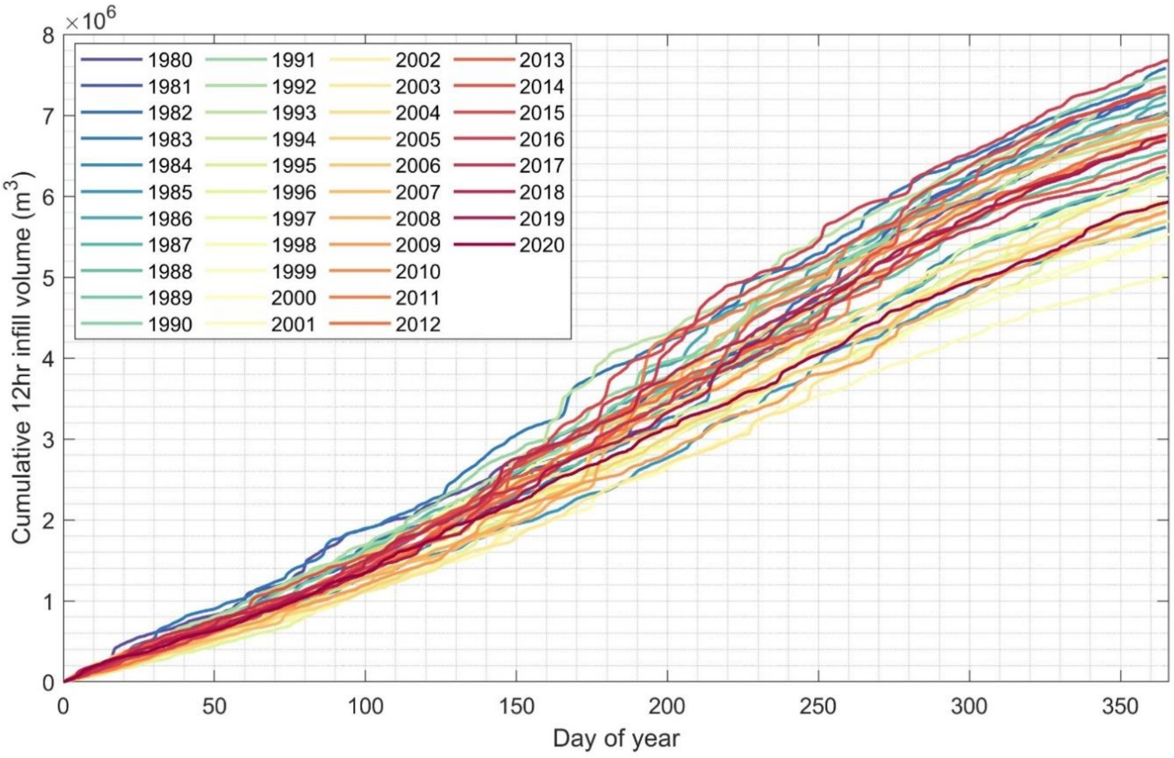

Figure 5-9 Annual cumulative infill volumes at the bar above the design depth over the 41-year period.

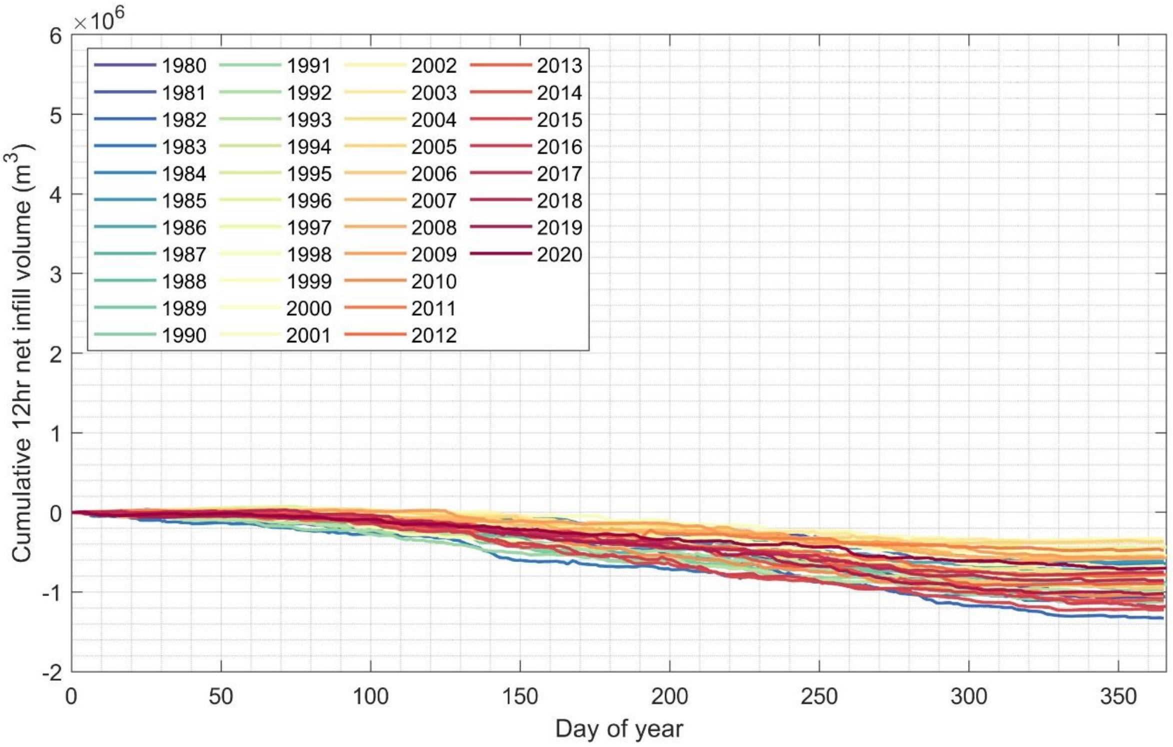

Figure 5-10 Annual cumulative net sedimentation volumes at the bar over the 41-year period.

5.2.2 Sediment Infill During Storm Event

Results of cumulative and net infill volumes for the storm event are presented in Table 5-5 and Figure 5-11.

Comparing results from IR with the storm event, cumulative volumes derived from the IR results yielded more conservative estimates, indicating approximately 20% more infill compared to the continuous synthetic storm run at the end of the simulation.

Throughout the storm event simulation, significant infill occurs as wave height increases, resulting in positive net infill. Cumulative rates tend to decelerate, particularly when the wave height (H_s) starts to decrease. Net sediment budget changes to erosive, showing a rapid increase in net erosion for wave heights decreasing from 7 m to 5 m. Once wave heights reach around 4 meters, net infill tends to stabilize, becoming slightly less erosive when H_s drops to less than 2 m towards the end of the simulation (Figure 5-11).

Map of deposition above design depth (Figure 5-12) and profile 1 (Figure 5-13) show that the majority of infill within the channel is situated just before the batter slope area and at the terminal lobe, while erosion is evident in between these areas of deposition in the channel. Comparatively high deposition is situated around the batter slopes, particularly the southern batter slope as shown in profile 2 (Figure 5-13).

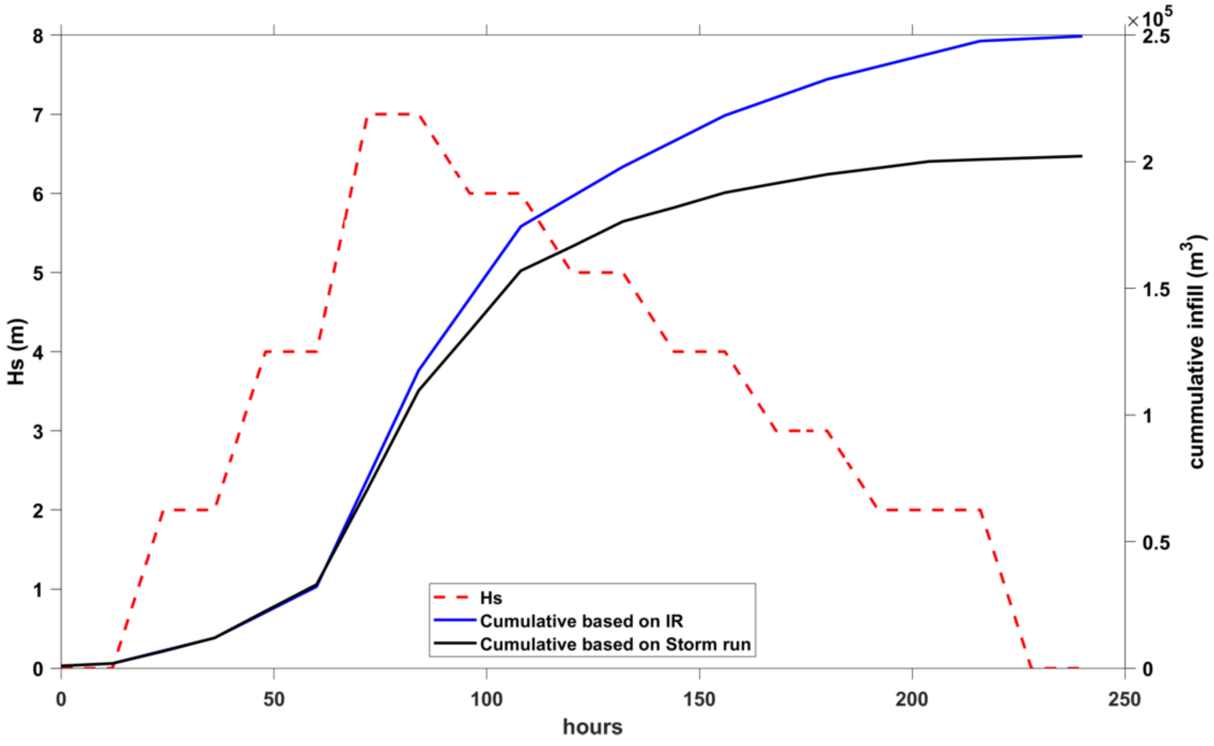

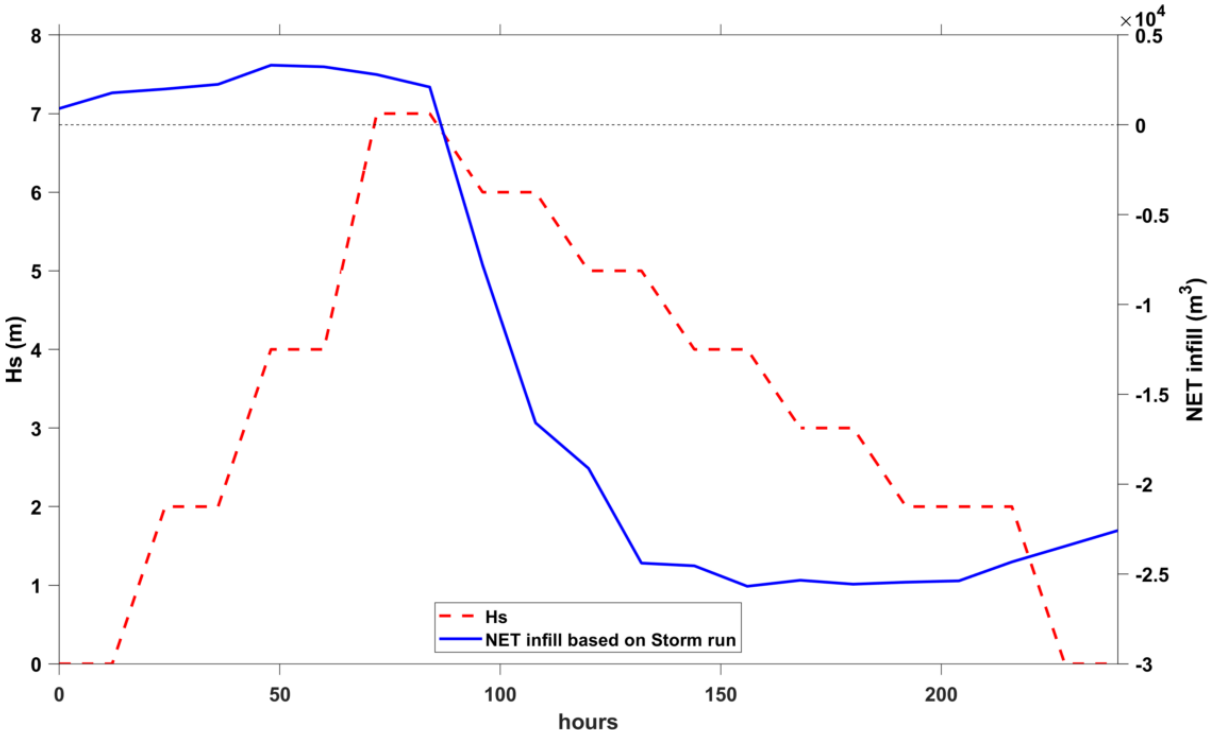

Figure 5-11 Cumulative (top) and net (bottom) infill from the synthetic storm scenario with modelled H_S.

Table 5-5: Sedimentation results from the synthetic storm scenario. Infill volumes for the 'bar' (polygons 3+4+5+6).

Timestep	Time (hrs)	Tide	H_s (m)	T_p (s)	D_p (˚N)	Infill Bar - deposition above design depth after 12h (m^3) – from IR and Control runs	Cumulative based on IR and Control runs	Cumulative based on continuous model (synthetic storm)	NET Infill Bar (m^3)
1	0	Typical	0	0	230	944	944	943	908
2	12	Typical	0	0	230	944	1,888	1,880	1,779
3	24	Typical	2	12	230	5,042	6,930	6,717	1,993
4	36	Typical	2	12	230	5,042	11,972	11,973	2,251
5	48	Typical	4	10	230	10,136	22,108	22,586	3,318
6	60	Typical	4	10	230	10,136	32,244	33,049	3,229
7	72	Typical	7	12	230	42,681	74,925	70,823	2,795
8	84	Typical	7	12	230	42,681	117,606	109,650	2,101
9	96	Typical	6	12	230	28,414	146,020	133,095	-7,813
10	108	Typical	6	12	230	28,414	174,434	156,940	-16,590
11	120	Typical	5	11	230	11,784	186,218	166,477	-19,122
12	132	Typical	5	11	230	11,784	198,002	176,414	-24,396
13	144	Typical	4	10	230	10,136	208,138	181,874	-24,546
14	156	Typical	4	10	230	10,136	218,274	187,798	-25,685
15	168	Typical	3	9	230	7,126	225,400	191,452	-25,350
16	180	Typical	3	9	230	7,126	232,526	195,003	-25,567
17	192	Typical	2	12	230	5,042	237,568	197,518	-25,457
18	204	Typical	2	12	230	5,042	242,610	200,112	-25,382
19	216	Typical	2	12	230	5,042	247,652	200,873	-24,329
20	228	Typical	0	0	230	944	248,596	201,534	-23,460
21	240	Typical	0	0	230	944	249,540	202,198	-22,584

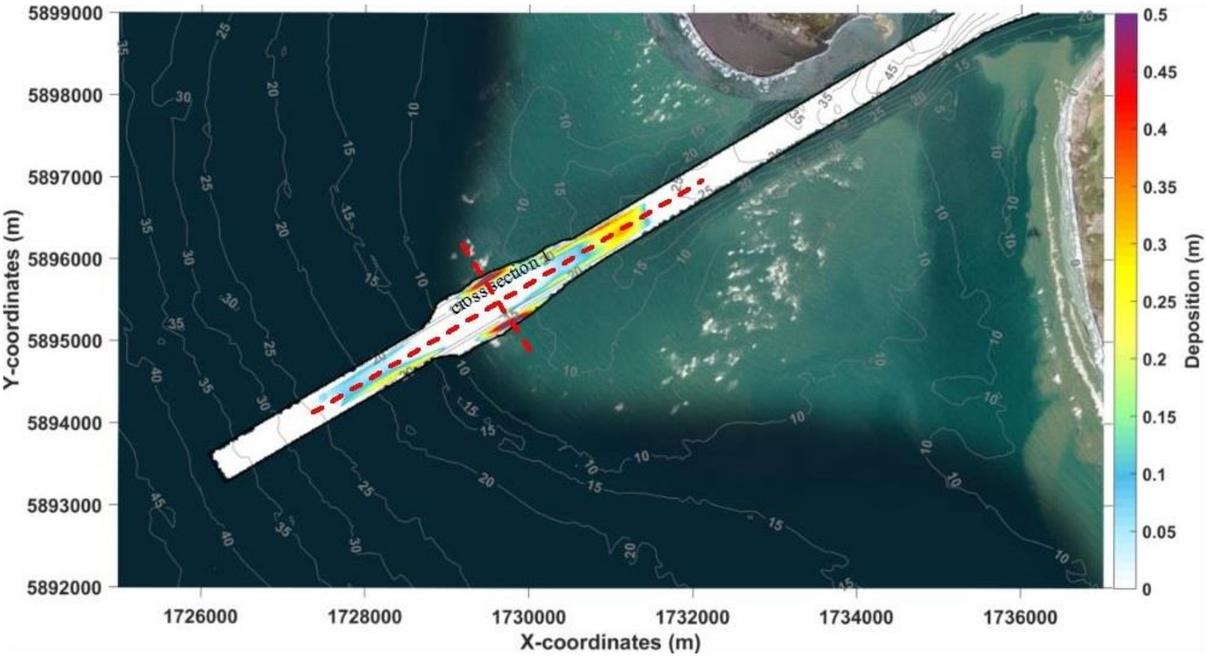

Figure 5-12 Deposition above design depth at the end of the storm run. Red lines show the location of two transects used to extract model results.

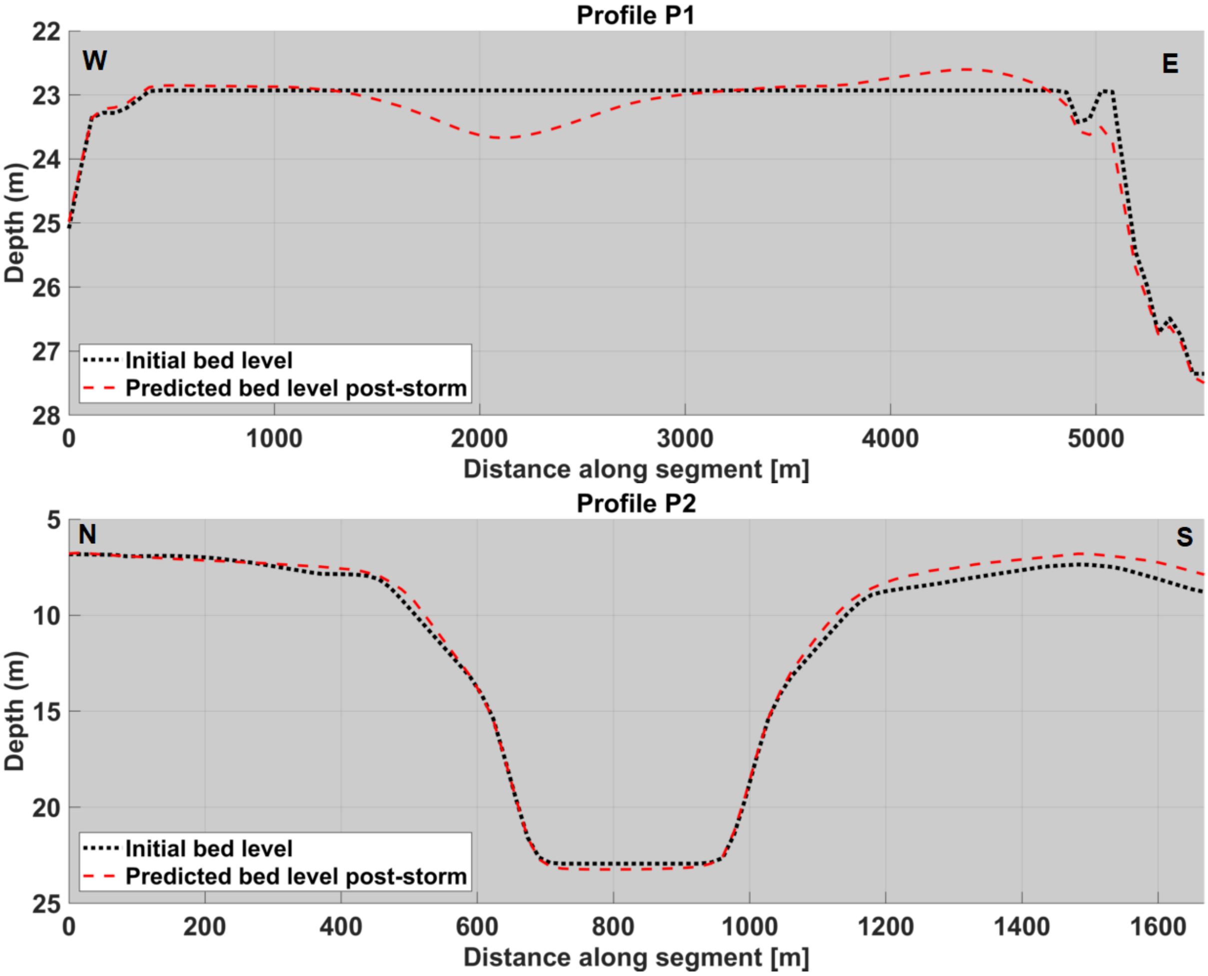

Figure 5-13 Profile along the channel (Profile 1, top) and across the channel and batter slopes (Profile 2, bottom).

5.2.3 Sediment Infill Post Storm Event

As shown in the results of sediment infill (net infill in Table 4-2 and Table 5-4) and erosion/deposition maps (e.g. Section 4.3), the channel presents areas of accumulation that are both below and above design depth and areas of erosion. The net infill indicates that, when considering both volumes of erosion and accumulation, the channel area covered by polygons 3, 4, 5, and 5 is mostly erosive, and the channel itself is potentially a significant contributor to the infill.

A key consideration for the long-term predictions of sediment infill is, in an extended period of time as the bathymetry evolves, the channel might erode (or stabilise) to a point when it will reduce its contribution to the overall infill.

To investigate the role of the channel as the main contributor of sediment to the infill, we re-ran a 12-h control run (Control 7, including channel, Hs = 5 m, Tp = 15 s and Dir = 230 deg) to assess if similar accumulation and erosion rates occur over an already deepened bathymetry (compared to the initial design depth bathymetry). We used the post-storm bathymetry for this run (see profiles in Figure 5-13). Any accumulation above design depth was removed to simulate dredging (Figure 5-14, blue line).

Results in Table 5-6 show that there is about 10% less accumulation for the run starting with the dredged bathymetry. Erosion rate is reduced by approximately 5% for this run compared to the original control 7 after 12h. It shows that erosion could potentially reduce over time affecting the infill rates, however, long-term processes have not been modelled. Results also show that accumulation and erosion of sediments reduces at different rates, suggesting that material contributing to channel infill could potentially be originating from elsewhere other than the channel itself.

Other sources of sediment to the channel according to the model results are likely the longshore transport from south of the entrance and sediment originating from erosion of the bar due to waves, along with the transportation by currents into the channel.

Maps of erosion and sedimentation (Figure 5-15) illustrate the reduced deposition in the southern batter compared to the previous Control 7 run. There is also increased transport out of the channel on the west side of the northern batter.

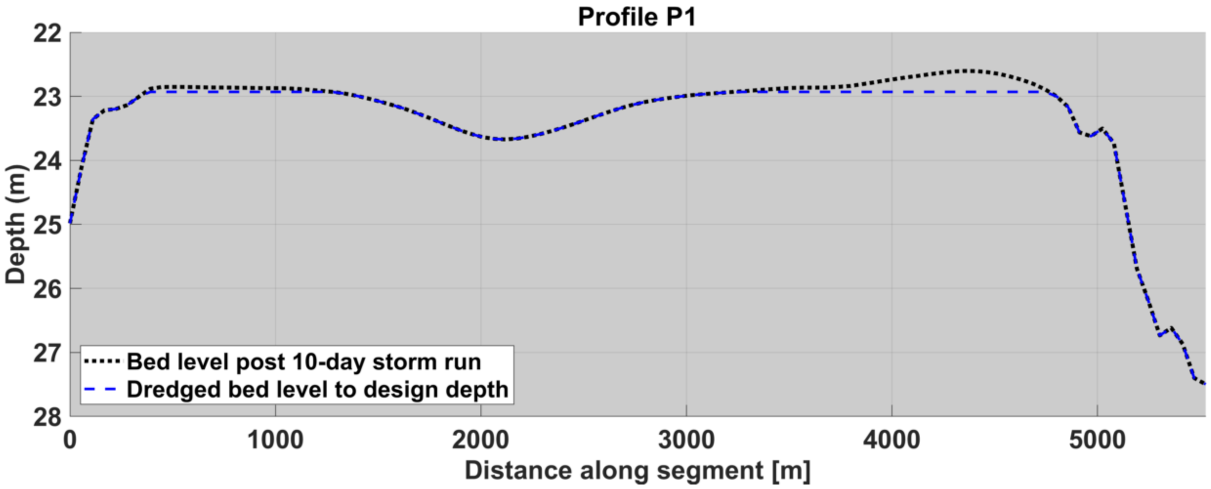

Figure 5-14 Profile along the channel (Profile 1) showing the post-storm bathymetry (black dotted line) and the dredged bathymetry (blue dashed line) representing the removal of any accumulation above the design depth.

Table 5-6: Infill results for Control 7 (original bathymetry including channel) and for Control 7 ran with initial bathymetry represented by a post-storm condition and with accumulation dredged to design depth. Wave forcing Hs = 5 m, Tp = 15 s and Dir = 230 deg. Infill volumes for the 'bar' (polygons 3+4+5+6).

	Control 7	**Control 7 after storm DREDGED**
Accretion	30,591	27,407
Erosion	-38,179	-36,255
NET	-7,589	-8,848
Accretion above design	23,979	21,468

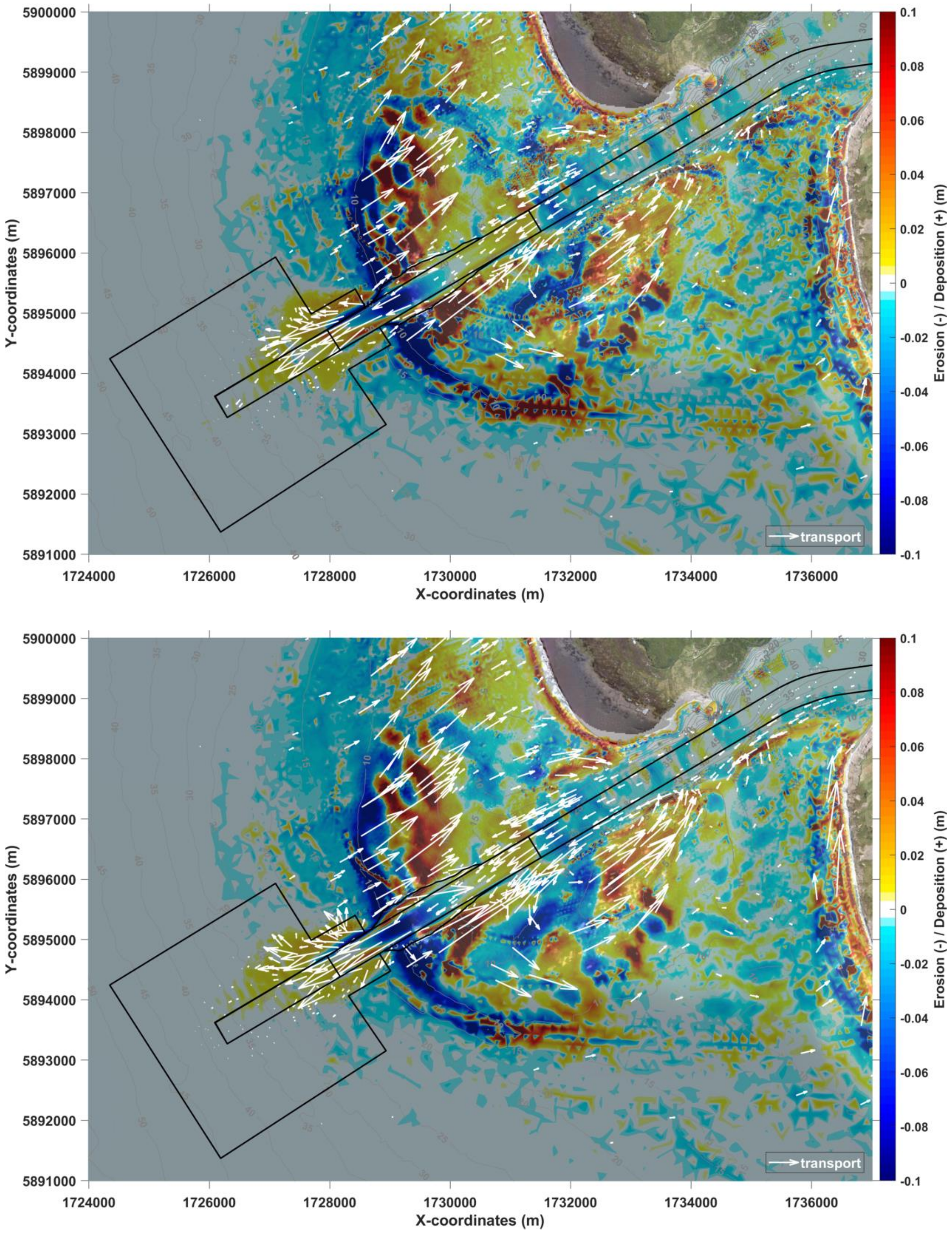

Figure 5-15 Maps of erosion (negative, blue) and deposition (positive, red) results for runs including the channel and forced by southwest waves (H_s = 5 m, T_p = 15 s and Dir = 230 deg). Top map shows results for Control 7 runs using the original bathymetry and bottom map is for Control 7 with modified initial bathymetry represented by a post-storm condition and with accumulation dredged to design depth.

5.2.4 Navigation Channel Infill Sensitivity

As shown in Section 5.2.2, infill results from the storm event simulation were compared with an estimate of the sediment infill using the same methodology as the annual prediction, i.e. the wave climate in 12 hours block was used to calculate the sediment infill. Results showed that the transformation process led to approximately 20% more sediment infill than the continuous storm even simulation. This indicates that the transformation process methodology is slightly conservative in its estimation of the total infill.

Results from the simulations with different sediment fraction i.e. 150 μm (fine sands), 250 μm (medium sands) and 500 μm (coarse sands), presented in Section 4.2, showed large difference in the sediment infill estimates. The sediment transport and predicted infill is typically two (2) to three (3) time larger with fine sands than medium sand, and about twice as large for medium sands compared to coarse sands. The particle size distribution analysis of the sediment samples within the entrance bar system showed that fine and medium sands are present on the bar and medium to coarse sands are present within the South West Channel. The medium sand fraction used in the detailed modelling assessment provide an averaged representation of the predicted sediment infill. However, with a combination of the model results to allow for a seabed sediment composed of 10% fine sands, 80% medium sands and 10% coarse sands the total sediment infill is roughly about 20% higher due to the larger component of fine sand infill.

This sensitivity analysis indicates that whilst our transformation process methodology to define the annual infill may be conservative by approximately 20%, the consideration for a single medium sand fraction (250 μm) may be underpredicting the infill estimate by about 20%. These assumptions and model limitations are each affecting the results in opposing manner, so results are likely accurate within +/- 20%, which is a reasonable outcome for the overall annual estimate of approximately 6.5 M m^3/year (or 5.03M to 7.68M m^3/year variability as shown in Section 5.2.1.

5.2.5 South Channel Assessment

Two navigation channels entering the harbour were initially assessed (refer to Technical Working Paper 04 – Navigation), a South West and South orientated channel. The South West channel was preferred based on lower capital dredge volumes (by about 50%) and stakeholder preference for a South West orientation. The detailed modelling therefore progressed with the South West channel.

The high sediment infill rates determined for the South West channel brought the South channel back in to question. To test likely infill rates of the South channel we ran a typical scenario similar to the control runs (H_s = 5 m, T_p = 15 s and Dir = 230 deg) using the 'design' bathymetry with the deepened South Channel (same depth and width as the South West channel). Given that this was a high-level investigation of the South Channel option, only one scenario was simulated. Results from this run show minimal erosion/deposition within the channel. The main erosion and deposition occur along the batter slopes, with the northern batter exhibiting significant deposition while the southern batter is showing erosion (Figure 5-16).

The deposition of the batters and the reduced scouring in the channel (compared to the South West channel) is likely a combination of short terms adjustment and onshore movement of the southern bar. The alignment of the channel to the wave forcing conditions likely contributes to the contrasting patterns of erosion/deposition observed in the results. The South channel is aligned at approximately 205 deg while the South West channel is aligned at approximately 240 deg compared to the most common incoming waves (230 deg).

Infill calculations were carried out both with and without the batter slopes (Figure 5-16), and the results are shown in Table 5-7. Deposition within the channel (excluding batter slopes) is 5,386 m^3. Including the batter slopes in the calculations, the total deposition is 48,916 m^3. This volume is approximately 1.6 times greater than the sediment calculated within polygons 3+4+5+6 for the South West channel under the same forcing conditions (30,591m^3 – Control 7). Assuming a 1.6 factor between the South West channel and the South Channel option, the annual infill would then be about 10.4M m^3/year on average and up to 12.3M m^3/year for the South Channel.

It is important to note that the simulation only used 250-μm sand as the sediment fraction, and sediment samples suggest a finer sediment distribution along the South Channel (Figure 2-3). Therefore, this volume could potentially be underestimated.

This assessment presents a preliminary overview to draw comparisons to the South West channel infill rates. To better characterise the sediment infill rates further modelling would be required for the South channel for comparison.

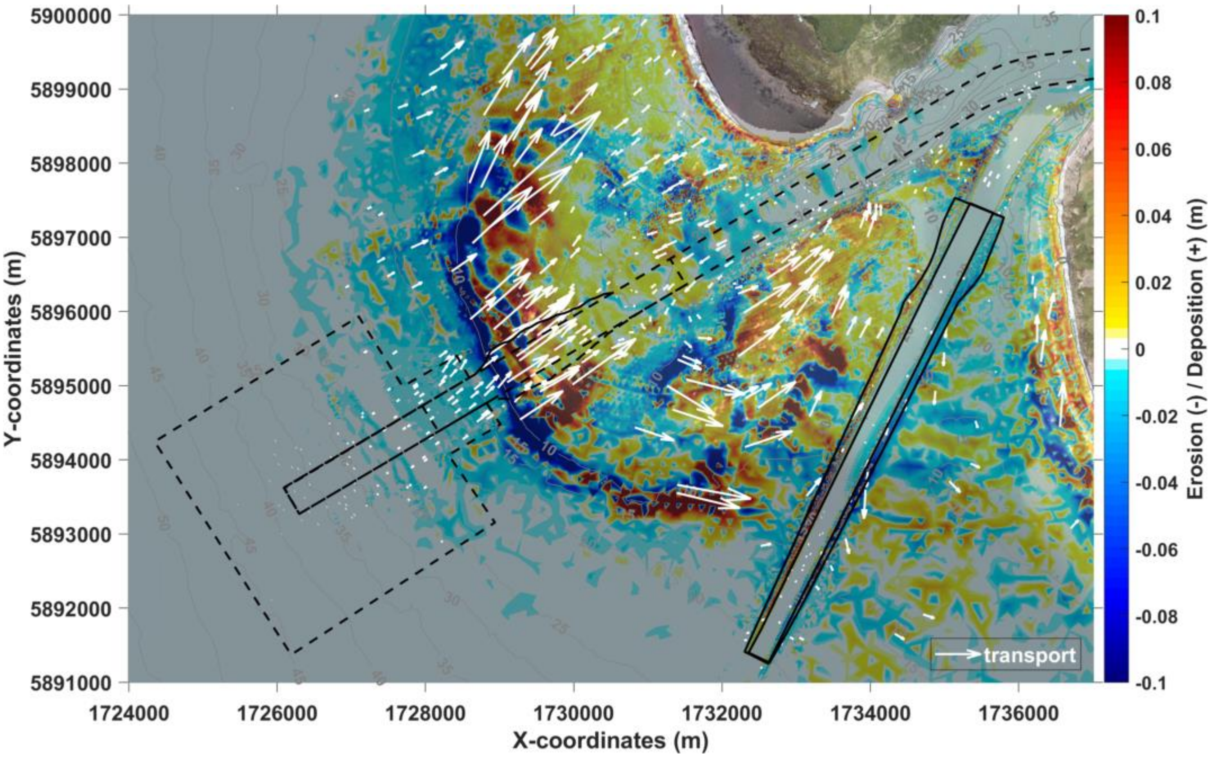

Figure 5-16 Map of erosion (negative, blue) and deposition (positive, red) for scenario using the deepened South channel bathymetry. Arrows show transport direction. Solid black lines represent the polygons used to calculate infill rates in the South channel.

Table 5-7: Infill results from the South channel scenario and results for the South West (Control 7, H_s = 5 m, T_p = 15 s and Dir = 230 deg) run for comparison. S = South, SW = South West.

	S-channel channel	**S-channel channel+batters**	**SW-channel (Control 7) channel**	**SW-channel (Control 7) channel+batters**
Accretion (m^3)	5,386	48,916	20,536	30,591
Erosion (m^3)	-6,278	-53,070	-31,120	-31,120
NET (m^3)	-892	-4,155	-10,584	-7,589

6 References

Deltares. (2014). *User Manual Delft3D-Functional Specifications. Draft version 2.20. Deltares.*

Deltares. (2023). *D-Morphology, 1D/2D/3D. User Manual.* (Version: 2023).

Goda, Y. (2007). *How much do we know about wave breaking in the nearshore waters.* 65–86.

Kamphuis, J. W. (2000). *Introduction to coastal engineering and management* (Advanced Series on Ocean Engineering, Vol. 16). World Scientific Publishing. https://www.worldscientific.com/worldscibooks/10.1142/7021

Ridderinkhof, M., de Swart, H. E., van der Vegt, M., & Hoekstra, P. (2016). Modeling the growth and migration of sandy shoals on ebb-tidal deltas. *Journal of Geophysical Research: Earth Surface*, *121*, 1351–1372. https://doi.org/10.1002/2016JF003823

Tonkin & Taylor Ltd. (2024a). *Manukau Harbour Port Feasibility Study: Coastal—Final Technical Working Paper* (TWP03). Report prepared for Ministry of Transport.

Tonkin & Taylor Ltd. (2024b). *Manukau Harbour Port Feasibility Study: Fieldwork Techincal Working Paper* (TWP02). Report prepared for Ministry of Transport.

Van Rijn, L. C., Walstra, D. J. R., & Ormondt, M. van. (2004). Description of TRANSPOR2004 and Implementation in Delft3D-ONLINE. *Z3748*.

van Rijn, L. C., Walstra, D. J. R., & van Ormondt, M. (2004). *Description of TRANSPOR2004 and implementation in Delft3D-ONLINE : final report* (Z3748.10; p. 77).

Appendix A: Sediment Transport Model Parameters and Description

Table A-1: Parameters used for the sediment transport modelling.

Parameter	Description	Value
Sediment transport		
Non – Cohesive Sediment (Sand)		
RhoSol	Sediment density (kg/m^3)	3000
SedTyp	Sediment type	Sand
SedDia	Median sediment diameter (D50) (m)	0.00025
cDryB	Dry bed density (kg/m^3)	1800
IFORM	Sediment transport formulation	(TR2004, Van Rijn et al., 2004)
Morphology		
BedUpd	update bed level during flow run	false
AlfaBs	Streamwise bed gradient factor for bed load transport [-]	1
AlfaBn	Transverse bed gradient factor for bed load transport [-]	1.5
Sus	Multiplication factor for suspended sediment reference concentration [-]	1
Bed	Multiplication factor for bed-load transport vector magnitude [-]	1
SusW	Wave-related suspended sediment transport factor [-]	1
BedW	Wave-related bed-load sediment transport factor [-]	1
SedThr	Minimum water depth for sediment computations [m]	0.1

Below is presented a short description of the general formulation used in the sediment transport modelling (Delft3D-FM). The text is extracted from the User Manual of D-Morphology (Deltares, 2023).

Sediment transport and morphology

A.1 General formulations

A.1.1 Introduction

The sediment transport and morphology module supports both bedload and suspended load transport of non-cohesive sediments and suspended load of cohesive sediments.

A.1.2 Suspended transport

Three-dimensional transport of suspended sediment is calculated by solving the three-dimensional advection-diffusion (mass-balance) equation for the suspended sediment:

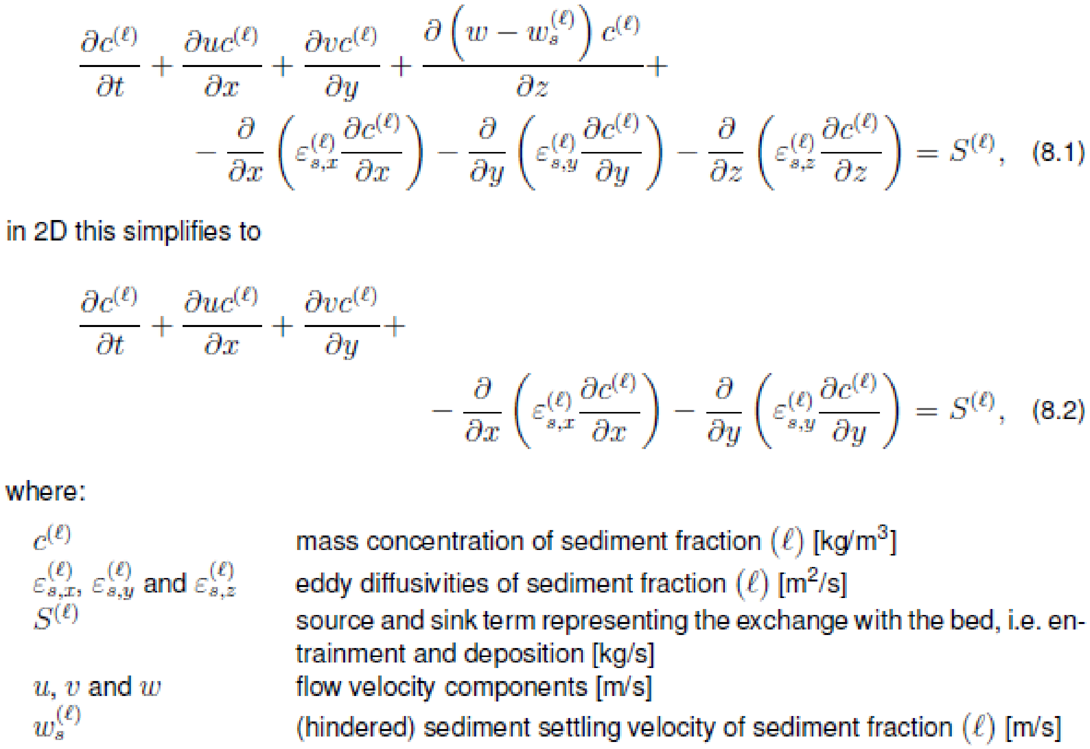

$$\frac{\partial c^{(\ell)}}{\partial t} + \frac{\partial u c^{(\ell)}}{\partial x} + \frac{\partial v c^{(\ell)}}{\partial y} + \frac{\partial \left(w - w_s^{(\ell)}\right) c^{(\ell)}}{\partial z} + \\ - \frac{\partial}{\partial x}\left(\varepsilon_{s,x}^{(\ell)} \frac{\partial c^{(\ell)}}{\partial x}\right) - \frac{\partial}{\partial y}\left(\varepsilon_{s,y}^{(\ell)} \frac{\partial c^{(\ell)}}{\partial y}\right) - \frac{\partial}{\partial z}\left(\varepsilon_{s,z}^{(\ell)} \frac{\partial c^{(\ell)}}{\partial z}\right) = S^{(\ell)}, \qquad (8.1)$$

in 2D this simplifies to

$$\frac{\partial c^{(\ell)}}{\partial t} + \frac{\partial u c^{(\ell)}}{\partial x} + \frac{\partial v c^{(\ell)}}{\partial y} + \\ - \frac{\partial}{\partial x}\left(\varepsilon_{s,x}^{(\ell)} \frac{\partial c^{(\ell)}}{\partial x}\right) - \frac{\partial}{\partial y}\left(\varepsilon_{s,y}^{(\ell)} \frac{\partial c^{(\ell)}}{\partial y}\right) = S^{(\ell)}, \qquad (8.2)$$

where:

$c^{(\ell)}$	mass concentration of sediment fraction (ℓ) [kg/m^3]
$\varepsilon_{s,x}^{(\ell)}$, $\varepsilon_{s,y}^{(\ell)}$ and $\varepsilon_{s,z}^{(\ell)}$	eddy diffusivities of sediment fraction (ℓ) [m^2/s]
$S^{(\ell)}$	source and sink term representing the exchange with the bed, i.e. entrainment and deposition [kg/s]
u, v and w	flow velocity components [m/s]
$w_s^{(\ell)}$	(hindered) sediment settling velocity of sediment fraction (ℓ) [m/s]

The local flow velocities and eddy diffusivities are based on the results of the hydrodynamic computations. The suspended sediment transport is computed largely in the same way as the transport of any other conservative constituent, such as salinity, heat, and constituents. There are, however, a number of important differences between sediment and other constituents, for example, the exchange of sediment between the bed and the flow, and the settling velocity of sediment under the action of gravity.

Other processes such as the effect that sediment has on the density of the fluid-sediment mixture, and hence on turbulence damping, can also be taken into account. In addition, a net flux of sediment from the bed to the flow, or vice versa, results in bed level changes which subsequently influence the hydrodynamic calculations. The formulation of several of these processes (such as, settling velocity, sediment deposition and pick-up) are sediment-type specific, this especially applies for sand and mud. Furthermore, the interaction of sediment fractions is important for many processes, for instance the simultaneous presence of multiple suspended sediment fractions has implications for the calculation of the local hindered settling velocity of any one sediment fraction as well as for the resulting mixture density.

A.2 Non-cohesive sediment

For the transport of non-cohesive sediment, Van Rijn et al. (2000) approach is followed by default. You can also specify a number of other transport formulations (see section 8.5).

A.2.1 Non-cohesive sediment settling velocity

The settling velocity of a non-cohesive ("sand") sediment fraction is computed following the method of Van Rijn (1993). The formulation used depends on the diameter of the sediment in suspension:

$$w_{s,0}^{(\ell)} = \begin{cases} \dfrac{(s^{(\ell)}-1)gD_s^{(\ell)2}}{18\nu}, & 65\ \mu\text{m} < D_s \leq 100\ \mu\text{m} \\ \dfrac{10\nu}{D_s}\left(\sqrt{1+\dfrac{0.01(s^{(\ell)}-1)gD_s^{(\ell)3}}{\nu^2}}-1\right), & 100\ \mu\text{m} < D_s \leq 1000\ \mu\text{m} \\ 1.1\sqrt{(s^{(\ell)}-1)gD_s^{(\ell)}}, & 1000\ \mu\text{m} < D_s \end{cases} \tag{8.19}$$

where:

$s^{(\ell)}$	relative density $\rho_s^{(\ell)}/\rho_w$ of sediment fraction(ℓ)
$D_s^{(\ell)}$	representative diameter of sediment fraction (ℓ)
ν	kinematic viscosity coefficient of water [m^2/s]

A.2.2 Non-cohesive sediment dispersion

The output of a turbulence closure model is the eddy viscosity at each layer interface; from this the vertical sediment mixing coefficient is calculated using the following expressions.

Including waves

If waves are included in a simulation using the algebraic or k-L turbulence closure model then the sediment mixing coefficient for non-cohesive sediment fractions is calculated entirely separately from the turbulence closure model, using expressions given by Van Rijn (1993) for both the current-related and wave-related vertical turbulent mixing of sediment.

The current-related mixing is calculated using the 'parabolic-constant' distribution recommended by Van Rijn:

$$\varepsilon_{s,c}^{(\ell)} = \begin{cases} \kappa \beta u_{*,c} z(1 - z/h), & \text{when } z < 0.5h, \\ 0.25 \kappa \beta u_{*,c} h, & \text{when } z \geq 0.5h, \end{cases} \tag{8.21}$$

where:

$\varepsilon_{s,c}^{(\ell)}$	vertical sediment mixing coefficient due to currents (for this sediment fraction)
$u_{*,c}$	current-related bed shear velocity

In the lower half of the water column this expression should produce similar turbulent mixing values to those produced by the algebraic turbulence closure model. The turbulent mixing in the upper half of the water column is generally of little importance to the transport of 'sand' sediment fractions as sediment concentrations in the upper half of the water column are low.

The wave-related mixing is also calculated following Van Rijn (1993). The expressions used to set this distribution are:

$$\varepsilon_{s,w}^{(\ell)} = \begin{cases} \varepsilon_{s,bed}^{(\ell)} = 0.004 D_* \delta_s^{(\ell)} & \text{when } z \leq \delta_s^{(\ell)}, \\ \varepsilon_{s,bed}^{(\ell)} + \left(\varepsilon_{s,\max}^{(\ell)} - \varepsilon_{s,bed}^{(\ell)} \right) \left(\dfrac{z - \delta_s^{(\ell)}}{0.5h - \delta_s^{(\ell)}} \right), & \text{when } \delta_s^{(\ell)} < z < 0.5h, \\ \varepsilon_{s,\max}^{(\ell)} = \dfrac{0.035 \gamma_{br} h H_s}{T_p}, & \text{when } z \geq 0.5h, \end{cases} \tag{8.22}$$

where $\delta s^{(\ell)}$ (the thickness of the near-bed sediment mixing layer) is estimated using Van Rijn's formulation, given by:

$$\delta_s^{(\ell)} = \min\left[0.5, \max\left\{0.1, \max\left(5\gamma_{br}\delta_w, 10\gamma_{br}k_{s,w}\right)\right\}\right] \tag{8.23}$$

where:

δ_w thickness of the wave boundary layer:

$$\delta_w = 0.072\hat{A}_\delta\left(\frac{\hat{A}_\delta}{k_{s,w}}\right)^{-0.25} \tag{8.24}$$

γ_{br} empirical coefficient related to wave breaking:

$$\gamma_{br} = \begin{cases} 1 + \left(\frac{H_s}{h} - 0.4\right)^{0.5} & \text{when } \frac{H_s}{h} > 0.4 \\ 1 & \text{when } \frac{H_s}{h} \leq 0.4 \end{cases} \tag{8.25}$$

$k_{s,w}$ wave-related bed roughness (as calculated for suspended sediment transport)

We calculate the total vertical sediment mixing coefficient by following Van Rijn and taking the sum of the squares:

$$\varepsilon_s^{(\ell)} = \sqrt{\varepsilon_{s,c}^{(\ell)2} + \varepsilon_{s,w}^{(\ell)2}}, \tag{8.26}$$

where ε_s is the vertical sediment diffusion coefficient used in the suspended sediment transport calculations for this sediment fraction.

A.2.3 Reference concentration

For non-cohesive sediment (e.g. sand), we follow the method of Van Rijn (1993) for the combined effect of waves and currents. The reference height is given by:

$$a = \min\left[\max\left\{\text{AksFac} \cdot k_s, \frac{\Delta_r}{2}, 0.01h\right\}, 0.20h\right], \tag{8.30}$$

where:

a	Van Rijn's reference height
AksFac	user-defined proportionality factor (morphology input file)
k_s	user-defined current-related effective roughness height (see options below)
Δ_r	wave-induced ripple height, set to a constant value of 0.025 m
h	water depth

Calculation of the reference concentration

The reference concentration c_a is calculated directly by the sediment transport formula ormit is derived from the suspended sediment transport rate given by the sediment transport formula as ca = Ss/Hu. The default transport formula (Van Rijn, 1993) includes a formula for the reference concentration (see section 8.5.3). The reference concentration is adjusted proportional to the relative availability of the sediment fraction in the top-layer of the bed (see section 8.6.4 on bed composition models).

A.2.4 Non-cohesive sediment erosion and deposition in 3D

The transfer of sediment between the bed and the flow is modelled using sink and source terms acting on the near-bottom layer that is entirely above Van Rijn's reference height. This layer is identified as the reference layer and for brevity is referred to as the kmx-layer; see Figure 8.2.

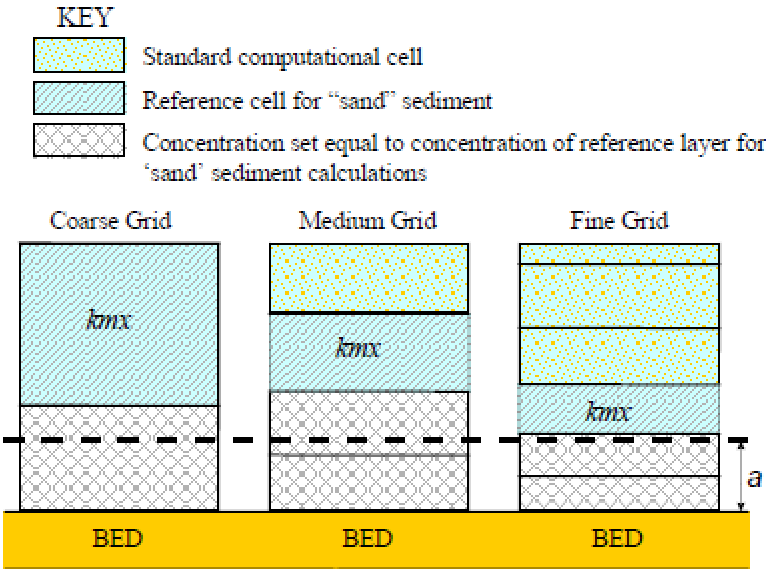

Figure 8.2: Selection of the kmx layer; where a is Van Rijn's reference height

The sediment concentrations in the layer(s) that lie below the kmx layer are assumed to rapidly adjust to the same concentration as the reference layer. Each half time-step the source and sink terms model the quantity of sediment entering the flow due to upward diffusion from the reference level and the quantity of sediment dropping out of the flow due to sediment settling. A sink term is solved implicitly in the advection-diffusion equation, whereas a source term is solved explicitly. The required sink and source terms for the kmx layer are calculated as follows.

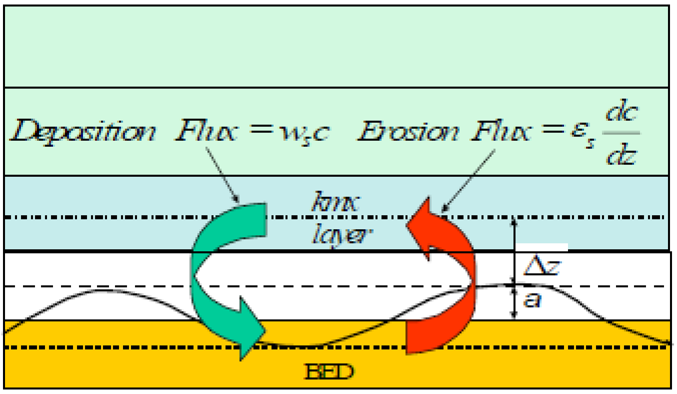

Figure 8.3: *Schematic arrangement of flux bottom boundary condition*

In order to determine the required sink and source terms for the kmx layer, the concentration and concentration gradient at the bottom of the kmx layer need to be approximated. We assume a standard Rouse profile between the reference level *a* and the centre of the kmx layer (see Figure 8.4).

$$c^{(\ell)} = c_a^{(\ell)} \left(\frac{a(h-z)}{z(h-a)} \right)^{A^{(\ell)}}, \tag{8.31}$$

where:

$c^{(\ell)}$	concentration of sediment fraction (ℓ)
$c_a^{(\ell)}$	reference concentration of sediment fraction (ℓ)
a	Van Rijn's reference height
h	water depth
z	elevation above the bed
$A^{(\ell)}$	Rouse number

As the reference concentration and the concentration in the centre of the kmx layer c_{kmx} are known, the exponent A(ℓ) can be determined.

$$c_{kmx}^{(\ell)} = c_a^{(\ell)} \left(\frac{a(h-z_{kmx})}{z_{kmx}(h-a)} \right)^{A^{(\ell)}} \Rightarrow A^{(\ell)} = \frac{\ln\left(\frac{c_{kmx}}{c_a}\right)}{\ln\left(\frac{a(h-z_{kmx})}{z_{kmx}(h-a)}\right)} \tag{8.32}$$

The concentration at the bottom of the kmx layer is:

$$c_{kmx(bot)}^{(\ell)} = c_a^{(\ell)} \left(\frac{a(h-z_{kmx(bot)})}{z_{kmx(bot)}(h-a)} \right)^{A^{(\ell)}} \tag{8.33}$$

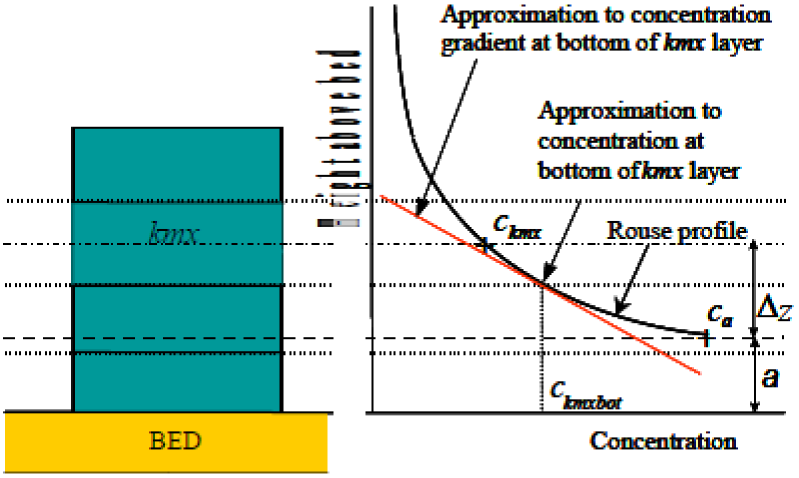

Figure 8.4: Approximation of concentration and concentration gradient at bottom of kmx layer

We express this concentration as a function of the known concentration c_{kmx} by introducing a correction factor α_1:

$$c^{(\ell)}_{kmx(bot)} = \alpha_1^{(\ell)} c^{(\ell)}_{kmx} \tag{8.34}$$

The concentration gradient of the Rouse profile is given by:

$$\frac{\partial c^{(\ell)}}{\partial z} = A^{(\ell)} c_a^{(\ell)} \left(\frac{a(h-z)}{z(h-a)}\right)^{A^{(\ell)}-1} \cdot \left(\frac{-ah}{z^2(h-a)}\right) \tag{8.35}$$

The concentration gradient at the bottom of the *kmx* layer is:

$$c'^{(\ell)}_{kmx(bot)} = A^{(\ell)} c_a^{(\ell)} \left(\frac{a(h-z_{kmx(bot)})}{z_{kmx(bot)}(h-a)}\right)^{A^{(\ell)}-1} \cdot \left(\frac{-ah}{z^2_{kmx(bot)}(h-a)}\right) \tag{8.36}$$

We express this gradient as a function of the known concentrations c_a and c_{kmx} by introducing another correction factor α_2:

$$c'^{(\ell)}_{kmx(bot)} = \alpha_2^{(\ell)} \left(\frac{c^{(\ell)}_{kmx} - c_a^{(\ell)}}{\Delta z}\right) \tag{8.37}$$

Erosive flux due to upward diffusion

The upward diffusion of sediment through the bottom of the kmx layer is given by the expression:

$$E^{(\ell)} = \varepsilon_s^{(\ell)} \frac{\partial c^{(\ell)}}{\partial z}, \tag{8.38}$$

where $\varepsilon_s^{(\ell)}$ and $\frac{\partial c^{(\ell)}}{\partial z}$ are evaluated at the bottom of the *kmx* layer.

We approximate this expression by:

$$E^{(\ell)} \approx \alpha_2^{(\ell)} \varepsilon_s^{(\ell)} \left(\frac{c_a^{(\ell)} - c_{kmx}^{(\ell)}}{\Delta z} \right), \tag{8.39}$$

where:

$\alpha_2^{(\ell)}$	correction factor for sediment concentration
$\varepsilon_s^{(\ell)}$	sediment diffusion coefficient evaluated at the bottom of the kmx cell of sediment fraction(ℓ)
$c_a^{(\ell)}$	reference concentration of sediment fraction(ℓ)
$c_{kmx}^{(\ell)}$	average concentration of the kmx cell of sediment fraction(ℓ)
Δz	difference in elevation between the centre of the kmx cell and Van Rijn's reference height: $\Delta z = z_{kmx} - a$

The erosion flux is split in a source and sink term:

$$E^{(\ell)} \approx \frac{\alpha_2^{(\ell)} \varepsilon_s^{(\ell)} c_a^{(\ell)}}{\Delta z} - \frac{\alpha_2^{(\ell)} \varepsilon_s^{(\ell)} c_{kmx}^{(\ell)}}{\Delta z}. \tag{8.40}$$

The first of these terms can be evaluated explicitly and is implemented as a sediment source term. The second can only be evaluated implicitly and is implemented as a (positive) sink term. Thus:

$$Source_{erosion}^{(\ell)} = \frac{\alpha_2^{(\ell)} \varepsilon_s^{(\ell)} c_a^{(\ell)}}{\Delta z} \tag{8.41}$$

$$Sink_{erosion}^{(\ell)} = \frac{\alpha_2^{(\ell)} \varepsilon_s^{(\ell)} c_{kmx}^{(\ell)}}{\Delta z} \tag{8.42}$$

Deposition flux due to sediment settling

The settling of sediment through the bottom of the kmx cell is given by the expression:

$$D^{(\ell)} = w_s^{(\ell)} c_{kmx(bot)}^{(\ell)}, \tag{8.43}$$

where $w_s^{(\ell)}$ and $c_{kmx(bot)}^{(\ell)}$ are evaluated at the bottom of the kmx layer.

We set:

$$c_{kmx(bot)}^{(\ell)} = \alpha_1^{(\ell)} c_{kmx}^{(\ell)}. \tag{8.44}$$

The deposition flux is approximated by:

$$D^{(\ell)} \approx \alpha_1^{(\ell)} c_{kmx}^{(\ell)} w_s^{(\ell)}. \tag{8.45}$$

This results in a simple deposition sink term:

$$Sink_{deposition}^{(\ell)} = \alpha_1^{(\ell)} c_{kmx}^{(\ell)} w_s^{(\ell)}. \tag{8.46}$$

The total source and sink terms is given by:

$$Source^{(\ell)} = \alpha_2^{(\ell)} c_a^{(\ell)} \left(\frac{\varepsilon_s^{(\ell)}}{\Delta z} \right), \tag{8.47}$$

$$Sink^{(\ell)} = \left[\alpha_2^{(\ell)} \left(\frac{\varepsilon_s^{(\ell)}}{\Delta z} \right) + \alpha_1^{(\ell)} w_s^{(\ell)} \right] c_{kmx}^{(\ell)}. \tag{8.48}$$

These source and sink terms are both guaranteed to be positive. The total net source and sink term in the layer kmx of Equation 8.1 becomes

$$S^{(\ell)} = \alpha_2^{(\ell)} c_a^{(\ell)} \left(\frac{\varepsilon_s^{(\ell)}}{\Delta z} \right) - \left[\alpha_2^{(\ell)} \left(\frac{\varepsilon_s^{(\ell)}}{\Delta z} \right) + \alpha_1^{(\ell)} w_s^{(\ell)} \right] c_{kmx}^{(\ell)}. \tag{8.49}$$

and S(ℓ) is equal to 0 in all other layers. Advection, particle settling, and diffusion are all set to zero at the bed to prevent double counting entrainment and deposition.

A.2.5 Non-cohesive sediment erosion and deposition in 2D

In 2D the entrainment and deposition terms discussed in the previous section, change into a relaxation towards an equilibrium concentration:

$$S^{(\ell)} = \frac{c_{eq}^{(\ell)} - c^{(\ell)}}{T^{(\ell)}} \tag{8.50}$$

where

$c^{(\ell)}$	(depth-averaged) concentration of sediment fraction (ℓ) [kg m^{-3}]
$c_{eq}^{(\ell)}$	equilibrium (depth-averaged) concentration of sediment fraction (ℓ) based on the selected transport formula [kg m^{-3}]
$S^{(\ell)}$	total net source and sink term [kg m^{-3} s^{-3}]
$T^{(\ell)}$	relaxation time scale [s]

Unless noted otherwise, the relaxation time scale is based on the work of Galappatti (1983)

$$\begin{aligned} T^{(\ell)} = \tilde{x} \exp \big[&(1.547 - 20.12\tilde{u})\, \tilde{x}^3 + \left(326.832\tilde{u}^{2.2047} - 0.2\right) \tilde{x}^2 \\ &+ (0.1385 \log(\tilde{u}) - 6.4061)\, \tilde{x} + 0.5467\tilde{u} + 2.1963\big] \end{aligned} \tag{8.51}$$

where

$\tilde{u}$	dimensionless ratio of shear velocity u_* over the depth-averaged velocity magnitude U [-]
$\tilde{x}$	dimensionless ratio of settling velocity w_s over the shear velocity u_* [-]

A.3 Bedload sediment transport of non-cohesive sediment

Bedload (or, for the simpler transport formulae, total load) transport is calculated for all “sand” and “bedload” sediment fractions by broadly according to the following approach: first, the magnitude and direction of the bedload transport at the cell centres is computed using the transport formula selected, subsequently the transport rates at the cell interfaces are determined, corrected for bed-slope effect and upwind bed composition and sediment availability.

A.3.1 Basic formulation

For simulations including waves the magnitude and direction of the bedload transport on a horizontal bed are calculated using the transport formula selected assuming sufficient sediment and ignoring bed composition except for e.g. hiding and exposure effects on the critical shear stresses. The default sediment transport formula is Van Rijn (1993).

Some of the sediment transport formulae prescribe the bedload transport direction whereas others predict just the magnitude of the sediment transport. In the latter case the initial transport direction will be assumed to be equal to the direction of the characteristic (near-bed) flow direction. In the case of a depth-averaged simulation, the secondary flow/spiral flow intensity Is optionally computed by the flow module may be taken into account; the bedload transport direction φτ is given by the following formula:

$$\tan(\varphi_\tau) = \frac{v - \alpha_I \frac{u}{U} I_s}{u + \alpha_I \frac{v}{U} I_s} \tag{8.52}$$

in which

$$\alpha_I = \frac{2}{\kappa^2} E_s \left(1 - \frac{\sqrt{g}}{\kappa C}\right) \tag{8.53}$$

where:

g	gravitational acceleration
κ	Von Kármán constant
C	Chézy roughness
U	the depth-averaged velocity
E_s	coefficient to be specified by you as `Espir` keyword in the morphology input file

The default value of Es is 0, which implies that the spiral flow effect on the bedload transport direction is not included. The spiral flow effect is of crucial importance in a depth-averaged simulation to get pointbar formation in river bends. This effect is only included for transport formulae that return the bedload transport rate but not its direction, i.e. Engelund & Hansen, Meyer-Peter & Muller, General formula, Van Rijn (1984), Ashida & Michiue and optionally the user-defined formula.

A.4 Transport formulations for non-cohesive sediment

A number of standard sediment transport formulations for non-cohesive sediment are available by default. The van Rijn (2007) was selected for this study.

A.4.1 Van Rijn (2007)

Van Rijn (2007a,b) describe the TRANSPORT2004 sediment transport model for clay, silt, and sand. At this moment, it can only be used for sediment fractions labelled as 'sand' although doing so does not impose a restriction on the grain size. The conceptual model distinguishes between sediment transport below the reference height a, which is treated as bedload transport, and that above the reference height, which is treated as suspended-load. The exchange of sediment between the bed and the water column happens via a boundary condition imposed at the reference height.

A.4.1.1 Reference concentration

The volumetric reference concentration is calculated as:

$$c_a = \max(c_{a,\max}, 0.015 f_{\text{silt}} \frac{D_{50}}{a} \frac{T_a^{1.5}}{D_*^{0.3}}) \tag{8.76}$$

where:

a reference height [m] given by

$$a = \frac{k_{s,c}}{30} + \max(0.01, \frac{1}{2}k_{s,c,r}, \frac{1}{2}k_{s,w,r}) \tag{8.77}$$

where $k_{s,c,w}$ and $k_{s,c,r}$ are both set equal to the ripple roughness height, and $k_{s,c}$ is the Nikuradse bed roughness height.

c_a volumetric concentration at reference height a [m^3 rock/m^3 fluid]

$c_{a,\max}$ maximum volumetric concentration at reference height a, specified as `CaMax` in the mor-file [m^3 rock/m^3 fluid]

f_{silt} dimensionless multiplication factor for silt fractions $\max(1, D_{\text{sand}}/D_{50})$ [-]

This concentration is subsequently multiplied by the specific density ρs of the considered sediment fraction to arrive at the mass concentration at the reference height. In order to evaluate this expression the following quantities must be calculated:

D_* non-dimensional particle diameter [-]

$$D_* = D_{50}\left[\frac{(s-1)g}{\nu^2}\right]^{1/3} \tag{8.78}$$

T_a non-dimensional bed-shear stress [-]

$$T_a = \frac{\tau'_{b,cw} - f_s\tau'_{cr}}{f_s\tau'_{cr}} \tag{8.79}$$

$\tau'_{b,cw}$ bed shear stress due to current in the presence of waves [N/m^2]

$$\tau'_{b,cw} = \alpha_{cw}\mu_c\tau_{b,c} + \mu_w\tau_{b,w} \tag{8.80}$$

α_{cw} wave-current interaction factor [-]

$$\alpha_{cw} = \max(0, \min(T_1 T_2, 1)) \tag{8.81}$$

$$T_1 = \left(\frac{{}^{10}\log(30\delta_m / r_a)}{{}^{10}\log(30\delta_m / r_c)} \right)^2 \tag{8.82}$$

$$T_2 = \left(\frac{{}^{10}\log(30h / r_c) - 1}{{}^{10}\log(30h / r_a) - 1} \right)^2 \tag{8.83}$$

μ_c efficiency factor current [-]

$$\mu_c = \frac{f'_c}{f_c} \tag{8.84}$$

f'_c gain related friction factor [-]

$$f'_c = 0.24 \left[{}^{10}\log\left(\frac{12h}{D_{90}} \right) \right]^{-2} \tag{8.85}$$

f_c total current-related friction factor [-]

$$f_c = 0.24 \left[{}^{10}\log\left(\frac{12h}{k_s} \right) \right]^{-2} \tag{8.86}$$

$\tau_{b,c}$ bed shear stress due to currents [N/m^2]

$$\tau_{b,c} = \frac{1}{8} \rho_w f_c u_{2D}^2 \tag{8.87}$$

μ_w wave-related efficiency factor [-]

$$\mu_w = \max\left(0.14, \min\left(0.7/D_*, 0.35\right)\right) \tag{8.88}$$

$\tau_{b,w}$ bed shear stress due to waves [N/m^2]

$$\tau_{b,w} = \frac{1}{4}\rho_w f_w \left(\widehat{U}_\delta\right)^2 \tag{8.89}$$

f_w total wave-related friction factor [-] (≡ Equations 8.171, 8.210 and 8.251):

$$f_w = \exp\left[-6 + 5.2\left(\frac{A_\delta}{k_{s,w}}\right)^{-0.19}\right] \tag{8.90}$$

$\widehat{U}_\delta$ representative peak orbital velocity for reference concentration [m/s]

$$\widehat{U}_\delta = \left(\frac{1}{2}u_{\mathrm{on}}^3 + \frac{1}{2}u_{\mathrm{off}}^3\right)^{1/3} \tag{8.91}$$

A_δ peak orbital excursion at edge of wave boundary layer [m] according linear wave theory

$$A_\delta = \frac{H_s}{2\sinh(\max(10^{-12}, \frac{2\pi h}{\lambda}))} \tag{8.92}$$

A.4.1.2 Bedload transport rate due to currents

The total bedload transport vector ⃗Sb,t is split into a current related part ⃗Sb,c and a waves related part ⃗Sb,w. Here we focus on computing the former. The transport vector due to currents is computed as the average of the instantaneous total transport rates Sb(t) over a wave period subdivided into NT sections weighted by the ratio of the flow velocity due to currents ⃗ua,c over the magnitude of the total instantaneous velocity due to both currents and waves Ua,t(t) both defined at the reference height *a*.

$$\vec{S}_{b,c} = \frac{1}{N_T}\sum_{t=1}^{N_T}\frac{\vec{u}_{a,c}}{U_{a,t}(t)}S_b(t) \tag{8.93}$$

with $S_b(t)$ the intrawave instantaneous bedload transport rate given by

$$S_b(t) = \frac{1}{2}D_{50}\rho_s\frac{f_{\mathrm{silt}}}{D_*^{0.3}}u_*'(t)T'(t) \tag{8.94}$$

where

u_*' the intrawave instantaneous shear velocity

$$u_*'(t) = \sqrt{\tau'(t)/\rho_w} \tag{8.95}$$

$T'(t)$ the intrawave instantaneous dimensionless excess shear parameter

$$T'(t) = \max(10^{-3}, \frac{\tau'(t) - r_2 f_s \tau_{cr}}{f_s \tau_{cr}}) \tag{8.96}$$

where

$$r_2 = 0.8 + 0.2(\frac{\tau'(t)}{f_s \tau_{cr}} - 0.8) \tag{8.97}$$

is clipped to values between 0.8 and 1.

$\tau'(t)$ the intrawave instantaneous bed shear stress

$$\tau'(t) = \frac{1}{2} \rho_w f'_{c,w} U_{a,t}(t)^2 \tag{8.98}$$

with

$$f'_{c,w} = a_{cw} \beta_{cw} f'_c + (1 - a_{cw}) f_w \tag{8.99}$$

where

$$a_{cw} = \frac{U_{2D}}{\max(10^{-6}, U_\delta + U_{2D})} \tag{8.100}$$

and

$$\beta_{cw} = \frac{1}{4} \left[\frac{-1 + \ln(30h/r_c)}{\ln(30a/r_c)} \right]^2 \tag{8.101}$$

with

U_δ near-bed peak orbital velocity [m/s] according linear wave theory

$$U_\delta = \frac{2\pi}{T_p A_\delta} \tag{8.102}$$

where A_δ is given by Equation (8.92)

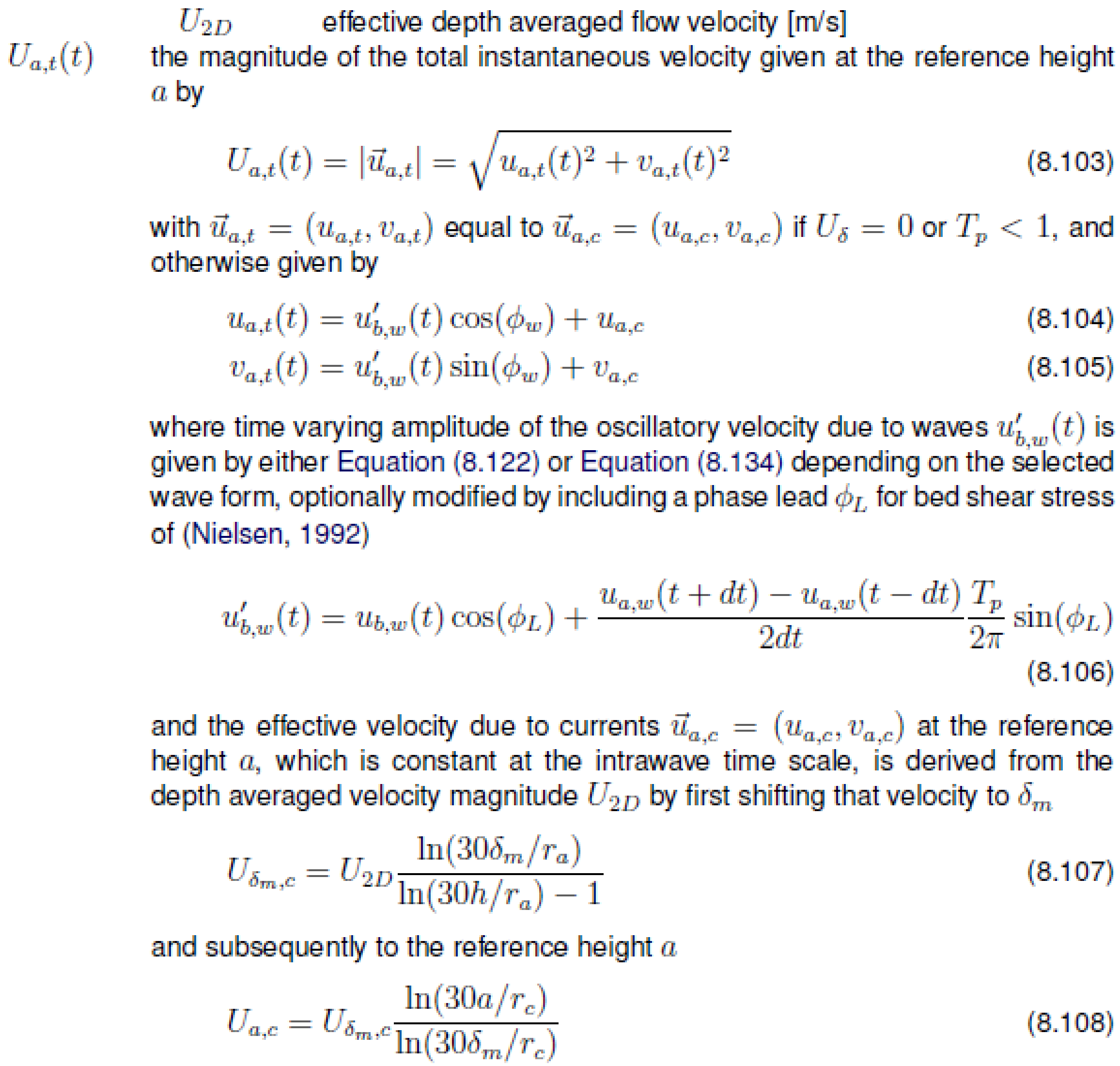

U_{2D} effective depth averaged flow velocity [m/s]

$U_{a,t}(t)$ the magnitude of the total instantaneous velocity given at the reference height a by

$$U_{a,t}(t) = |\vec{u}_{a,t}| = \sqrt{u_{a,t}(t)^2 + v_{a,t}(t)^2} \tag{8.103}$$

with $\vec{u}_{a,t} = (u_{a,t}, v_{a,t})$ equal to $\vec{u}_{a,c} = (u_{a,c}, v_{a,c})$ if $U_\delta = 0$ or $T_p < 1$, and otherwise given by

$$u_{a,t}(t) = u'_{b,w}(t)\cos(\phi_w) + u_{a,c} \tag{8.104}$$
$$v_{a,t}(t) = u'_{b,w}(t)\sin(\phi_w) + v_{a,c} \tag{8.105}$$

where time varying amplitude of the oscillatory velocity due to waves $u'_{b,w}(t)$ is given by either Equation (8.122) or Equation (8.134) depending on the selected wave form, optionally modified by including a phase lead ϕ_L for bed shear stress of (Nielsen, 1992)

$$u'_{b,w}(t) = u_{b,w}(t)\cos(\phi_L) + \frac{u_{a,w}(t+dt) - u_{a,w}(t-dt)}{2dt}\frac{T_p}{2\pi}\sin(\phi_L) \tag{8.106}$$

and the effective velocity due to currents $\vec{u}_{a,c} = (u_{a,c}, v_{a,c})$ at the reference height a, which is constant at the intrawave time scale, is derived from the depth averaged velocity magnitude U_{2D} by first shifting that velocity to δ_m

$$U_{\delta_m,c} = U_{2D}\frac{\ln(30\delta_m/r_a)}{\ln(30h/r_a) - 1} \tag{8.107}$$

and subsequently to the reference height a

$$U_{a,c} = U_{\delta_m,c}\frac{\ln(30a/r_c)}{\ln(30\delta_m/r_c)} \tag{8.108}$$

unless 30δm < ra in which case Ua,c = 0, and subsequently using that velocity magnitude in the direction of the simulated flow velocity that corresponds best with the reference height a (which corresponds to the depth averaged flow direction in a 2D model, but depends on the layer distribution in a 3D model). The default wave velocity asymmetry is based on Isobe and Horikawa (1982) (Wform = 1).

A.4.1.3 Bedload transport rate due to waves

The bedload transport vector due to waves $\vec{S}_{b,w}$ is obtained by subtracting the bedload vector due to currents $\vec{S}_{b,c}$ (computed by Equation (8.93)) from the total bedload transport vector $\vec{S}_{b,t}$, i.e.

$$\vec{S}_{b,w} = \vec{S}_{b,t} - \vec{S}_{b,c} \tag{8.109}$$

where the total bedload transport vector is computed as

$$\vec{S}_{b,t} = \frac{1}{N_T} \sum_{t=1}^{N_T} \frac{\vec{u}_{b,t}(t)}{U(t)} S_b(t) \tag{8.110}$$

See the previous section for a definition of a terms.

A.4.1.4 Suspended load transport rate due to waves

The suspended load transport vector due to the asymmetric oscillatory wave motion $\vec{S}_{s,w}$ is obtained by multiplying the mean concentration c_{sl} in the suspension layer by the net flow velocity due to wave asymmetry $\vec{u}_a$ for that layer

$$\vec{S}_{s,w} = c_{\mathrm{sl}} \vec{u}_a \tag{8.111}$$

where the velocity vector $\vec{u}_a = (u_a, v_a)$ is defined as

$$u_a = U_a \cos(\phi_w) \tag{8.112}$$

$$v_a = U_a \sin(\phi_w) \tag{8.113}$$

where the magnitude U_a of the net flow due to the velocity asymmetry is given by

$$U_a = 0.1 p_2 \frac{u_{\mathrm{on}}^4 - u_{\mathrm{off}}^4}{u_{\mathrm{on}}^3 + u_{\mathrm{off}}^3} \tag{8.114}$$

if the effective velocity

$$v_{\mathrm{eff}} = \sqrt{U_{2D}^2 + u_{\mathrm{on}}^2} - v_{cr} \tag{8.115}$$

is larger than $\varepsilon = 10^{-6}$; otherwise $\vec{S}_{s,w} = 0$. In these equations, u_{on} and u_{off} depend on the selected wave form (see Sections 8.5.1.5 or 8.5.1.6, and

p phase lag parameter [-] is either user specified (`Fpco`), or computed as

$$p = -\tanh\left(100(\frac{k_{s,r}}{w_s T_p} - 0.1)\right) \tag{8.116}$$

based on ripple roughness height $k_{s,r}$, settling velocity w_s and wave peak period T_p.

v_{cr} critical flow velocity [m/s] given by

$$v_{\mathrm{cr}} = 5.75\sqrt{sgD_{50}\theta_{\mathrm{cr}}}\ {}^{10}\log(4h/D_{90}) \tag{8.117}$$

Furthermore, the mean concentration c_{sl} over the suspension layer with an assumed thickness of $\delta = 3\delta_s$, insofar as it's above the reference height a, is numerically approximated by

$$c_{\mathrm{sl}} = \sum_{k=1}^{\mathrm{kmax}} \begin{cases} c_k(3\delta_s - z_k - \frac{1}{2}d_k) & \text{if layer } k \text{ contains } 3\delta_s \\ c_k d_k & \text{if layer } k \text{ is fully between } a \text{ and } 3\delta_s \\ c_k^*(z_k + \frac{1}{2}d_k - a) & \text{if layer } k \text{ contains } a \\ 0 & \text{for layers above } 3\delta_s \text{ or below } a \end{cases} \tag{8.118}$$

where z_k is height of the centre of layer k above the bed (the layers are numbered from the bed upward). Because of the typically large concentration gradient at the bottom of the concentration profile, the concentration c_k^* of the bottommost partial layer is computed based on the assumption of a Rouse profile

$$c_k^* = c_k\left(\frac{z_k(h-z)}{z(h-z_k)}\right)^Z \tag{8.119}$$

where z is the characteristic average height above the bed for that layer

$$z = \frac{z_k + \frac{1}{2}d_k + a}{2} \tag{8.120}$$

and where Z is the suspension number derived from the computed concentrations of layers k and $k+1$ as

$$Z = \frac{\ln(c_{k+1}/c_k)}{\ln(z_k/(h - z_{k+1}))} \tag{8.121}$$

A.4.1.5 Wave asymmetry Isobe and Horikawa (1982)

Following Isobe and Horikawa (1982), the time variation of the velocity due to waves is modelled as a sine wave of which the first (onshore) and second (offshore) half are compressed/stretched relative to each other.

$$u_{b,w}(t) = \begin{cases} u_{\text{on}} \sin\left(\frac{\pi}{T_{\text{for}}} t\right) & \text{for } 0 \leq t < T_{\text{for}} \\ u_{\text{off}} \sin\left(\frac{\pi}{T_{\text{back}}} (t - T_{\text{for}})\right) & \text{for } T_{\text{for}} \leq T < T_p \end{cases} \tag{8.122}$$

with the duration for onshore (T_{for}) and offshore (T_{back}) directed velocities are calculated as

$$T_{\text{for}} = \frac{u_{\text{off}}}{u_{\text{on}} + u_{\text{off}}} T_p \tag{8.123}$$

$$T_{\text{back}} = T_p - T_{\text{for}} \tag{8.124}$$

The associated maximum on- and offshore velocities are computed using

$$u_{\text{on}} = U_{\text{max}} \left[\frac{1}{2} + \left(r_{\text{max}} - \frac{1}{2}\right) \tanh\left(\frac{r_a - \frac{1}{2}}{r_{\text{max}} - \frac{1}{2}}\right)\right] \tag{8.125}$$

$$u_{\text{off}} = U_{\text{max}} - u_{\text{on}} \tag{8.126}$$

Both values are clipped to be at least $1 \cdot 10^{-5}$ [m/s]. Here the maximum velocity amplitude is computed as

$$U_{\text{max}} = 2rU_\delta \tag{8.127}$$

and the skewness r_a is given by

$$r_a = -5.25 - 6.1 \tanh(a_{11} u_1 - 1.76) \tag{8.128}$$

where r_a is clipped to values larger than 0.5, and the maximum skewness r_{max} is given by

$$r_{\text{max}} = -2.5 \frac{h}{\lambda} + 0.85 \tag{8.129}$$

following Grasmeijer (2002) where values are clipped within the range 0.62 to 0.75. In the various formulae the following symbols are used

$$r = -0.4 \frac{h_s}{h} + 1 \tag{8.130}$$

$$u_1 = \frac{u_{\text{max}}}{\sqrt{gh}} \tag{8.131}$$

$$a_{11} = -0.0049 t_1^2 - 0.069 t_1 + 0.2911 \tag{8.132}$$

$$t_1 = T_p \sqrt{\frac{g}{h}} \tag{8.133}$$

Appendix B: Inner Harbour Assessment

B.1 Model Verification

Published Data – Inner Harbour

In the study conducted by Green et al. (2000), the authors analyse the time series of suspended-silt concentration measured by an optical backscatter sensor and suspended-sand concentration measured by an acoustic backscatter sensor in a deep channel (14 m MSL) of Manukau Harbour.

Sand (100-200 µm) concentrations estimated from the acoustic backscatter (ABS) measurements, showed that sand concentration peaked at 100-200 mg/l at a distance of 1 cm from the seabed (Figure B-1).

We extracted depth-averaged sediment concentration, from a number of modelled scenarios, at the same location as the ABS deployment site (37 03.96 S, 174 42.32 E (1751608.785 5896445.864). Using the same technique as in the fieldwork measurement comparison (i.e., applying the Rouse profile – Section 3.2.4.1), we distributed the depth-averaged concentration over the water column using the Rouse model and calculated concentration at the same height as in the work of Green et al (2000), i.e., at 1 cm from the seabed.

Figure B-2 shows modelled peaks in concentration of 40 and 80 mg/l for a scenario over typical tides using particle size of 150 µm, which was a similar particle size used in the study of Green et al. 2000 (i.e., 100-200 µm).

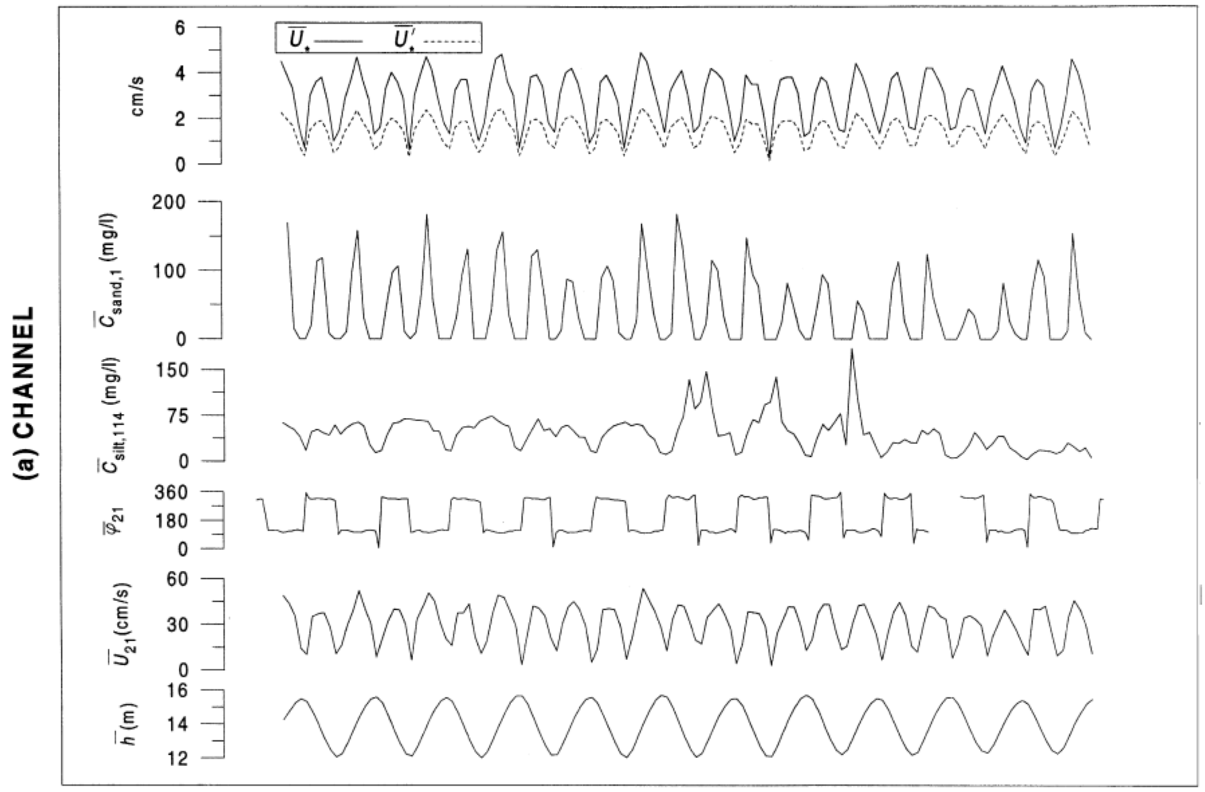

Figure B-1 Timeseries of burst-averaged data. Concentration of sand is presented in the second graph from the top (C_{sand},1). Site located at 37 03.96 S, 174 42.32 E (1751608.785 5896445.864) in Poutawa Channel. Source: Green et al. (2000).

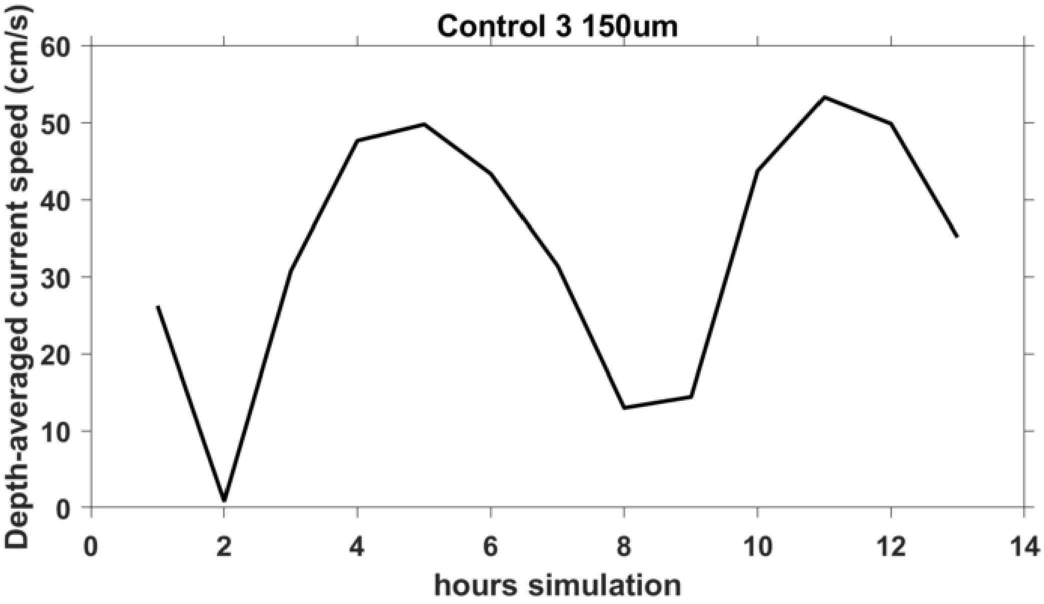

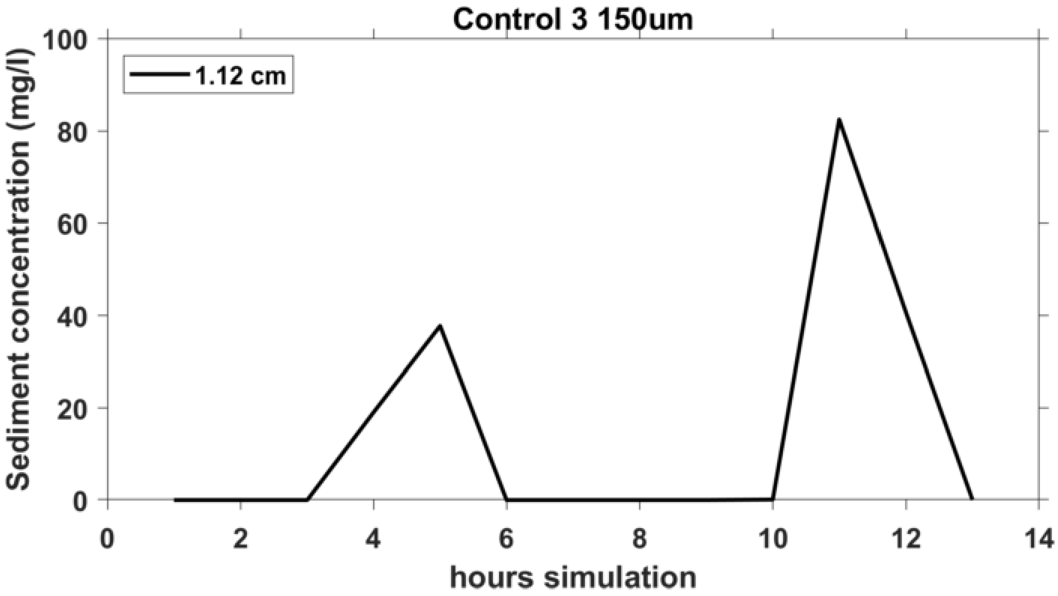

Figure B-2 Top: timeseries of depth-averaged current speed (cm/s). Bottom: timeseries of sediment concentration (mg/l) at approximately 1 cm from seabed estimated from the depth-averaged model results using the Rouse profile. Results are over a typical tide and forcing wave conditions H_s = 5 m, T_p = 15 s and Dir = 230 deg (Control 3). This run used a particle size of 150 µm.

B.2 Sediment Infill Processing Areas

Following the methodology presented in Section 4.2, infill rates were calculated for a polygon (Polygon 10) located in the upper inner harbour, near the representative port location (Figure B-3).

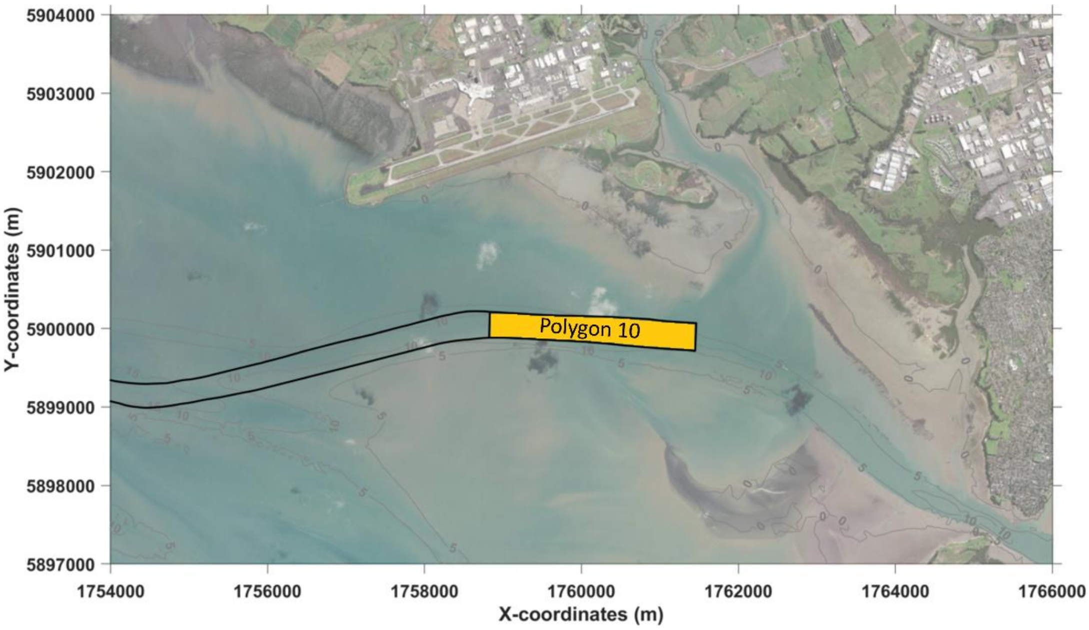

Figure B-3 Polygons used to calculate infill rates within the harbour.

B.3 Sedimentation

Deposition volumes in the inner harbour polygon were very low compared to the volumes within the bar polygons (3+4+5+6), averaging around 58 m^3 with a maximum deposition of approximately 400 m^3 (Table B-1).

Wind vs no wind scenarios

In scenarios including wind (control 3a, 4a, and 5a), regarding the inner harbour, wind generated currents increased the sediment transport rate over shallow area and led to an increase in sediment deposition, particularly during spring tide (4a), although the overall net result remained predominantly erosive (Figure B-4).

SW vs NW wave scenarios

In our control runs, we examined the impact of wave direction from the northwest (NW) on sediment erosion and deposition patterns. Volumes calculated for the inner harbour polygon remained consistent when compared to scenarios using SW waves.

Runs using 150 µm and 500 µm sediment fractions

The results showed, as anticipated, increased sediment transport (Figure B-6) and higher predicted infill volumes (Table B-2) for fine sand (150 µm) compared to medium (250 µm) and coarse (500 µm) sand, with the coarser fraction resulting in less infill in comparison to the other fractions.

The effect of the wind on the infill rates in the inner harbour was tested for the finer fraction (150 um). We ran two scenarios with wind speeds of 10 m/s and 20 m/s, and compared to scenarios without wind, all considering a typical tide.

In the 10 m/s wind scenario, deposition was approximately 1.3 times greater than in the no-wind scenario. For the 20 m/s wind scenario, deposition was 4.2 times greater than at 10 m/s and 5.7 times greater than the no-wind scenario (Table B-3).

Figure B-7 presents the maps of erosion and deposition for these scenarios. Within polygon 10, net infill is positive for the no-wind and medium strength wind scenarios but erosive for the strong wind (20 m/s) scenario. Deposition mainly occurs in a small region southeast of the polygon. By the end of the simulation, the maps show erosion in most of the channel near the port, with some deposition along the channel batter slope.

Table B-1: Infill volumes for the inner harbour (polygon 10) after 12h (m^3). Infill above design depth are presented only for scenarios which included the concept navigation channel.

Scenario	Infill inner harbour–- deposition after 12h (m^3)	Infill inner harbour–- NET after 12h (m^3)	Infill inner harbour–- deposition above design depth (m^3)
Control 1	24	-1	n/a
Control 1 (3 sed)	37	-9	n/a
Control 2	21	12	18
Control 2 (3 sed)	50	38	43
Control 3	19	-1	n/a
Control 3 (3 sed)	32	-6	n/a
3a	145	-84	n/a
Control 4	163	-39	n/a
4a	413	-354	n/a
Control 5	0	0	n/a
5a	38	-46	n/a
Control 6	19	-1	n/a
Control 7	16	9	14
Control 7 (3 sed)	38	28	32
Control 8	219	123	179
Control 9	0	0	0
Control 10	16	9	14
Control 11	13	8	12
Control 12	14	8	12
Control 13	33	-5	n/a
Control 14	20	-1	n/a
Control 15	16	10	14
Control 16	22	-1	n/a
Control 17	23	-1	n/a

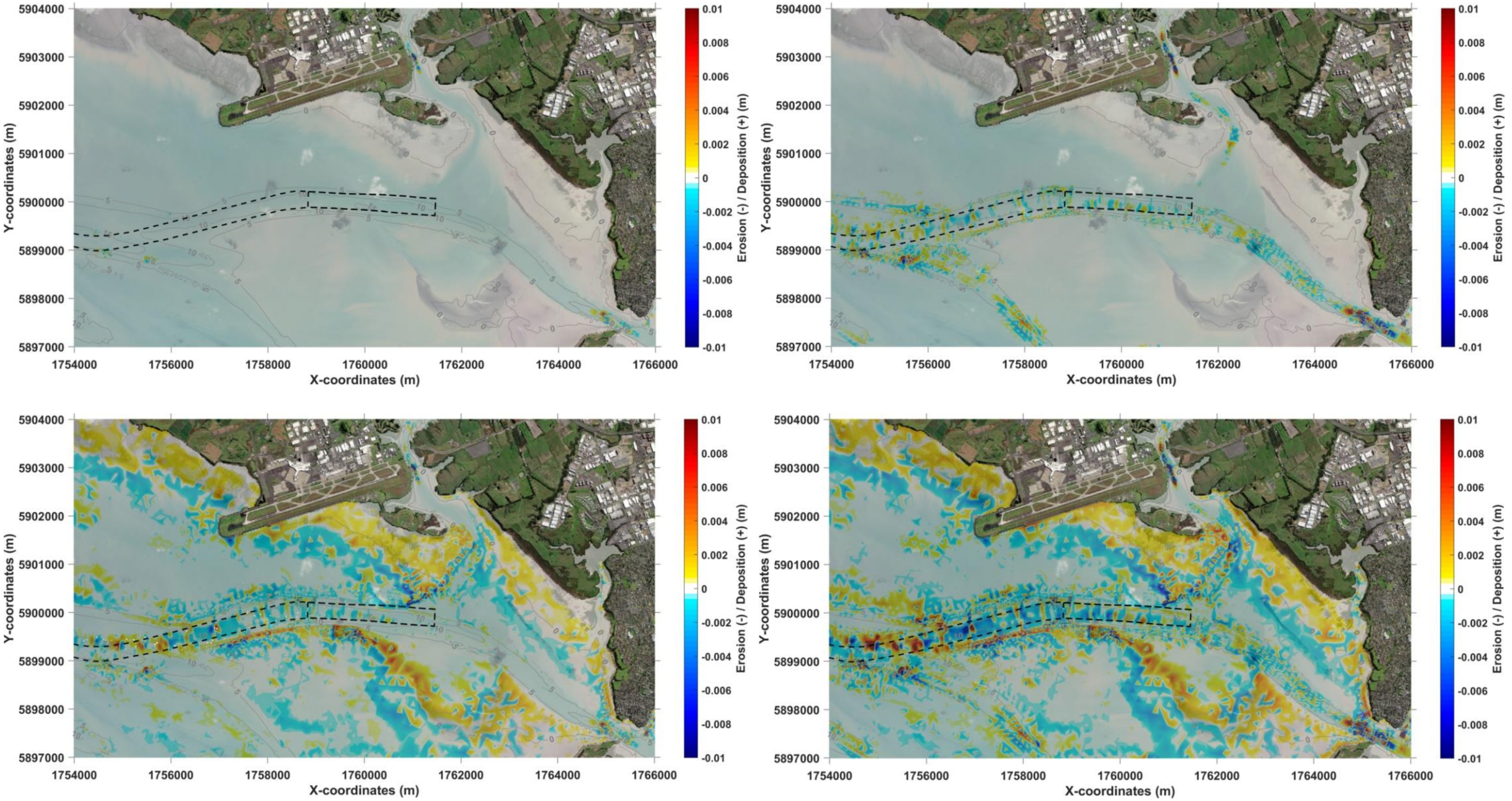

Figure B-4 *Examples of maps of erosion (negative, blue) and deposition (positive, red) results for the inner harbour for scenarios without wind (left) and with wind (right). Top left: Control 3, Top right: Control 3a, Bottom left: Control 4, and Bottom right: Control 4a.*

Table B-2: Infill volumes for the inner harbour (polygon 10) after 12h (m³) for runs using a different particle size each (150 µm, 250 µm, and 500 µm). Infill above design depth is presented only for scenarios which included the concept navigation channel.

	Infill inner harbour-- deposition after 12h (m^3)	Infill inner harbour-- NET after 12h (m^3)	Infill inner harbour-- deposition above design depth (m^3)
Control_03_150	38	-10	n/a
Control_03_250	19	-1	n/a
Control_03_500	18	-1	n/a
Control_07_150	46	38	39
Control_07_250	16	9	14
Control_07_500	14	8	12

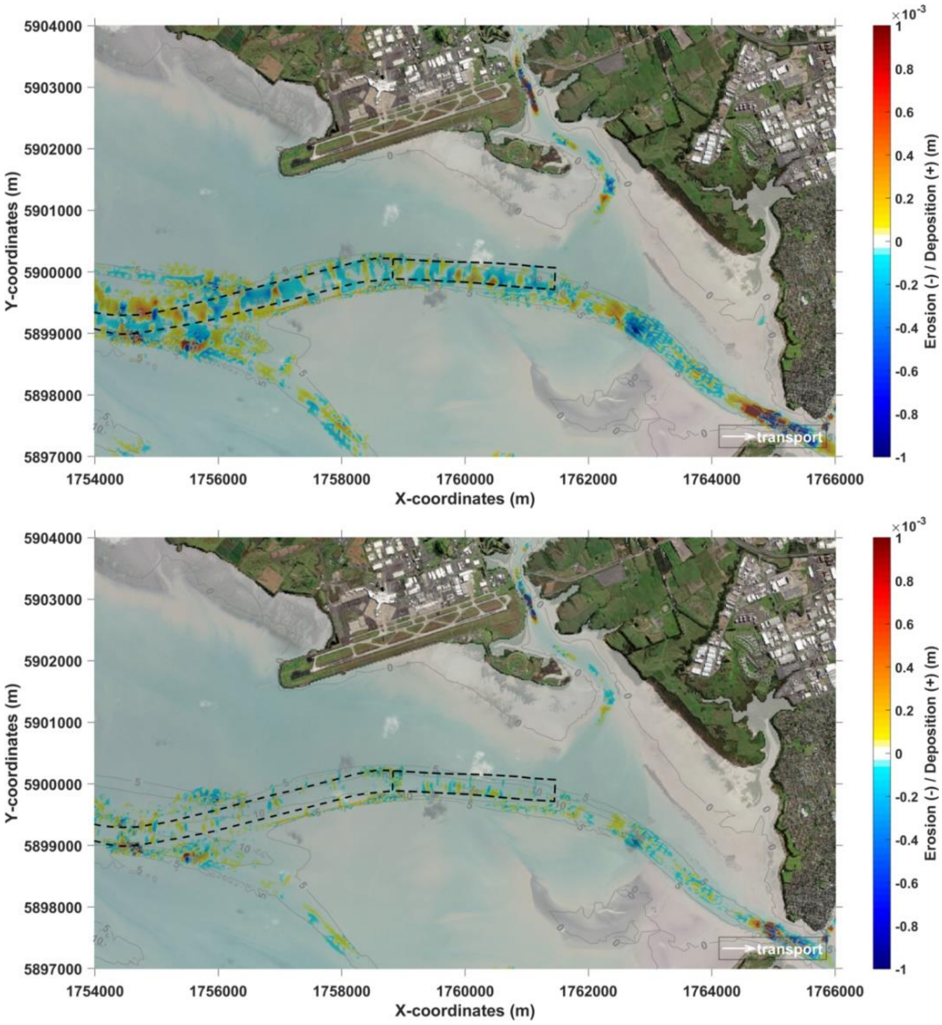

Figure B-6 Maps of erosion (negative, blue) and deposition (positive, red) results (Control 3) for runs using 150 µm fraction (top) and 500 µm (bottom). Note the difference in scale for the erosion/deposition in the inner harbour maps.

Table B-3 Inner harbour infill rate for finer 150 µm fraction including, wind speed 10 m/s and 20 m/s for Control 7. Results with no wind also included for comparison.

	Control_07 150 µm no wind	**Control_07 150 µm wind 10 m/s**	**Control_07 150 µm wind 20 m/s**
Deposition (m^3)	46	62	261
Erosion (m^3)	-8	-16	-315
NET (m^3)	37	46	-54
Above design depth (m^3)	39	53	240

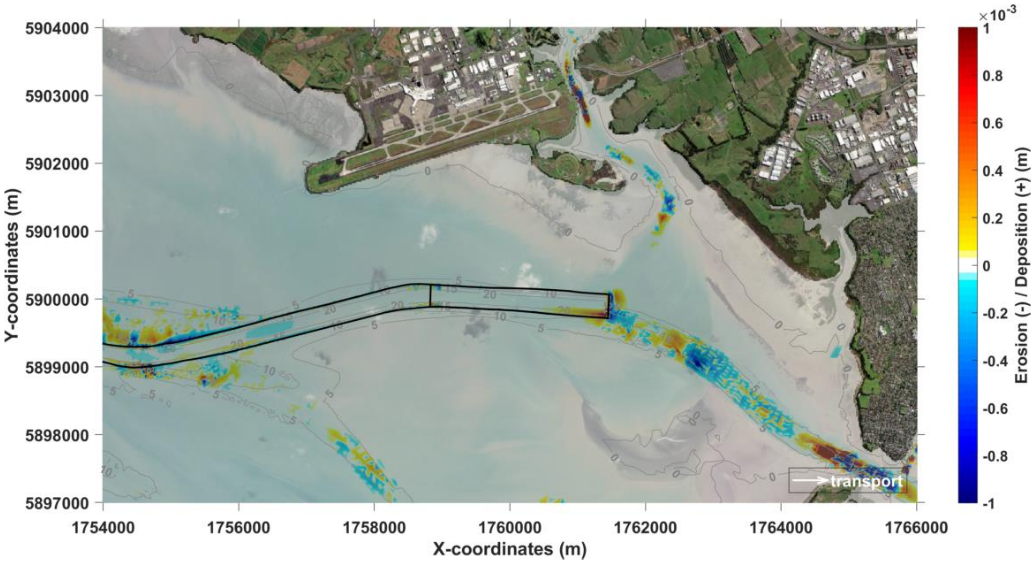

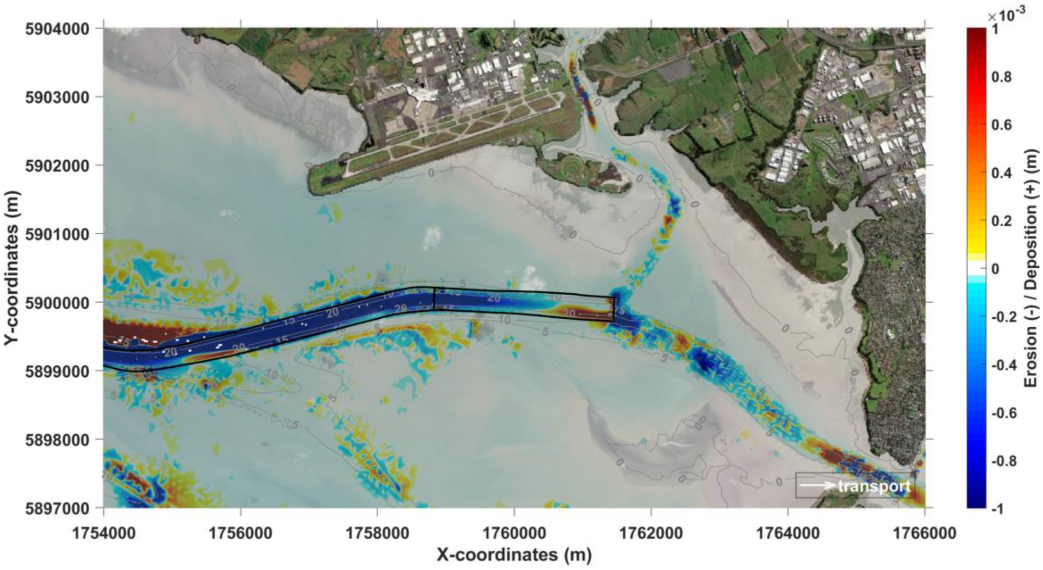

Figure B-7 Maps of erosion (negative, blue) and deposition (positive, red) for Control 7 without wind (top), wind = 10 m/s (middle), and wind = 20 m/s (bottom).

B.4 Inner Harbour Port Area Annual Infill

The estimate of sediment infill that may occur near the proposed port area was undertaken based on the results from the Control scenarios presented in Section 4.2, and the predicted infill in Polygon 10 (see Figure B-3) for the fine sands sediment fraction (i.e. 150µm). Swell waves do not penetrate all the way to the inner harbour. Sediment transport there is expected to be a result of sediment resuspension due to wind wave actions (when winds are included in the simulations) and currents in the shallow intertidal areas. Tidal currents together with wind generated currents transport sediment which in turn settle in deeper area of the harbour such as the dredged navigation channel and port area. With the concept navigation channel mostly sitting within the natural deep channel of the harbour the sedimentation is limited to the areas close to shallow adjacent banks.

A summary of the sediment infill (Polygon 10) is presented below:

Tide only no wind:

- Infill is negligible during neap tide.
- Minimal infill during a typical tide approximately 100m^3/24hour.
- Infill is about 10 times larger during a spring tide than a typical tide.

Tide with medium strength wind (10m/s):

- Infill is minimal during neap tide.

- Infill during a typical tide approximately 125 m^3/24hour.
- With medium winds the infill is about 4 times larger during a spring tide than a typical tide (i.e. 500 m^3/24hour).

Tide with strong wind (20m/s):

- Infill is about 125 m^3/24hour during neap tide.
- Infill during a typical tide approximately 500 m^3/24hour.
- With wind infill is about 4 time larger during a spring tide than a typical tide (i.e. 2000 m^3/24hour).

Analysis of the wind speed probability of occurrence showed that the wind speed from Auckland Airport showed that winds are less than 5 m/s for 50% of the time and greater than 15 m/s for less than 1% of the time.

Based on the above, infill estimates were combined with wind probabilities to determine the overall annual infill estimate within Polygon 10 (Figure B-3), which covers 2.6 km of channel, is expected to be approximately 100,000 to 150,000 m^3/year.

Note that is considering fine sands only as we have not modelled silts and clays.

Sedimentation is also expected on the batter slopes of the dredged channel at about 60,000 m^3/year per km of channel. There is about 5 km of channel from the port area with dredged batter slopes. So, assuming another 5 km of channel from the port area (Polygon 10) this amounts to 300,000 m^3/year.

It is likely that small, localised infill will occur elsewhere along the inner harbour channel, particularly where the channel intersects other natural tributaries. Although this sedimentation is expected to be smoothed out by strong ebb currents.